Studies on Functional Magnetic Resonance Imaging with Higher Spatial and Temporal Resolutions

Shizue Nagahara

Graduate School of Engineering, Kyoto University

Acknowledgments

First of all, I would like to give hertful thanks to my supervisor Professor Tetsuo Kobayashi who offered continuing support and constant encouragement.

I also owe a very important debt to Professor Koji Koyamada and Professor Takashi Hikihara whose comments made enormous contribution to my work. It is a pleasure to thank Dr. Michiko Narasaki and Dr. Hidehiko Imai for providing the instruction of experiments and their insightful suggestions and comments. Advice, comments and generous encouragement given by Professor Susumu Mori, Dr. Shoko Yoshida, and all members in Johns Hopkins University has been a great help when I visited their group in USA. I acknowledge the constructive comments and generous help by Associate Professor Shoji Hamada, Dr. Takenori Oida, Dr. Yosuke Ito, Dr. Shiho Okuhata and Dr. Hiroaki Natsukawa. I also acknowledge the technical, moral supports, and cheerful atmosphere by all members of the Kobayashi group. I am particularly grateful for the assistance given by Ms. Utako Yamamoto, Mr. Wataru Nakayama and Mr. Masahito Ueno.

This work was financially supported by a Grant-in-Aid for Japan Society for the Promotion of Science (JSPS) Fellows (23-5348).

Finally I would like to offer special thanks to my family for their moral support and warm encouragement.

Abstract

Functional magnetic resonance imaging (fMRI) provides us where neural activities occur and helps us determining the region of the human brain which associates with the targeted brain function. In recent years, expectations for alternative methods of conventional fMRI, which observes hemodynamic responses related to neural activities, have been larger. This is because the conventional fMRI is considered to record neural activities indirectly and have poor spatial and temporal resolutions. Among the emerging fMRI methods, we evaluated the feasibility of two of those in this dissertation: one is based on diffusion weighted imaging (DWI) and the other uses spin-lock imaging sequence. In addition, we investigated appropriate imaging conditions for those approaches through numerical simulations and measurements with MRI.

First, we studied on the method to noninvasively measure human brain functions by DWI, which is one of the MRI techniques. This approach is based on the fact that neural and/or grial cells in the brain swell when neuronal activations occur resulting in changes in diffusion of water molecules. Thus, the spatial and temporal resolutions of this technique are expected to be superior to those of the conventional fMRI. In the diffusion where the motion of water molecules is restricted by obstacles, the signal intensity of DWI varies intricately with motion probing gradient (MPG) parameters. We carried out the Monte Carlo simulations of the movements of water molecules diffusing in restricted structures whose sizes were comparable to those of neurons to clarify how the size of the regions where water molecules move around neural cells affect the acquired DWI signal intensities and determine appropriate MPG parameters for brain mapping. As a result, the acquired DWI signal intensities changed because of changes in the size of the regions where water molecules moved; that is, cell swellings induced changes in DWI signal intensities. The simulation results also indicated that the signal intensities varied greatly depending on the size of the restricted structures and the MPG parameters. According to this simulation, we estimated the MPG parameters that maximize the difference in DWI signal intensities before and after cell swelling.

Subsequently, we extended our simulation model mentioned above to take into account influences of water diffusion of both intracellular and extracellular regions. To investigate how the DWI signal intensities change in DW-fMRI measurements, we also carried out

Monte Carlo simulations to evaluate the intensities before and after cell swelling. In the simulations, we modeled cortical cells as two compartments by considering differences between the intracellular and the extracellular regions. Simulation results suggested that DWI signal intensities increase after cell swelling because of an increase in the intracellular volume ratio. The simulation model with two compartments, which respectively represent the intracellular and the extracellular regions, shows that the differences in the DWI signal intensities depend on the ratio of the intracellular and the extracellular volumes. We also investigated the MPG parameters, b-value, and separation time dependences on the percent signal changes in DW-fMRI and obtained useful results for DW-fMRI measurements.

Finally, we investigated an fMRI method with spin-lock imaging sequence that focuses on neural magnetic fields and has strong potential to detect neural activities more directly than the conventional method. Because this fMRI does not depend on the hemodynamic phenomenon, improved temporal and spatial resolutions can be expected in fMRI measurements. Therefore, to understand the mechanism of this approach, we visualized magnetization behavior during the measurement with externally applied oscillating magnetic fields assuming targeted neural magnetic fields. Furthermore, to detect minute magnetic fields of the order of sub-nT, we carried out phantom studies on the practical use of this method as an fMRI approach. A single-loop coil generating oscillating magnetic fields was placed inside a saline-filled phantom. Time-dependent performance of magnetization during the spin-lock imaging sequence was thus visually demonstrated for improving understanding of the mechanism of the fMRI method with the spin-lock imaging sequence. Moreover, we were able to detect magnetic fields of approximately 200 pT by choosing a spin-lock pulse of long duration and increasing the number of MR image acquisitions. Our results provide useful information for understanding the mechanism of the direct detection of oscillating neural magnetic fields using a spin-lock imaging sequence with MRI. In addition, we propose the feasibility of detecting oscillating magnetic fields of 200 pT while considering realistic fMRI use.

We believe that the findings described above are helpful for improvement of two novel fMRI approaches and their practical use in the future.

Contents

List of Figures

List of Tables

Chapter 1

Introduction

I believe that "what consciousness is" is one of the biggest mysteries of human beings. It has been discussed as the subject not only in the region of medicine but also in the region of philosophy over many years; however, we have not reached the answer. Although the most of the mystery remains unrevealed, it is considered that the consciousness is controlled by the brain. Thus, to reveal "what consciousness is" it is necessary to clarify the brain. With great advance of science, we are obtaining knowledges about the brain: what consists the brain and how the brain works. In particular, after the emergence of noninvasive technical methods for measurement of the brain functions, mechanisms of various brain functions, e.g. visual or auditory sense, have been discovered. In contrast, mechanisms of higher brain functions, e.g. recognition or memory, are still matter of debate; and therefore, further development of technical methods for measurement of the brain functions is expected.

There are several methods to measure the brain functions commonly used: Electroencephalogram (EEG) and Magnetoencephalogram (MEG), which are based on the measurement of electromagnetic fields, and, functional magnetic resonance imaging (fMRI) and near infrared spectroscopy (NIRS), which are based on the measurement of blood flow and metabolism. Among those approaches, fMRI is the most generally used approach because of its relatively high spatial resolution and ease of measurement. Hence, more and more researchers have employed fMRI as a tool to investigate the brain functions including the higher brain functions. In addition to elucidating the brain functions themselves, it is anticipated to help diagnosing psychiatric disorders, e.g. Alzheimer's disease [1, 2], dementia [3] or schizophrenia [4], and even treating them [5] in recent years. This is because psychiatric disorders are currently considered to be caused by abnormalities in the brain and they provide impairments in the brain functions. Therefore, the importance of improving the conventional methods for the measurement of brain functions or discovering the new technical approaches is increasing.

The technique of fMRI was established in the 1990s by researchers including Seiji

Ogawa [6, 7, 8]. The most widely used fMRI method is based on blood oxygenation level dependent (BOLD) effect, which causes MR signal changes due to the hemodynamic and metabolic phenomenon occurring after neural responses. Since we collect fMRI data using MRI equipment, we can make the use of its advantage of high spatial resolutions. We obtain information of the brain functions and MR images of anatomical brain structures simultaneously in fMRI measurement. Therefore, brain functions are spatially segregated in fMRI data and we can determine the specific region of the brain which the functions are localized.

However, the spatial resolution of fMRI is not sufficient because the mechanism of the BOLD-fMRI depends on not the neural activity itself but contributions from veins draining the regions of activation [9]. Hence, the BOLD-fMRI indirectly observes brain activation and cannot observe brain activation through neural activities directly as EEG or MEG. Moreover, there is also limitation for temporal resolution. MR signal changes originating from BOLD effect, what we call BOLD signals, usually reaches the peak a few seconds after the brain activation occurs; we explain details of the mechanism in the following chapter. In contrast, neural activities provide changes in electromagnetic fields a few hundreds milliseconds after the brain activation. Additionally, the undershoot of the BOLD signals continues for at least 15–20 seconds [10]; and therefore, the overlap of BOLD signals prevent us from investigating the individual events of brain activation. For these reasons, researchers have been attempting various kinds of fMRI approaches to overcome these disadvantages.

Instead of the fMRI approach based on BOLD effect, fMRI approaches based on other mechanisms have been proposed, in particular, based on contributions from extra-vascular regions of the brain—neural cells and/or glial cells—. An fMRI approach using diffusion weighted imaging (DWI) was proposed by D. Le Bihan et al. [11]. DWI can be carried out with the MRI technique, and it can measure and visualize the micromovement of water molecules, which is refereed to as diffusion [12]. It has been used for clinical use such as detecting acute brain ischemia or visualizing nerve bundles of white matters in the human brain [13].

D. Le Bihan et al. insisted that sources of MR signal changes are changes of diffusion of water molecules which are moving around neural cells in the fMRI approach using DWI [11, 14, 15, 16, 17]. Neural cells are considered to swell during the brain activation [18] and the swelling of neural cells affect diffusion of water molecules around the neural cells. Thus, we can measure brain functions based on the contributions of neural cells rather than hemodynamic and metabolic phenomenon. In spite of the proposal for the mechanism of the fMRI using DWI, however, the reason why MR signals change corresponding to brain activation in DWI has not been clarified. On the other hand, some researchers concluded that the fMRI using DWI observes the contribution of intra-vascular components [16, 19,

20, 21, 22]; and therefore, the use of DWI for fMRI measurements is still matter of debate.

Another approach which attempts to detect magnetic fields produced by neurons corresponding to neural activities is attracting attentions the most [23, 24, 25, 26, 27, 28, 29]. Mechanism of the approach is similar to the MEG and it present the most direct measurement of neural activities.

At first, it was suggested that we can observe neural activities as changes in magnitudes or phases of net magnetizations in acquired MR signals [30]. When the brain activates, magnetic fields are generated by neural currents, which run through neural cells. The magnetic fields are referred to neural magnetic fields and present subtle and transient alternations of static magnetic fields of MRI. Consequently, the magnitudes and phases of the net magnetization change in the regions where neural activities occur. However, there are problems of phase cancellation due to e.g. incoherent neuron orientation and no fMRI experiments have been reported in which neural magnetic fields were successfully detected.

Witzel et al. [31] and Halpern-Manners et al. [32] reported their studies of the fMRI detecting neural magnetic fields using spin-lock imaging sequence, which we mention the details in following chapter. In their studies, they insisted that the spin-lock imaging sequence has sensitivity to oscillating magnetic fields; and therefore, fMRI measurements can detect neural magnetic fields oscillating at a certain frequency. Both of them showed the successful detection of oscillating magnetic fields with MRI. However, the mechanism of the interaction between oscillating magnetic fields and spin-lock imaging sequence has not been clarified and it is still difficult to detect subtle neural magnetic fields of the order of sub-nT.

The objective of dissertation is to investigate fMRI approaches which are not based on hemodynamic and metabolic phenomena for higher spatial and temporal resolutions. In particular, we focused on two kinds of fMRI approaches; one is based on DWI and the other attempts direct detection of neural magnetic fields by using spin-lock imaging sequence. We investigated how these two approaches detect brain functions with MRI and appropriate imaging conditions for each approach.

As for the fMRI approach with DWI, we proposed a mechanism that changes in size of restricted regions where water molecules diffuse contribute to MR signal changes. We also investigated contributions of DWI parameters to MR signal changes and determined appropriate conditions for fMRI measurement. To evaluate the contribution of the size of restricted regions and DWI parameters, we achieved Monte Carlo simulations with a 2D circle simulation model in Chapter 3. We obtained MR signal intensities of DWI by calculating phases and positions of random walking water molecules. The simulation results demonstrated that the changes in MR signal intensities were caused by the changes in the size of restricted regions, which we assume cell swellings, and there exist appro-

priate values for DWI parameters. MRI measurements with a phantom supported the simulation results. Subsequently, we extended our simulation model to 3D cubes with two compartments indicating intracellular and extracellular regions in order to consider influences of water diffusion in those two different regions in Chapter 4. We employed the same simulation method used in Chapter 3 and investigated contributions of the size of restricted regions and DWI parameters. As a result, we found that change in volume ratio of intracellular and extracellular regions produced the increase in MR signal intensities after the cell swelling. We also obtained appropriate values to obtain DWI parameters for fMRI. The results with the extended simulations with the 3D model showed more reliable information for the mechanism of MR signal changes and employing appropriate values for DWI parameters to carry out fMRI measurements. These findings are helpful for further investigation of fMRI using DWI.

In Chapter 5, we clarified the interaction between spin-lock imaging sequence and oscillating magnetic fields which are target for direct detection based on the Bloch simulations. To demonstrate the interaction, we visualized a performance of a spin magnetization during the spin-lock imaging sequence and an application of oscillating magnetic fields. Bloch simulation was also used for investigating settings of spin-lock imaging sequences. Furthermore, oscillating magnetic fields of the order of sub-nT were detected by MRI measurements in phantom studies. The visualization of the spin magnetization performance helps understanding the mechanism of this fMRI approach, and the results obtained in the phantom studies demonstrate the feasibility of direct detection of neural magnetic fields using spin-lock imaging sequence.

Chapter 2

Background

We investigated the feasibility of new fMRI methods: DW-fMRI and NMFD-fMRI. In this chapter, we describe imaging techniques for MRI and fMRI as background of our study. Currently, fMRI based on BOLD contrast is generally used for brain mapping. However, its spatial and temporal resolutions are limited because it observes the hemodynamic responses associated with neural activations [11]. We therefore investigated alternative new fMRI methods using DWI (DW-fMRI) and spin-lock imaging (NMFD-fMRI). DWI is one of MRI techniques that visualizes the water self-diffusion in microscopic structures such as cellular tissues. Spin-lock imaging is also an MRI technique that has sensitivity for oscillating magnetic fields such as neural magnetic fields.

2.1 Magnetic resonance Imaging (MRI)

The technique of MRI is based on a chemical analytical technique called nuclear magnetic resonance (NMR). This section describes the principle of MRI with pulse sequence and signal processing [33].

2.1.1 Basic principles of MRI

For the measurement of MRI in humans, primary objects are hydrogen protons, so that we describe the NMR phenomenon of the hydrogen protons hereafter.

In MRI, a spinning charged hydrogen nucleus, which is a single positively charged proton, creates an electromagnetic field. Another property of the hydrogen nucleus that we know from quantum theory is that it has specific energy levels. This energy can be decided related to spin quantum number $\mathbf{I}$, and the hydrogen nucleus has a $\mathbf{I}$ of 1/2:

$$\mathbf{I}(\mathrm{H}) = \frac{1}{2}. \tag{2.1}$$

The number of energy states of the hydrogen nucleus is determined as

$$\text{The number of energy states} = 2\mathbf{I} + 1 = 2. \tag{2.2}$$

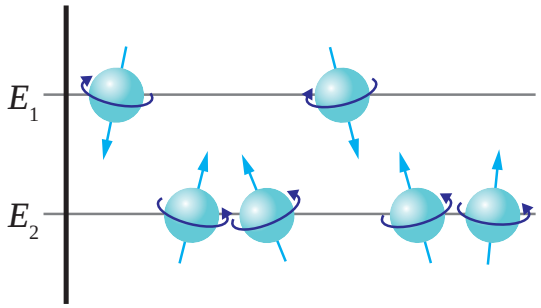

Figure 2.1: There are two energy states for hydrogen protons: E_1 and E_2. They are spinning about their axis and creating a magnetic field; the direction of the created magnetic field depends on the direction of rotation of the spinning protons.

Therefore, a hydrogen proton has two energy states: -1/2 and +1/2. As shown in Figure 2.1, the fact that they have two energy states creates two kinds of the hydrogen proton which are aligned in opposite directions.

When the charged spinning hydrogen protons are placed in an external static magnetic field $\mathbf{B}_0$, they align with the external field; some of those are in the direction of the magnetic field and the others are in the direction opposite to the magnetic field. The former ones have lower energy than the latter ones, and therefore more hydrogen protons point in this direction than in the opposite direction. As a result, the net magnetization $\mathbf{M}$ is produced in the direction parallel to the external static magnetic field. If there is no external magnetic field, the net magnetization $\mathbf{M}$ is zero.

Furthermore, the hydrogen protons placed in the magnetic field, they experience a torque and begins to precess at a certain angular frequency ω_0. This angular frequency is given by an equation called the Larmor equation [34]:

$$\omega_0 = \gamma B_0. \tag{2.3}$$

where γ is the gyromagnetic ratio and B_0 is the amplitude of the external static magnetic field [35]. The gyromagnetic ratio γ is constant and it is fixed for the nucleus of interest. For hydrogen protons $\gamma = 42.58$ MHz/T [36].

In MRI systems, if a three dimensional Cartesian coordinate is used, the orientation of the static magnetic field B_0 is conventionally taken to be along the z-axis, which is referred to "longitudinal" direction. The x-y plane, which is perpendicular to the z-axis, is called "transverse" plane. In order to receive signals in MRI we need electromagnetic wave of a very specific frequency. If it is transmitted into patients, it perturbs alignment of magnetization; signals are received from magnetization in the body when it returns to its original alignment. A radio frequency (RF) pulse is used for this process. The magnetization $\mathbf{M}_0$ which is initially aligned along z-axis (the axis of B_0) changes its orientation

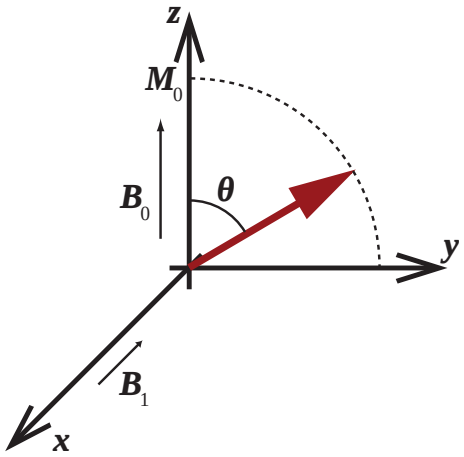

Figure 2.2: Magnetization vector is flipped toward x-y plane by application of RF pulse. As time passes, flip angle θ increases. Amplitude of θ is dependent on time τ and amplitude of the RF pulse B_1.

flipping into the x-y plane if the RF pulse whose frequency exactly matches the Larmor frequency is transmitted perpendicular to the z-axis. We call this phenomenon magnetic resonance. If the frequency of the RF pulse is different from the Larmor frequency, the magnetic resonance will not occur.

Here, we deal with two different magnetic fields: B_0, which is a very strong external static magnetic field (e.g., 1.5 T) and B_1, which is a very weak magnetic field (e.g., 50 mT) generated by an RF pulse and is oscillating at the Larmor frequency. During this magnetic resonance, each proton spins which was precessing out of phase and had no net transverse magnetization component lines up with B_1 field and then will be precessing in phase. Considering that the net magnetization are flipped into the transverse plane (x-y plane), this magnetic resonance produce a spiral motion of the magnetization down toward the transverse plane, and hence the transverse magnetization increase. The flip angle from the z-axis (Figure 2.2) can be determined by the amplitude of B_0 and the duration time of RF pulses [37]:

$$\theta = \gamma B_1 \tau \tag{2.4}$$

$$= \omega_1 \tau \tag{2.5}$$

where ω_1 is angle frequency of RF precession. Especially, θ of π /2 and π are often used, and those are called $\pi/2$ pulse and π pulse, respectively.

Moreover, as shown in Figure 2.3 the net magnetization is divided into M_z, which is longitudinal magnetization (z-axis) component, and M_{xy}, which is transverse (x-y plane) component, conventionally. As described above, if the magnetic resonance occurs, M_z decreases and M_{xy} increases.

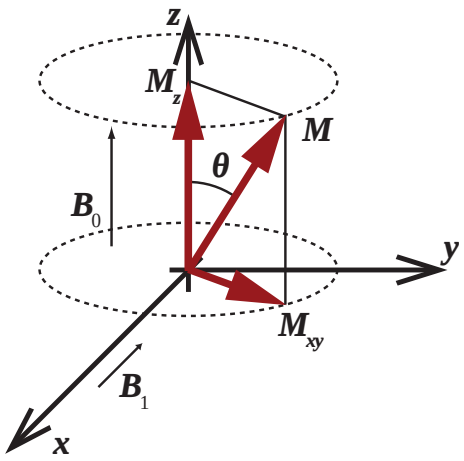

Figure 2.3: Net magnetization $\boldsymbol{M}$ can be divided into two components M_{xy} in x-y plane and M_z along z-axis in rotating coordinate systems.

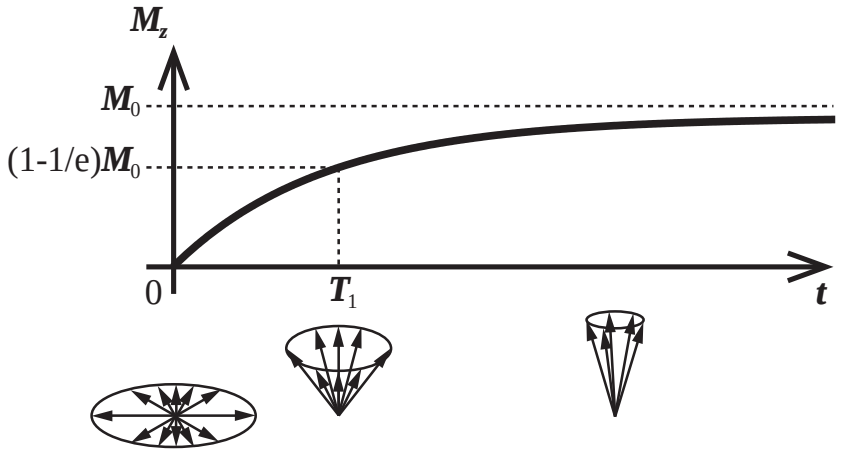

Figure 2.4: T_1 relaxation curve. Longitudinal component M_z recovers according to Equation (2.6). 63.2% recovery of M_z can be observed at t of T_1.

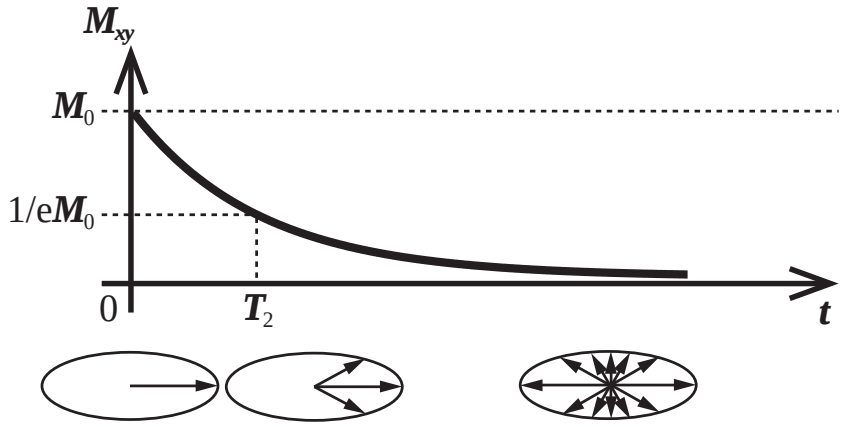

Figure 2.5: T_2 relaxation curve. Transverse component M_{xy} decay according to Equation (2.7) after the RF pulse is turned off. 36.8% decay of M_{xy} can be observed at t of T_2.

Once the π pulse turned on, the magnetization M is flipped into the x-y plane, decreasing M_z to 0 and making M_{xy} oscillate around the z-axis with all protons precessing in phase. After the magnetization M is flipped into the x-y plane, the π pulse is turned off and all protons become to go back to the lowest energy state based on a general principle of thermodynamics. The flipped magnetization is thus aligned with the axis of the B_0 magnetic field, which is the equilibrium state. In addition, all the proton spins get out of phase with each other. Consequently, M_z will have a maximum value, and M_{xy} will be 0 because the proton spins precess around the z-axis with no phase coherence at equilibrium state. This return is referred to as relaxation, and those in M_z and M_{xy} are described as longitudinal and transverse relaxation, respectively; the longitudinal relaxation recovers M_z along z-axis slowly and the transverse relaxation decreases M_{xy} rapidly.

M_z during the longitudinal relaxation can be formulated as

$$M_z(t) = M_0 \left\{ 1 - \exp\left(-\frac{t}{T_1} \right) \right\}, \tag{2.6}$$

where M_0 and T_1 are initial magnetization and T_1 relaxation time, respectively. T_1 is also called longitudinal relaxation time and denotes how quickly M_z recovers to the equilibrium state (Figure 2.4).

M_{xy} during the transverse relaxation is also formulated as

$$M_{xy}(t) = M_0 \exp\left(-\frac{t}{T_2} \right), \tag{2.7}$$

where T_2 is T_2 relaxation time, which is also called transverse relaxation time. It denotes the rate of M_{xy} decay (Figure 2.5). T_2 decay usually occurs 5 to 10 times more rapidly than T_1 recovery because of the spin-spin interactions caused by internal magnetic field inhomogeneities.

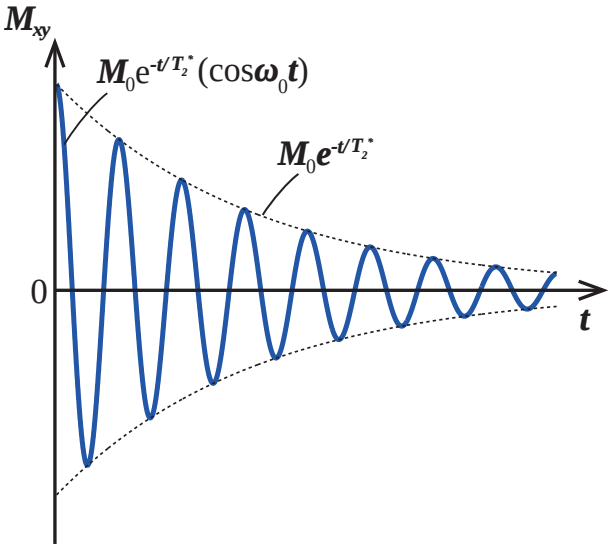

Figure 2.6: Free induction decay (FID). Behavior of oscillating and decaying transverse magnetization M_{xy}. Amplitude of M_{xy} decreases according to T_2^* relaxation.

Moreover, considering the external magnetic field inhomogeneities, M_{xy} decays at a rate characterized by T_2^* instead of T_2. Different from T_2, which depends only on spin-spin interactions and have fixed value, T_2^* depends on external magnetic field inhomogeneities and is not fixed. The relation between T_2 and T_2^* is described by the following equation, when the magnetic field inhomogeneity of the external magnet is ΔB,

$$\frac{1}{T_2^*} = \frac{1}{T_2} + \gamma \Delta B. \tag{2.8}$$

As is obvious from the equation, T_2^* is always less than T_2, therefore, T_2^* decay is always faster than T_2 decay.

MR signals are received at receiver coil, which is placed perpendicularly to the transverse magnetization plane. The RF transmitter coil is often used as a receiver coil. During the relaxation of the magnetization, M_{xy} rotates around the z-axis in the x-y plane at frequency ω_0 and decays by T_2^* relaxation. It induces an oscillating and decaying signal in the receiver coil (Figure 2.6). This signal is called free induction decay (FID) and it is described mathematically as

$$M_{xy}(t) = M_0 \exp\left(-\frac{t}{T_2^*}\right)(\cos\omega_0 t). \tag{2.9}$$

2.1.2 Image acquisition of MRI

In a actual measurement of signals with a patient in a large magnetic field, spatially encode is required. As described above, transmitting the RF pulse to the protons in the

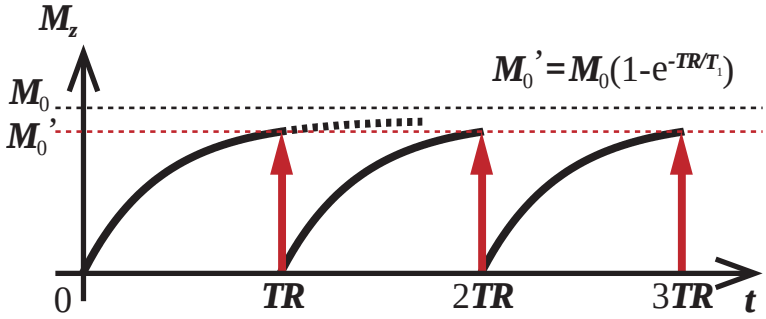

Figure 2.7: Series of exponential curves of T_1 relaxation. Longitudinal component of the magnetization M_z never reaches the initial equilibrium state.

patient provides a FID, but it is one signal (one FID) from the entire patient. To obtain spatial information, spatially encode using gradient coils is necessary. Gradient coils is used for creating gradient magnetic fields which specify the x, y and z coordinates of the signal. To spatially encored the signals, it is necessary to repeat the number of obtaining FIDs, that is, the number of applying the RF pulse.

Repeating the application of the RF pulse means that we apply another RF pulse after we apply one RF pulse. The time interval of these RF pulses is called repetition time (TR). Here, we apply the first RF pulse at $t = 0$ considering the $\pi/2$ pulse as RF pulse. At the point of $t = 0$, the initial magnetization is aligned along the z-axis with the amplitude of M_0: $M_z = M_0$ and $M_{xy} = 0$. Immediately after $t = 0$, the magnetization is flipped into the x-y plane and we obtain M_z of 0 and M_{xy} of M_0. As time goes by, we obtain recovering M_z and decaying M_{xy}. Assuming M_{xy} is very small at $t = \mathrm{TR}$, we can describe M_z at $t = \mathrm{TR}$ as

$$M_z(TR) = M_0 \left\{ 1 - \exp\left(-\frac{TR}{T_1} \right) \right\}. \tag{2.10}$$

Since the second $\pi/2$ pulse is applied earlier than M_z recover completely, M_z at time TR is less than the initial magnetization M_0. Then, the second $\pi/2$ pulse is applied and the magnetization is flipped into the x-y plane again. Therefore, a series of exponential curves that never reach full magnetization can be obtained as shown in Figure 2.7.

In addition to the influences of recover time, the magnetization depends on proton densities (spin densities) in the patient. It indicates how many protons that are mobile enough to change direction according to the external magnetic field. Here, we describe M_z at $t = \mathrm{TR}$ considering the proton density $N(\mathrm{H})$ as

$$M_z = N(\mathrm{H}) \left\{ 1 - \exp\left(-\frac{TR}{T_1} \right) \right\}. \tag{2.11}$$

As described in Subsection 2.1.1, the signal is observed in MRI measurement through the induced current in the receiver coil by the oscillating M_{xy}. Thus, the signal S is

proportional to the M_z component at time TR:

$$S \propto N(\mathrm{H}) \left\{ 1 - \exp\left(-\frac{TR}{T_1} \right) \right\}. \tag{2.12}$$

Another factor which determines the signal of MRI is echo time (TE). There is a short interval, which is referred to as TE, between the application of the $\pi/2$ pulse and the signal acquisition in actual measurement. The signal is thus affected by the magnetization decays at rate T_2^*. After a time TE, the signal can be measured as

$$\begin{aligned} S &\propto M_z(TR) \exp\left(-\frac{TE}{T_2^*} \right) \\ &= N(\mathrm{H}) \left\{ 1 - \exp\left(-\frac{TR}{T_1} \right) \right\} \exp\left(-\frac{TE}{T_2^*} \right). \end{aligned} \tag{2.13}$$

Equation (2.13) includes two variables: TR and TE, and three invariables: T_1, T_2^* and $N(\mathrm{H})$. These three invariables are determined by tissues. To differentiate various tissues based on these characters, TR and TE are properly chosen. For example, longer TR reduces the T_1 effect because (1 - e^{-TR/T_1}) approaches 1 if TR goes infinity. On the other hands, short TR enhances the T_1. As for TE, it affects T_2^* contrast; short TE reduces the T_2^* contrast because the very short TE leads e^{-TE/T_2^*} to 1. Of course long TE enhances the T_2^* contrast.

There are three types of contrast weighted imaging methods based on these characters of TR and TE: T_1-weighted, T_2-weighted and proton density weighted images. In the MRI measurement, the transverse magnetization decays according to not T_2^* but T_2 relaxation time if we use a method which eliminates external magnetic field inhomogeneities. Here, we consider T_2 relaxation for the transverse magnetization to deal with T_2-weighted imaging As well as T_2^* contrast, T_2 contrast depends on TE; short TE reduces the T_2 effect and long TE enhances the T_2 effect.

First, T_1-weighted images can be obtained by choosing short TR and short TE and enhancing the T_1 effect and reduce the T_2 effect. On the other hand long TR and long TE are used for T_2 weighted imaging because they enhance the T_2 effect and reduce the T_1 effect. Moreover, long TR and short TE are preferable to proton density weighed imaging. These three type of contrast weighted images are used properly depending on purposes (Figure 2.8).

2.1.3 Pulse sequences

A pulse sequence is a sequence of RF pulses. For acquisition of MR images, it is necessary to repeat applying the RF pulses. As well as TR and TE stated in the previous subsection, contrast of MR images depend on the kind of pulses: $\pi/2$, π RF pulses or RF pulse which have other flip angle, and the order of these pulses. Here, we describe two types of

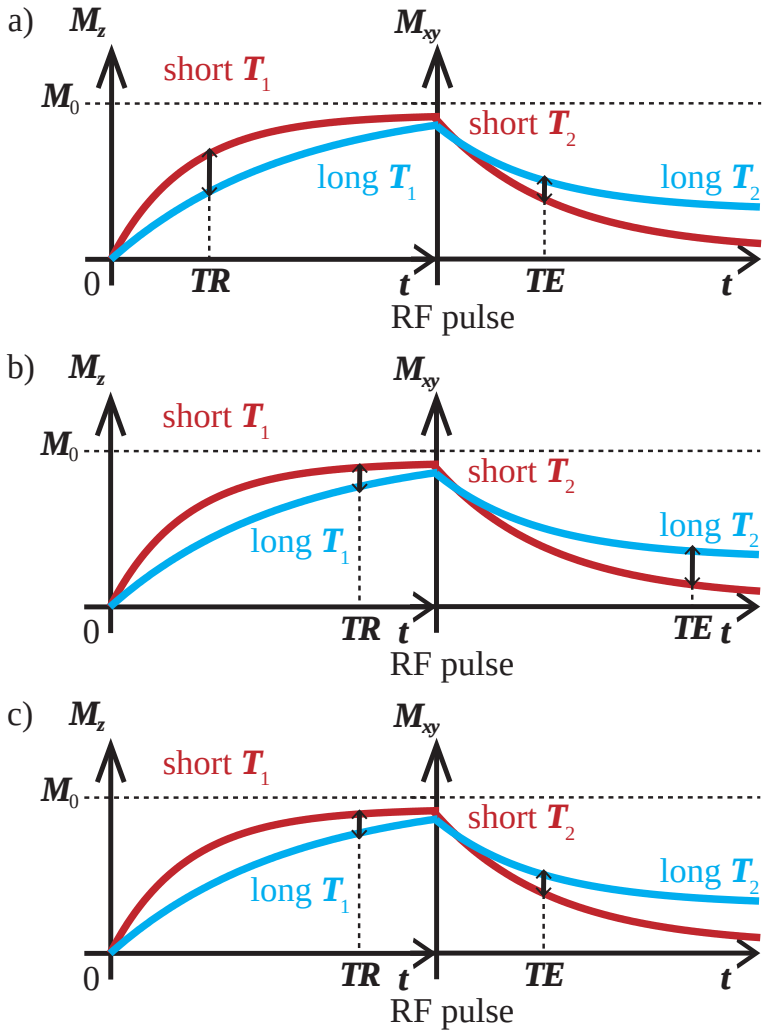

Figure 2.8: T_1 and T_2 relaxation curves of two different tissues which have long relaxation time (blue) and short relaxation time (red). Short TR enhances T_1 effect and short TE has little influence on T_2 difference; contrast by T_1 is remarkable (a). Long TR reduce T_1 effect and long TE enhances T_2 effect; contrast by T_2 is remarkable (b). Long TR and short TE make little difference; contrast by proton density are obtained (c).

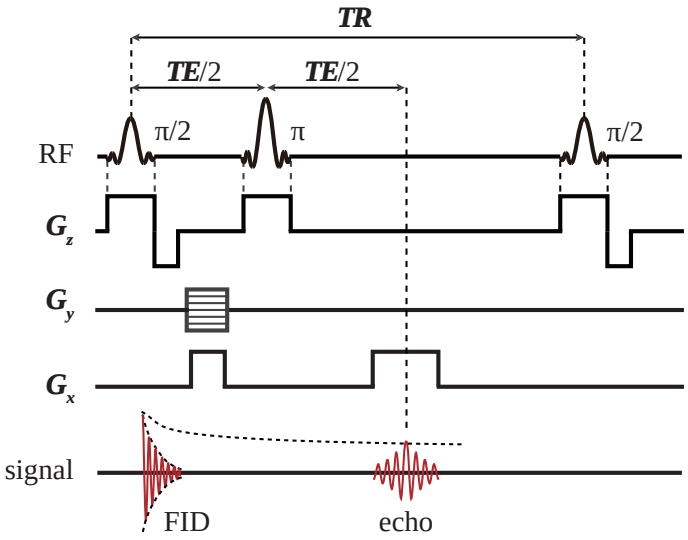

Figure 2.9: Spin echo pulse sequence.

fundamental and conventional pulse sequence: spin echo (SE) pulse sequence and gradient echo (GE) pulse sequence. In addition, we describe fast imaging methods which is used to obtain MR images, echo planner imaging (EPI) and fast spin echo (FSE).

Spin echo (SE) pulse sequence

The SE pulse sequence is the most frequently used for MRI. It has advantages to eliminate external magnetic inhomogeneities, which we discussed in Subsection 2.1.1, by applying rephasing π pulse in addition to excitation $\pi/2$ pulse.

We demonstrates the SE pulse sequence in Figure 2.9. The $\pi/2$ pulse is used for excitation of the magnetization. It flips M_z which is aligned along longitudinal axis into the transverse plane. Immediately after the $\pi/2$ pulse is applied, all the spins are in phase and begin to precess at frequency ω_0. However, they gradually get out of phase with each other because of the external magnetic inhomogeneities and spin-spin interactions. After time τ the π pulse is applied and all the spins flip π in the transverse x-y plane; they continue precessing but in the opposite direction. Therefore, after an equal time τ, they will get in phase again producing a maximum signal. With this rephasing process, the SE pulse sequence eliminates the external magnetic inhomogeneities (but not spin-spin interactions). We usually use $TE/2$ as τ.

Gradient echo (GE) pulse sequence

The GE pulse sequence uses partial flip angle techniques. In this techniques, small flip angles are employed for a excitation RF pulse to reduce TR. Consequently, we can reduce

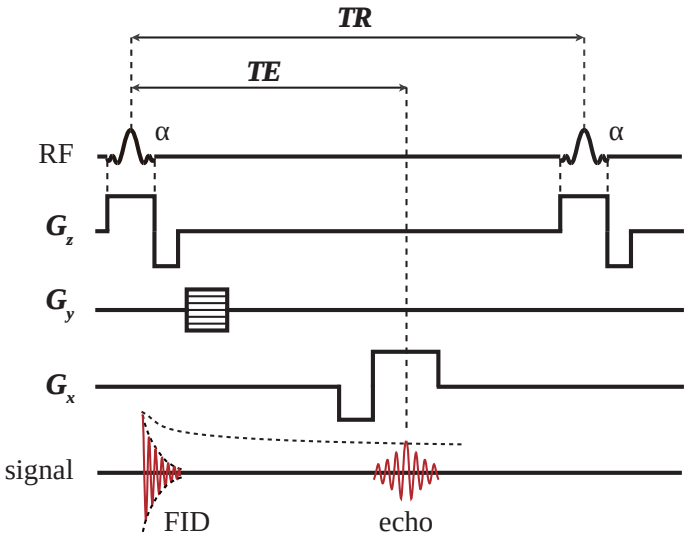

Figure 2.10: Gradient echo pulse sequence.

scan time and therefore, GE pulse sequence has ability to employ three-dimensional (3D) imaging.

If we employ small flip angles for the excitation RF pulse, the major component of M_z remains along z-axis after applying the excitation pulse. As a result, we will obtain sufficient M_z at the point of next excitation even if we use short TR. However, since the major component of M_z remains along z-axis, π pulse cannot be used for obtaining echo, that is, the signal. We therefore employ a refocusing gradient in the x direction instead of refocusing π pulse as shown in Figure 2.10. The reforcusing gradient can be divided into two parts. The first lobe is negative gradient which dephases the spins in the transverse plane. The second lobe is positive gradient which rephases the spins and then, we can observe echo, that is, the signal.

Although the GE pulse sequence has an advantage of reduction of scan time, it has a disadvantage that it cannot eliminate the external magnetic field inhomogeneities different from the SE pulse sequence. We therefore need to consider T_2^* relaxation and obtain T_2^*-weighted images with the GE pulse sequence.

Echo planar imaging (EPI)

EPI is one of the fast scanning techniques. It can collect all the echoes which is necessary for phase encoding in one or multiple shot with rapid on-and-off switching of y-axis gradients.

We represent pulse sequence for EPI in Figure 2.11. Single-shot EPI collects all the echoes needed for phase encoding by multiple gradient reversals in a single acquisition

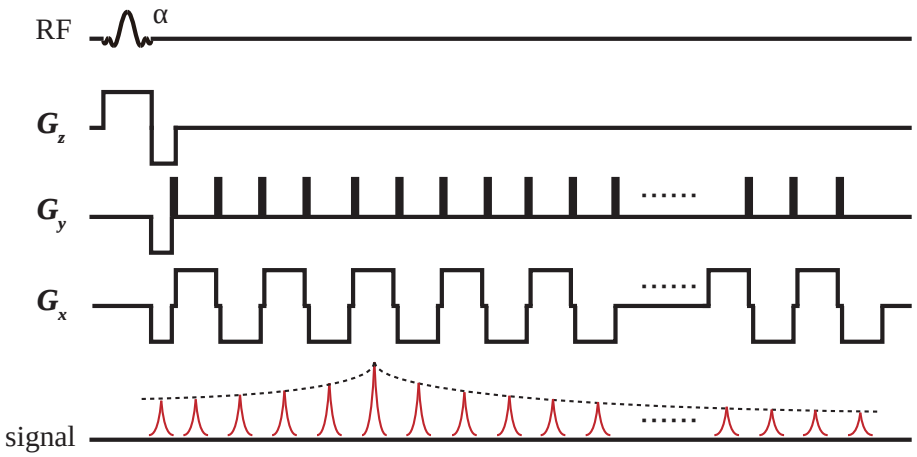

Figure 2.11: Pulse sequence of echo planar imaging.

after applying a single RF excitation pulse. The y-axis gradient reverses rapidly from maximum positive to maximum negative $N_y/2$ times (N_y: necessary repetition time for phase encoding) generating N_y echos during a single T_2^* decay. Multishot EPI divides the sequence into multiple segments, that is, shot. It is also called segmented EPI. It has an advantage that there is less stress on the gradients than the single-shot EPI; however, it takes longer time.

Fast spin echo (FSE)

FSE is also one of the fast scanning techniques and was first proposed by Hennig et al. [38]. It was referred to as rapid acquisition with relaxation enhancement (RARE). However, it is usually called FSE or turbo spin echo (TSE) and hereafter, we use FSE for this method.

FSE sequence can be shown as Figure 2.12. Similar to EPI, we need to repeat phase encoding in a single acquisition after the RF excitation pulse for decreasing scan time with the FSE sequence. The point which is different from EPI is that π pulses are used for rephasing the spin and generating multiple echos during a single acquisition time. As well as EPI, FSE has an advantage of decreased scan time. In addition, it has another advantage that the rephasing from the multiple π pulses leads to less distortion from magnetic susceptibility artifact because it generates images affected by only external magnetic inhomogeneities.

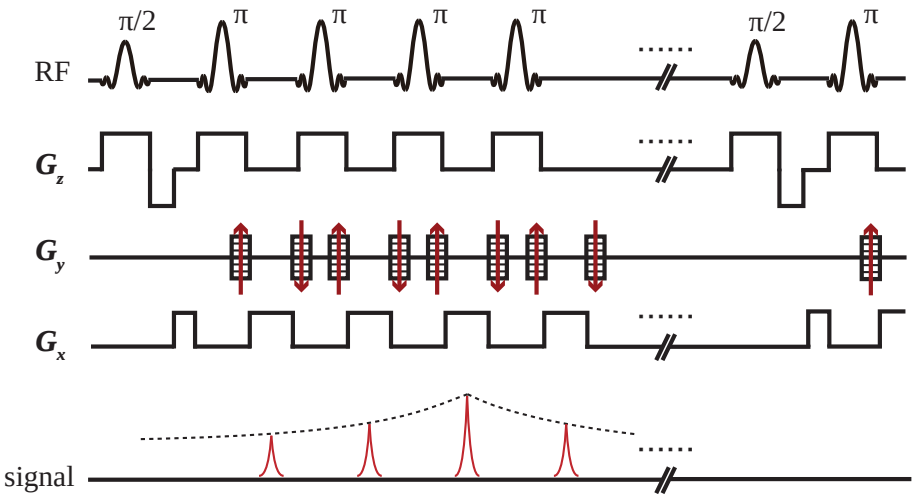

Figure 2.12: Fast spin echo pulse sequence.

2.2 Functional magnetic resonance imaging (fMRI)

FMRI measures a brain activity using MRI by measuring changes in local oxygenations of blood, which reflects the brain activity. The analysis of fMRI data is complex and requiring the use of sophisticated techniques from signal and image processing to statistical processing in order to produce final map representing which brain regions respond to stimulations.

In this section, we describe the principle of fMRI including BOLD contrast theory, analysis method with image processing and statistical processing.

2.2.1 Blood oxygenation level dependent (BOLD) contrast

Conventional fMRI takes advantage of the fact that when neurons in the brain activate, the amount of blood flowing through that area is increased. We call this phenomenon "hemodynamic response" and it has been known for more than 100 years, though the mechanisms remain only partly understood [39]. The mechanism of MR signal changes related to this blood flowing is referred to as blood oxygenation level dependent (BOLD) contrast although it is still to be determined; however, there are hypotheses to explain the observed signal changes.

Deoxyhemoglobin is a paramagnetic molecule whereas oxyhemoglobin is diamagnetic. The presence of deoxyhemoglobin in a blood vessel causes a susceptibility difference between the vessel and its surrounding tissue [7, 6]. Thus, the magnetic susceptibility of blood changes and the T_2^* value of blood water becomes short because of dephasing of proton spins caused by such susceptibility. As a result, in a T_2^*-weighted imaging experi-

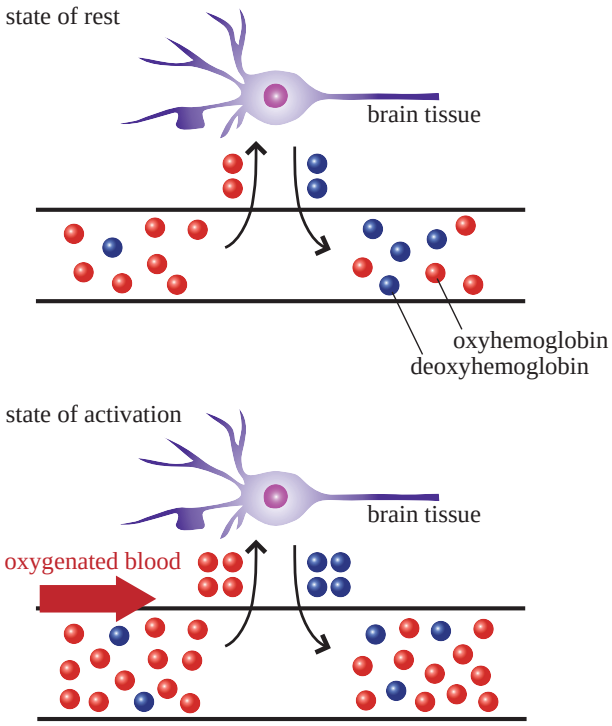

Figure 2.13: Blood oxygenation level dependent (BOLD) effect. In a state of activation, ratio of oxyhemoglobin in a blood vessel increases because of oversupplied oxygenated blood.

ment, the presence of deoxyhemoglobin in the blood vessels causes MR signal reductions in those voxels containing vessels. Since oxyhemoglobin is diamagnetic and is not affected by the dephasing and does not produce MR signal reduction, changes in oxygenation of the blood can be observed as the signal changes in T_2^*-weighted images [8, 9] This is one reason of BOLD effect.

The other reason of BOLD effect is that brain activation is characterized by a drop in the local oxygen extraction fraction and a corresponding drop in the local concentration of deoxyhemoglobin [9]. Once a neural activity occurs, the oxygen consumption is increased and the level of deoxyhemoglobin in the blood would also increases. Thus, it is expected to observe that MR signals would decrease. However, as well as the slight increase in oxygen extraction from the blood, there is a much larger increase in cerebral blood flow (CBF) delivering more oxyhemoblobin (Figure 2.13). Since they oversupply oxygenated blood and overcompensate for the consumed oxyhemoglobin, the local concentration of deoxyhemoglobin decreases [40, 41]. Thus, the observed MR signals increase in the region of the neural activity.

Although BOLD contrast has been used as a biomarker of neural activities in the fMRI measurement as described above, it's an indirect method and there are limitations related

to spatial and temporal resolutions. Based on the BOLD contrast, we observe the MR signal changes caused by local changes in the T_2^* value of blood water in vessels. Thus, the spatial resolution is limited because the vessels at the origin of the BOLD contrast feed or drain somewhat large territories compared with the activated neuronal assemblies [11]. As for temporal resolution, hemodynamic response is slow; whereas neural activities may only last milliseconds, it takes about 5 seconds to observe the increase in CBF that reaches its maximum. Moreover, after this peak there is a long undershoot that does not recover to baseline for at least 15–20 seconds [10].

2.2.2 Image processing

FMRI data is obtained as a series of MR images. It is necessary for mapping of neural activities to process these images appropriately to avoid complex problems [10]. For example, a number of artifacts, such as those caused by head movement and a number of sources of variability in the data, including variability between individuals and variability across time within individuals. Moreover, the large dimensionality of the data also causes a number of challenges.

Here, we describe four image processing which is required before analyzing the fMRI data: motion correction, slice timing correction, spatial normalization and spatial smoothing.

Motion correction

When subjects move their heads during fMRI experiments, fMRI data can be affected drastically by the motion. There are two major effects of head motion; one is that it causes a mismatch of the location of subsequent images in the time series. This is often referred to as "bulk motion" because it involves a wholesale movement of the head. The other is disruption of the MR signal itself. If the head motion occurs during the acquiring images, the protons that move into a voxel from a neighboring slice have an excitation that is different from that expected by the scanner, and the reconstructed signal will not accurately reflect the tissue in the voxel. This is referred to as a "spin history" effect [42].

The motion correction is also known as realignment. This technique is applied to reduce the misalignment between images in an fMRI time series produced by the head motion. Motion correction tools which are currently used generally assume that the position of the head can change by translation or rotation along each of the three axes, whereas the shape of the head cannot change. It can correct MR images for bulk motion, but not for spin history motion because this effect cannot be described by rotation or translation of the entire brain. Hereafter, we therefore state the motion correction for bulk motion.

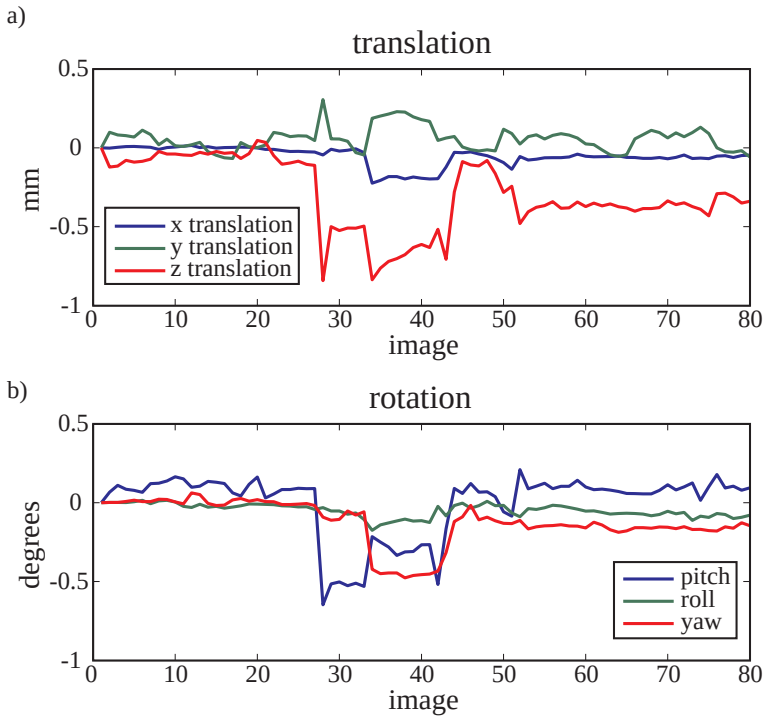

Figure 2.14: Plots of estimated head motion: translation in mm (x, y and z) a) and rotation in rad ("pitch", "roll" and "yaw") b).

The first step of motion correction is estimating motion. Figure 2.14 represents an example of head motion estimated from time series of an fMRI data, which are used for estimating parameters for the rigid body transformation: translation in mm (x, y and z) and rotation in rad ("pitch", "roll" and "yaw"). A target for the motion correction which is assumed as a reference can be a specific single image or a mean of time series. A single image is generally recommended to be used as a reference.

The second step is reslicing all the images except the reference image. Once the parameters for transformation have been estimated, they are applied to the original images to create transformed, or resliced images. All the original images are transformed using these estimated parameters along the reference image and rescliced images will be created using a number of interpolation methods.

However, although we can apply motion correction to fMRI data, there are cases that we should dispose the entire data because of too much head motions of patients. If sudden motion occurs during a scan, there will be likely effects on MR images which cannot be corrected using a rigid-body transformation. As a general rule, any translation displacement of more than half of the voxel dimension should be thrown away owing to unreliability of data.

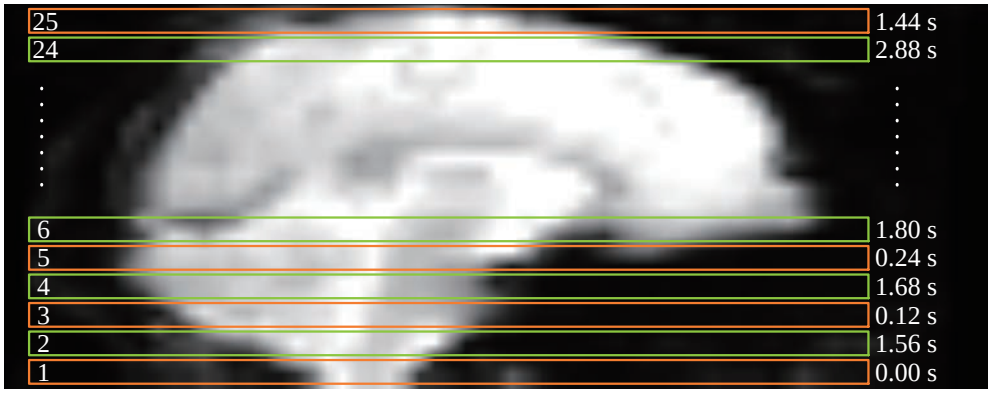

Figure 2.15: Slice timing in an interleaved MRI acquisition. The slices are acquired in the order 1-3-5-7-· · ·-25-2-4-· · ·-24. If we set the number of slice of 25 and TR of 3.00 s, it takes 0.12 s to acquire one slice. The times on the right side represent the time at which the data in the slice starts being acquired.

Slice timing correction

Most of all fMRI data are collected two dimensionally and data for one slice is acquired at a time. The order of acquiring slices depends on the case: ascending, descending or another order known as interleaved acquisition. In interleaved acquisition, every other slice is acquired sequentially, such that half of the slices are acquired followed by the other half. This means that data in different slices are acquired at systematically different times, and these differences range up several seconds depending upon the TR of the pulse sequence (Figure 2.15). These differences in acquisition time, which we usually call slice timing, are problematic for the fMRI analysis. In a fMRI analysis, the time of events such as trials in a task are used to create a statistical model expecting that signals would be evoked by the task; the analysis assumes that all data were obtained at the same timing, and therefore there is mismatch between the model and the data.

Slice timing correction is necessary to overcome this mismatch between the acquisition timing of different slices. The most common approach for the slice timing correction is determining a reference slice and interpolate the data in all other slices to match the timing of the reference slice. For this correction, it is required to know the exact timing of the acquisition, of which is generally calculated by TR, the number of slices and the slice order.

Spatial normalization

In fMRI measurement, we wish to generalize across individuals so that we could apply brain functions to our species more broadly. This requires the data of fMRI to be integrated across individuals; however, there are many differences in the size and shape

of individual brains. Therefore, they should be transformed to align with one another by using a reference frame, that is "template", which is a representative image of the atlas and provides a target to which individual can be aligned. This transformation is known as "intersubject registration" or "spatial normalization" and a set of both linear and nonlinear registration methods is often used.

There are two commonly used methods for the spatial normalization of fMRI data. One is referred to as "prestatistics normalization", where the data are preprocessed and spatially normalized prior to statistical analysis. The other is referred to as "poststatistics normalization", where the data preprocessed and the statistical analysis is performed on data in the native space. In poststatistics normalization, the normalization is applied to the statistical result images. Choice of each method usually depends on the software package used for analysis. The poststatistics normalization has a merit to use disk space economically; however, it also has a problem that values of voxels outside the brain are stored as NaN ("not a number"). To solve the problem the NaN values have to be replaced with zeros in the image for further analysis.

Spatial smoothing

Spatial smoothing, which is the application of a filter to images, is applied to remove high-frequency component. An example of smoothing fMRI data is shown in Figure 2.16. The first advantage of spatial smoothing is increasing the signal-to-noise ratio for signals with larger spatial scales by removing high-frequency information. In addition, the acquisition of smaller voxels can help reduce dropout in regions of susceptibility artifacts, and smoothing can help overcome the increased noise that occurs when small vexels are used. Second, when data are combined across individuals, there may be variability in the spatial location of functional regions that is not corrected by spatial normalization. Spatial smoothing can reduce the variabilities across individuals. Therefore, for the analysis methods, a specific degree of spatial smoothness is required.

The most commonly used spatial smoothing method is applying the convolution of the three-dimensional image with a three-dimensional Gaussian filter (or kernel). The amount of smoothing is determined by the width of the distribution, which is described as the full width at half-maximum; the larger value provides the greater smoothing.

2.2.3 Statistical analysis

After image processing mentioned above, statistical modeling is applied to processed fMRI data to obtain final results of activation map. We would like to detect voxels which have time series that match the pattern of stimulus application. There are two processes of statistical analysis: statistical modeling and statistical inference.

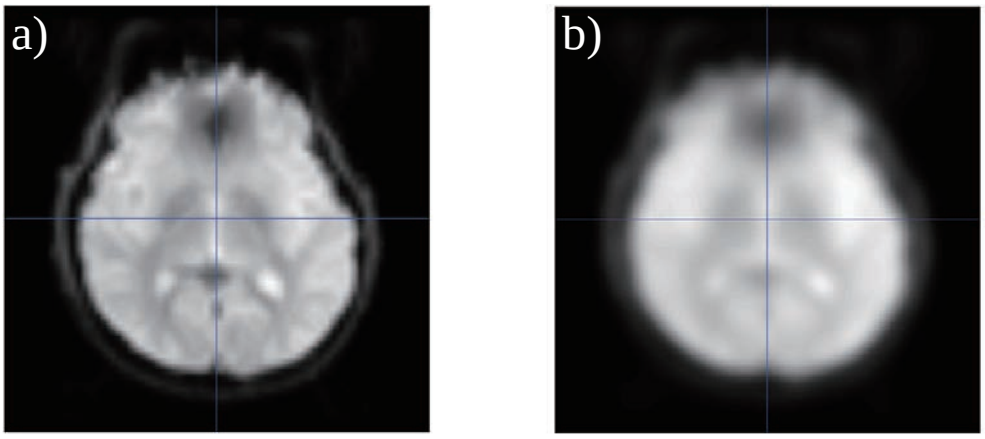

Figure 2.16: An example of application of spatial smoothing to fMRI data. An axial slice before a) and after b) spatial smoothing.

Statistical modeling

The first process of statistical analysis is statistical modeling of expected BOLD signal. Its goal is to determine the modeled function of expected BOLD signal based on a provided time series of stimulus and to analyze each voxel's time series to see whether the BOLD signal changes in response to the stimulus. The tool used for this determination is the general linear model (GLM), where a time course of observed BOLD signal plays the role of dependent variable and the independent variables is provided stimulus time series. In an actual analysis, a basis function is used for the stimulus time series; a hemodynamic response function (HRF) is generally chosen.

The HRF shown in Figure 2.17 is the ideal noiseless response to an infinitesimally brief stimulus. It is considered to have initial dip and poststimulus undershoot before and after the peak, respectively. The initial dip is identified by some studies that it occurs within the first 1–2 seconds and is thought to reflect early oxygen consumption [9]; however, it is generally very small compared to the peak positive BOLD response and is generally ignored in most models of fMRI data. The poststimulus undershoot is a late undershoot, which is relatively small in amplitude and persists up to 20 seconds or more after stimulus. A peak height of positive BOLD response is most directly related to neural activity [43], and the maximum amplitude is about 5% for the primary sensory stimulation in BOLD-fMRI. A time to peak and a width are generally 4–6 and 1–2 seconds, respectively.

The GLM approach to fMRI analysis depends on the assumption that observed BOLD signals are linear transformation of underlying neural signals. Therefore, a BOLD signal model reflecting the neural signals is required when being compared with the observed BOLD signals. A natural approach to creating the BOLD signal model from provided neural signals is using the convolution operation (Figure 2.18). In the operation, the

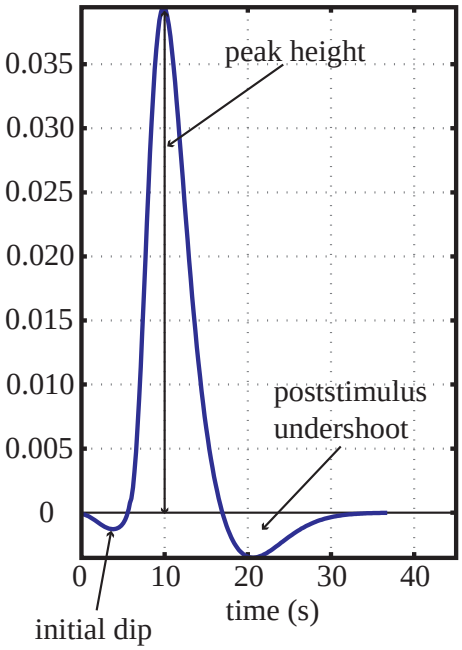

Figure 2.17: An example of the hemodynamic response. This is referred to as hemodynamic response function (HRF). The HRF usually has the initial dip and poststimulus undershoot before and after the peak, respectively.

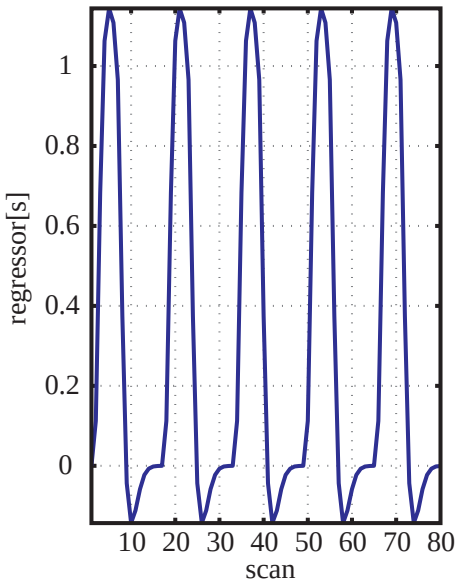

Figure 2.18: Time domain regressors created by convolution of stimulus design and HRF. It is used for the GLM approach to fMRI analysis.

stimulus onset time series, f, is blended with an appropriately chosen basis function (e.g., HRF), h, creating a result function:

$$(h * f)(t) = \int h(\tau) f(t - \tau) d\tau, \tag{2.14}$$

where τ is a time delay between the function h and f. The obtained function, that is, the expected BOLD signal model has a shape that more closely represents the shape of the BOLD response reflecting the task design of stimulus.

Statistical inference

Statistical inference is the second process of statistical analysis carried out after the modeling of BOLD signals. Its goal is to make decisions to create activation maps (Figure 2.19) based on the fMRI data and obtained BOLD signal model accounting for uncertainty due to noise in the data. If we think about an image composed of V voxels, there are mainly two kinds of approaches for statistical inference; "voxel-level" and "cluster-level" inference.

In voxel level inference, we statistically determine where there are significant differences between the fMRI data and the BOLD signal model by testing each and every voxel individually. Specifically, by examining whether the statistic at each voxel exceeds a threshold, we can determine where there is a significant effect at each individual voxel. If the statistic at a voxel exceeds the threshold, we regard that voxel as "significant".

We can take into account the spatial information available in a image by finding connected clusters of activated voxels and testing the significance of each cluster using cluster-level inference. In actual measurement, we generally expect that fMRI data is spatially extended because the brain regions of activation are often much larger than the size of one voxel and fMRI data are often spatially smoothed. Cluster-level inference is generally more sensitive than voxel-level inference for standard MRI data; however it has a disadvantage of less spatial specificity or precision.

2.3 Diffusion weighted imaging (DWI)

Diffusion weighted imaging can probe and image tissue structure on a microscopic scale. It provides unique information of the fine architecture of neural tissues in brain by visualizing the water self-diffusion, which means a motion of water molecules. This technique is used to observe anatomical structure or changes related to various physiological and pathological states, such as acute brain ischemia [13]. In this section, we explain the principle of DWI.

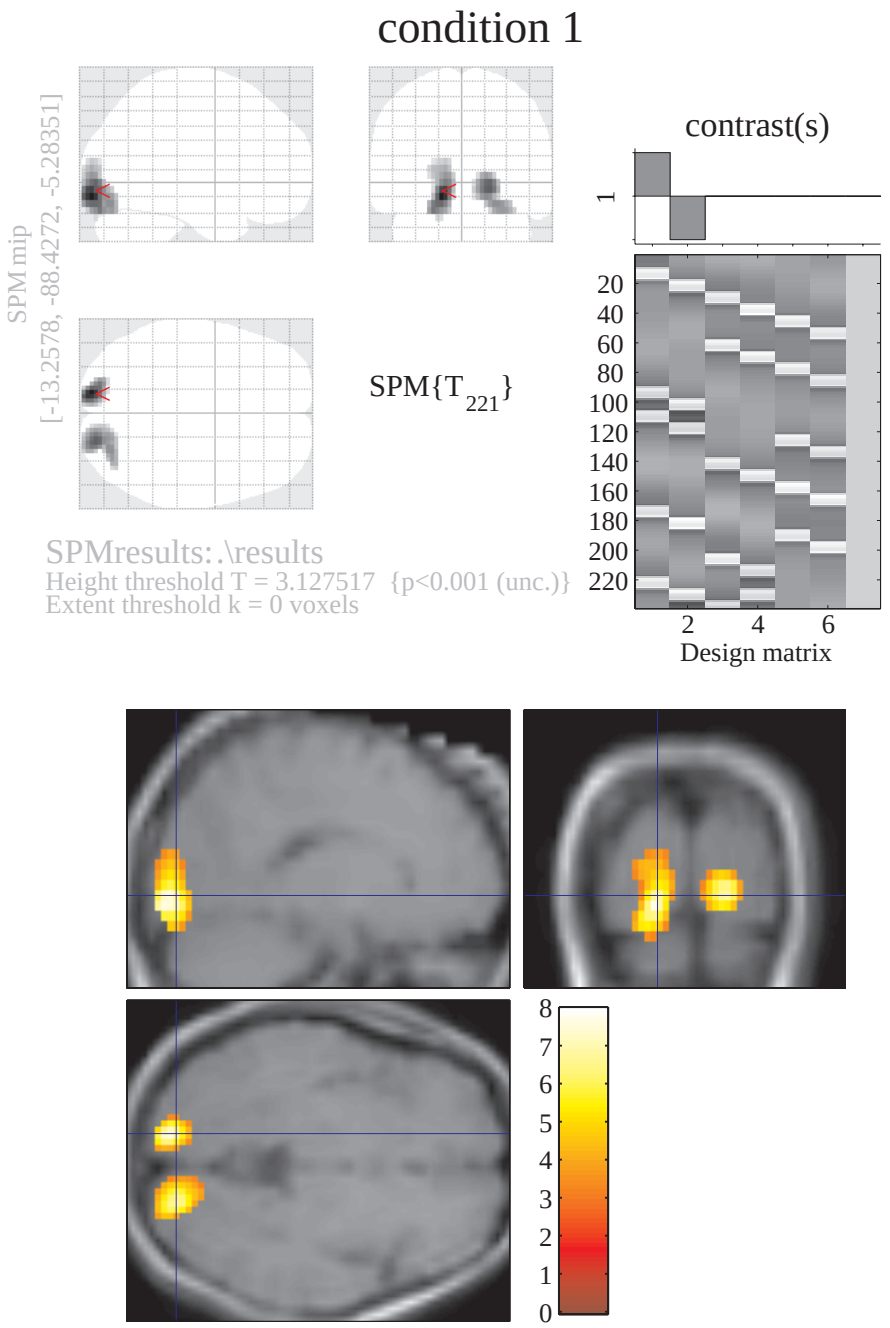

Figure 2.19: An example of activation map of the brain obtained with SPM 8 software. This result demonstrates that there is activation in the region which is related to the visual processing (the primary visual cortex) when a patient is presented a visual stimulus.

2.3.1 Diffusion of water molecules

Water molecules move referring to the thermal energy carried by themselves. Particles surrounded by water molecules move affected by collisions with these water molecules. It is called "Brownian motion" and its physical process was well characterized by Einstein [44]. We also call these particles "Brownian particle" and their random translational motion make them move to where there are less particles from where there are more particles. Therefore, the Brownian motion make a non-equilibrium solution reach equilibrium; the Brownian motion causes diffusion phenomenon.

In MRI measurement, the target is protons included in water molecules. In this case, water molecules are Brownian particles and diffusion phenomenon with only water molecules are called "self diffusion".

The diffusion phenomenon is demonstrated by diffusion equation. The diffusion equation is derived from Fick's laws of diffusion [12]. Fick's law was postulated that the flux of material across a given plane is proportional to the concentration gradient across the plane. Fick's law usually indicates Fick's first law. If only the diffusion along the x axis is considered, it states as

$$N(x,t) = -D\frac{\partial c(x,t)}{\partial x}, \tag{2.15}$$

where $N(x,t)$, $c(x,t)$ and D are the number of molecules moving through the plane at a location x per unit area at a time point t, a concentration at x and a diffusion coefficient, respectively. The unit of D is m^2/s, where the unit of $N(x,t)$ is the number per $\mathrm{m}^2\mathrm{s}$.

Here, assuming a minute distance dx adjacent to a location x, we consider a thin column with a sectional area of S, a width of ds and a volume of $V = Sdx$. The number of molecules that flow in V per unit time is $N(x)S$, which is equal to that of molecules passing the S. The number of molecules that flow out V per unit time is $N(x+dx)S$ and we therefore can describe the number of molecules which increase in V during minute time dt as

$$dN = S[N(x) - N(x+dx)]dt. \tag{2.16}$$

Transforming this equation, we obtain

$$\frac{dN}{dt} = S[N(x) - N(x+dx)]. \tag{2.17}$$

Based on the relation of $Sdx = V$, the equation can be rewrite as

$$\frac{1}{V}\left(\frac{dN}{dt}\right) = \frac{N(x) - N(x+dx)}{dx}. \tag{2.18}$$

The number of molecules per unit volume N/V represents the concentration c. Since the concentration c depends on both of a location x and a time point t, we introduce partial

differentiation and transform the equation:

$$\frac{\partial c}{\partial t} = \frac{N(x) - N(x+dx)}{dx}. \tag{2.19}$$

Here, we apply the relation below to Equation (2.19) because c is continuous function of t and x:

$$\frac{\partial N}{\partial x} = \frac{N(x+dx) - N(x)}{dx}. \tag{2.20}$$

From Equations (2.19) and (2.20), the relational expression is derived as

$$\frac{\partial c}{\partial t} = -\frac{\partial N}{\partial x}. \tag{2.21}$$

We calculate the partial differentiation for x to the both side of Equation (2.15),

$$\frac{\partial N}{\partial x} = -D\frac{\partial^2 c}{\partial x^2}. \tag{2.22}$$

Then, the diffusion equation expressed in a partial differential equation of second order is derived from Equations (2.21) and (2.22) as

$$\frac{\partial c}{\partial t} = D\frac{\partial^2 c}{\partial x^2}. \tag{2.23}$$

This equation is also called Fick's second law.

Now, we obtained the diffusion equation, which demonstrates the diffusion phenomenon, and we therefore need to solve this equation. The diffusion equation is solved for c under two boundary conditions: one is that $c(x,t) = 0$ in all location x except for $x = 0$ at time point $t = 0$, and the other is that $\int c(x,t)dx = 1$.

$$c(x,t) = \frac{1}{\sqrt{4\pi Dt}} \exp\left(\frac{-x^2}{4Dt}\right). \tag{2.24}$$

This equation indicates Gaussian distribution with the mean square displacement $\sigma^2 = \langle x^2 \rangle = 2Dt$ with respect to the origin of the coordinate axes. In other words, the diffusion phenomenon follows the Gaussian distribution.

We explain a diffusion phenomenon focusing on water molecules placed in a sufficiently wide space; this is referred to as free diffusion. In contrast, a diffusion phenomenon of water molecules placed in a restricted space is called restricted diffusion (Figure 2.20).

Again we begin with only the diffusion along the x axis and assume an obstacle at points which are d away from the origin. If the molecules reach $\pm d$ after a certain time, they are bounced and cannot pass the obstacle. Therefore, we represents a restriction of mean square displacement of water molecules $\langle x^2 \rangle$ as

$$\left\langle x^2 \right\rangle \leq d^2. \tag{2.25}$$

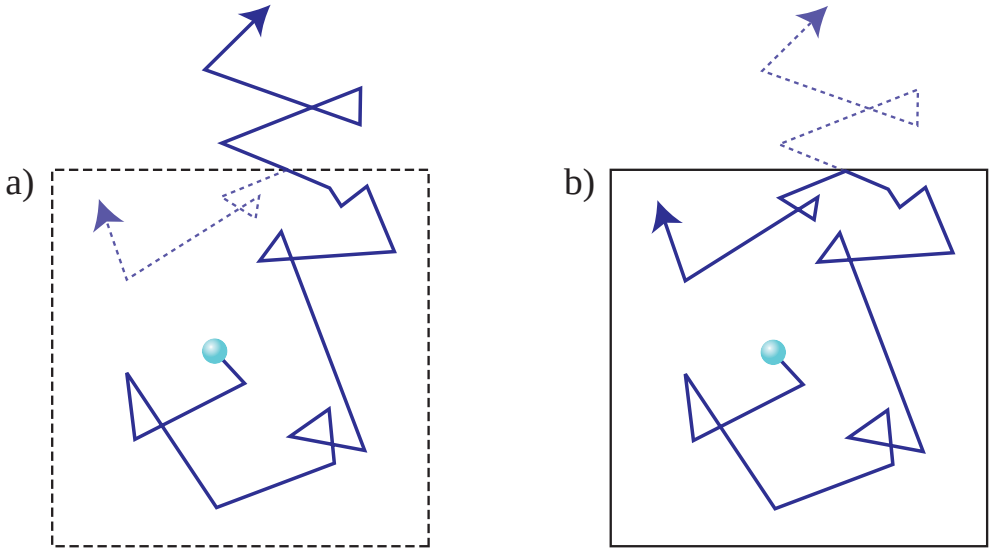

Figure 2.20: Movement of water molecules in case of free diffusion (a) and restricted diffusion (b). Water molecules can not pass through the obstacle and are bounced in case of the restricted diffusion.

Here, Einstein-Smoluchowski's equation provides the equation below

$$\langle x^2 \rangle = 2Dt. \tag{2.26}$$

From $2Dt \leq d^2$, we obtain

$$D \leq \frac{d^2}{2t}. \tag{2.27}$$

Consequently, the molecules diffuse freely and $\langle x^2 \rangle$ increases proportionally to t at the beginning, however, $\langle x^2 \rangle$ gradually stops increasing and finally the observed diffusion coefficient decreases with the increase of t because they cannot diffuse over the obstacle and $\langle x^2 \rangle$ dose not increase.

2.3.2 Basic principles of DWI

By combining MRI principles with NMR physics and chemistry to encode molecular diffusion effects, it becomes possible to obtain local measurement of water diffusion in vivo. The use of a pair of magnetic field gradient pulses [45] makes MR signals sensitive to diffusion. A sequence for this diffusion imaging is shown in Figure 2.21. The pair of magnetic field gradient, which is called motion probing gradient (MPG), is added to the spin-ehco pulse sequence and each gradient is set before and after the π refocusing pulse, respectively. They have the same amplitude $\boldsymbol{G}$ and duration time δ, and the interval time between them is called separation time Δ.

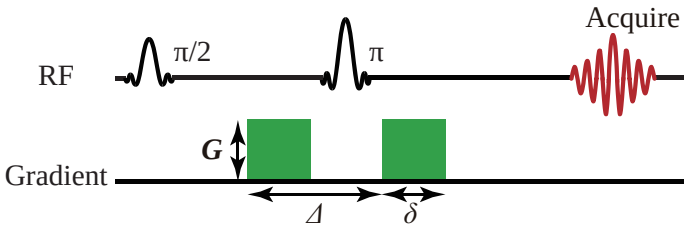

Figure 2.21: Stejskal-Tanner's pulse sequence that is generally used for DWI. A pair of gradients with the same amplitude $\boldsymbol{G}$ and period δ on both sides of the π reforcus pulse.

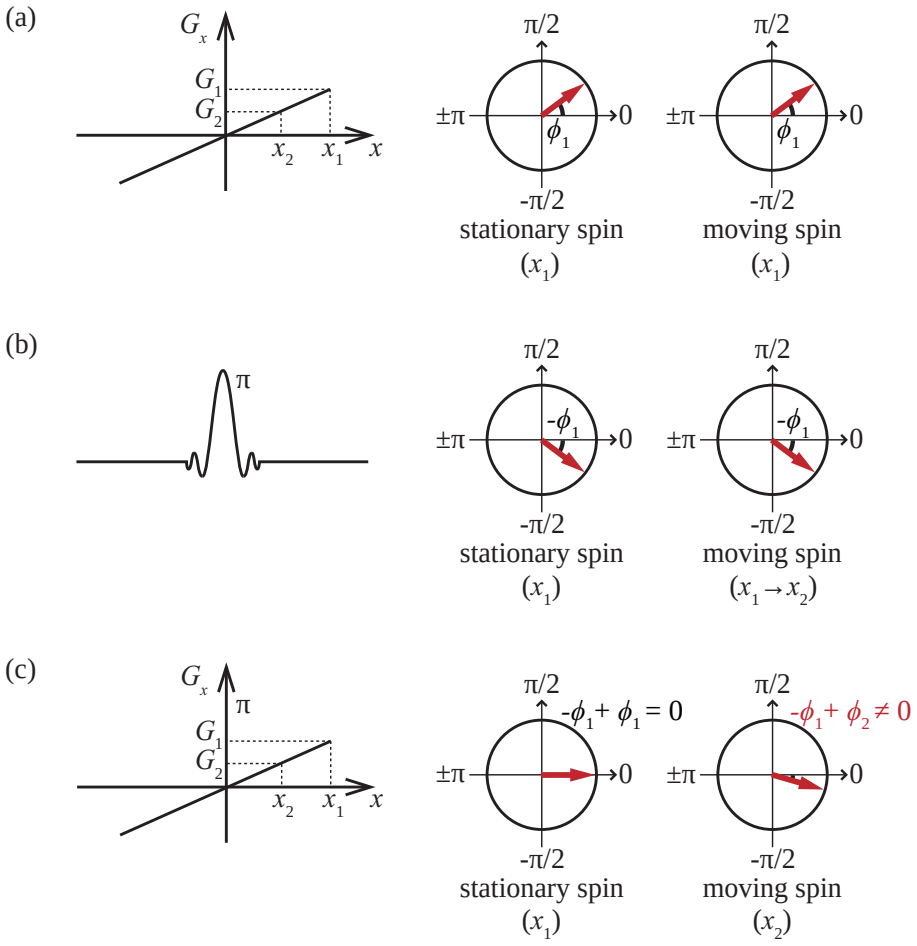

Figure 2.22: Phase shift of magnetization of stationary spin and moving spin during DWI measurement. The first MPG generates phase shift of each spin (a). Refocusing pulse inverts phase shift of each spin (b). The second MPG also generates phase shift, which cancels out the phase shift of the stationary spin while leaves that of the moving spin (c).

The MPGs affect phase of spins of hydrogen protons included in water molecules [12, 46]. During the first pulse of MPG, which is switched on at time t_1 and off at time t_2, spins are magnetically "labeled" according to their spatial location. If we consider diffusion of water molecules only in x-axis, each spin experiences a phase shift (Figure 2.22 (a)):

$$\phi^{(1)}(x,t) = \gamma \int_{t_1}^{t_2} G_x(t) \cdot x(t) dt, \tag{2.28}$$

where G_x and x are the amplitude of the MPG and the displacement of the spin at time t. γ is gyromagnetic ratio and its unit is rad/(Ts) here. If we assume the gradient is constant during the MPGs, Equation (2.28) can be rewrite as

$$\phi^{(1)}(x,t) = \gamma G_x \cdot \int_{t_1}^{t_2} x(t) dt. \tag{2.29}$$

A π refocusing pulse occurs at the end of the first pulse of MPG. This flips the phases of all spins (Figure 2.22 (b)). The second pulse of MPG is switched on at time $t_3 = t_1 + \Delta$ and off at time $t_4 = t_3 + \delta$. Each spin also experiences a phase shift (Figure 2.22 (c)):

$$\phi^{(2)}(x,t) = G_x \cdot \int_{t_3}^{t_4} x(t) dt. \tag{2.30}$$

The net phase shift at the end of the second pulse of MPG is

$$\phi(x,t) = \phi^{(2)}(x,t) - \phi^{(1)}(x,t). \tag{2.31}$$

Considering that two gradient pulses of MPG have the same duration (t_2 - t_1 = t_4 - t_3), the second pulse cancels out the phase shift of a stationary spin generated by the first pulse. Since it does not move during the sequence, it experiences gradients with the same amplitude through MPGs. In contrast, in case of a moving spin, there remains a residual phase offset that depends on its path during the sequence as shown in Figure 2.22:

$$\phi(x,t) = \gamma G_x \cdot \left(\int_{t_1}^{t_2} x(t) dt - \int_{t_3}^{t_4} x(t') dt' \right). \tag{2.32}$$

Since it moves during the sequence, it experiences gradients with the different amplitudes through MPG and therefore, the net phase shift can be observed.

The phase shift of each spin causes decreases in MR signals. MR signals are calculated with $\mu \cos\phi$ and $\mu \sin\phi$ and proportional to $\sqrt{(\mu\cos\phi)^2 + (\mu\sin\phi)^2}$. Here, $\mu\cos\phi$ and $\mu\sin\phi$ indicate x and y component of each magnetic moment $\boldsymbol{\mu}$, respectively. In MRI measurement there are a lot of spins and we observe the net magnetization $\boldsymbol{M}$ which is the vectorial sum of all the magnetic moments $\boldsymbol{\mu}$. When we consider three magnetization moment and assume they remain stationary, we obtain $M = 3\mu$ (Figure 2.23 (a)). If

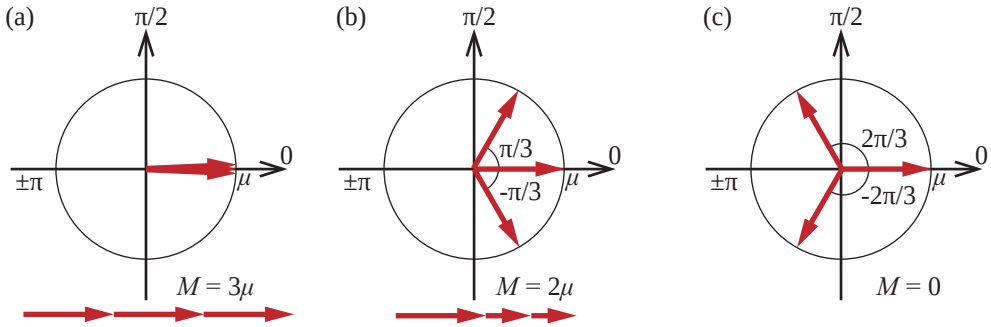

Figure 2.23: Net magnetization of three magnetic moments: three μ with no phase shift (a), with phase shift of 0 and $\pm\ \pi/3$ (b), and with phase shift of 0 and $\pm\ 2\pi/3$ (c).

they move and experience different gradients, however, they obtain various phase shifts depending on their position. For example, three μ with phase shift of 0 and $\pm\ \pi/3$ causes $M = 2\mu$ and three μ with phase shift of 0 and $\pm\ 2\pi/3$ causes $M = 0$ as shown in Figures 2.23 (b) and (c). Therefore, the vectorial sum of these magnetic moments decrease because of their various phase shifts. Consequently, this dephasing process decreases MR signals. This is the principle of DWI.

2.3.3 Signal processing

As described in the previous subsections, DWI visualizes an amplitude of diffusion as a signal decrease by dephasing the magnetic moment of diffusing water molecules. MR signals obtained in DWI are determined by the net magnetization of water molecules. Since the molecules obey the Gaussian distribution, we obtain a vectorial moment of a magnetization $2\mu\cos\phi$ in x axis from two spin moments $\boldsymbol{\mu}$, which diffuse along x axis in a symmetry.

If we consider only the diffusion along the x axis, the probability density distribution P is expressed as

$$P(x,t) = c(x,t) = (4\pi Dt)^{-\frac{1}{2}} \exp\left(\frac{-x^2}{4Dt}\right), \tag{2.33}$$

and the net magnetization M is expressed as

$$M = 2\int_0^\infty \cos\phi \cdot (4\pi Dt)^{-\frac{1}{2}} \exp\left(\frac{-x^2}{4Dt}\right) dx. \tag{2.34}$$

In case of stationary water molecules, we have the net magnetization M_0 with $\phi = 0$ and $\cos\phi = 1$:

$$M_0 = 2\int_0^\infty \cos\phi \cdot (4\pi Dt)^{-\frac{1}{2}} \exp\left(\frac{-x^2}{4Dt}\right) dx = 1. \tag{2.35}$$

In contrast, the phase shift ϕ of the moving water molecules is

$$\phi(x,t) = \gamma \int_{t_1}^{t_2} G_x(t)x(t)dt, \tag{2.36}$$

and therefore, the net magnetization of moving water molecules is obtained by substituting Equation (2.36) for Equation (2.34):

$$M = \exp\left\{-\gamma^2 D \int_0^t \left[\int_0^{t'} G_x(t'')dt''\right]^2 dt'\right\}. \tag{2.37}$$

With $M_0 = 1$, we can describe

$$\begin{aligned}
\ln\left(\frac{M}{M_0}\right) &= -\gamma^2 D \int_0^t \left[\int_0^{t'} G_x(t'')dt''\right]^2 dt' \\
&= -\gamma^2 D G_x^2 \left[\int_0^{\delta} t'^2 dt' + \int_{\delta}^{\Delta} \delta^2 dt' + \int_{\Delta}^{\Delta+\delta} (\delta - t' + \Delta)^2 dt'\right] \\
&= -\gamma^2 D G_x^2 \left[\frac{\delta^3}{3} + \left(\delta^2\Delta - \delta^3\right) + \frac{\delta^3}{3}\right] \\
&= -\gamma^2 D G_x^2 \delta^2 \left(\Delta - \frac{\delta}{3}\right).
\end{aligned} \tag{2.38}$$

The last term of Equation (2.38) is diffusion time.

In DWI, the parameter b-value is introduced. B-value is defined as

$$b = \gamma^2 G_x^2 \delta^2 \left(\Delta - \frac{\delta}{3}\right). \tag{2.39}$$

Equation (2.38) can be replaced using Equation (2.39):

$$\ln\left(\frac{M}{M_0}\right) = -bD. \tag{2.40}$$

Thus, we can state the net magnetization normalized by that which have not experienced phase shift M_0:

$$\frac{M}{M_0} = \exp\left(-bD\right). \tag{2.41}$$

Moreover, signal intensity S is determined proportional to the magnetization M, which provides

$$\frac{S}{S_0} = \exp\left(-bD\right). \tag{2.42}$$

Here, S and S_0 are the signal intensities of diffusing water molecules with and without phase shifts of their spins.

In an actual measurement, we usually obtain S_0 not applying the MPG in the sequence, that is, it is used to normalize S obtained by applying the MPG in the sequence. S/S_0 is referred to as the normalized signal intensity and represents how much the signal intensity decreases because of the diffusion phenomenon of water molecules. As is obvious in Equation (2.42), a larger diffusion of water molecules which leads larger D results in smaller S/S_0, and otherwise results in larger S/S_0. Moreover, as for b-value, Equation (2.42) represents that we also obtain smaller S/S_0 with larger b and larger S/S_0 with smaller b; we can describe that b-value is an important parameter which shows how much we are trying to emphasize the effects of the water molecule diffusion. It can be determined on the apparatus.

2.4 Neural magnetic field dependent fMRI (NMFD-fMRI)

In the previous section, we stated that DW-fMRI can be expected as a more direct method of fMRI compared with the conventional fMRI, which is based on the hemodynamic response, because it could be sensitive to influences of cell swellings caused by brain activation. In recent years, however, it has been expected that new fMRI methods will enable neural magnetic fields to be detected directly [23, 24, 25, 26, 27, 28, 29]. Although no fMRI experiment has been reported in which neural magnetic fields have been successfully detected, some researchers claim that such fields are observable with MRI scanners [24, 26, 28, 29]. If the new fMRI method can detect neural magnetic fields, it would provide the most direct measurement of fMRI methods. Researchers have been attempting to detect changes in phase or magnitude of the magnetization generated by subtle and transient alternations of static magnetic fields resulting from neural activities. However, these changes are weak and may be difficult to detect. In addition, phase cancellation induced by incoherent neuron orientation can influence results obtained using this method [23, 25].

In this section, we discuss the fMRI method based on direct detecting neural currents or neural magnetic fields. First of all, we describe recent researches about this fMRI. Second, we explain the principle of $T_{1\rho}$-weighted images obtained by means of spin-lock imaging sequence. It has potential to detect oscillating magnetic fields such as neural magnetic fields and is expected to be used for fMRI measurement.

2.4.1 Neural current fMRI

An fMRI method which is sensitive to neural magnetic fields is often referred to neural current imaging or current imaging. It is similar to the conventional BOLD-fMRI because both methods are fundamentally highly localized alternations in the main magnetic

field of the scanner, which depend on the geometry of the source (vasculature or neural bundle) and cause a phase shift and/or magnitude change [30]. The difference between BOLD and current fMRI is that the spacial and temporal resolutions, and the current fMRI is expected to have higher resolutions than BOLD-fMRI; the sources which cause alternations in the magnetic fields are different. Incidentally, if we consider the source of current fMRI, it actually is the neural magnetic field induced by neural currents which flow along dendrites of neural cells. In our research, therefore, we call this fMRI method directly targeting on magnetic fields generated by neural currents "neural magnetic field dependent (NMFD)-fMRI".

Singh et al. reported that they attempted to detect intrinsic neural magnetic fields with 1.5 T MRI in 1994 [47]. They carried out the experiment with a standard multishot SE imaging technique to detect phase changes induced by neural activities while human subjects experience auditory stimulus. In their study, the findings were negative; however, the approach was innovative. The first estimate of the minimal phase shift which can be detectable with the achievable signal-to-noise ratio (about 6 degrees) was shown in this study. It was also the first report that a current phantom was used to simulate neural activity.

In 1999, Bodurka et al. reported that they first used EPI time series data to observe the effects of injected current on MR phase and magnitude around the copper wire carrying current [23]. They demonstrated that phase shifts on the order of 0.8 ± 0.1 degrees (1.7 ± 0.3 nT magnetic field change) were detected and mapped.

Kamei et al. also published an effort at imaging neural currents in humans in 1999 [48]. In their study, they proposed the idea that the neural current effect is dependent in one direction on the gradient polarity, while susceptibility effect are not. They suggest that they successfully produced images of neural current distribution induced by neural activities; however, the reproducibility of these results remain to be demonstrated. After this work, this group also published another work on an RF pulsed-based method for detecting transient neural currents [49].

In 2002, Bodurka et al. [24] published a study about NMFD-fMRI method. They presented a straightforward but novel calculation for the expected field change in a voxel based on information from MEG, neuroanatomy and electrophysiology. Furthermore, in addition to GE-EPI sequence, they used SE-EPI sequence with regard to enhancement of high-temporal-frequency neural current effect and attenuation of less-high-frequency ($<$ 10 Hz) artificial phase shifts that can be caused by respiration or hemodynamic changes, and uncharacterized signal drift. Finally, they concluded that they could detect magnetic field changes as small as 200 pT and lasting for 40 ms in a phantom which contains wires by observing MR phase shifts. The sensitivity and flexibility of the technique was demonstrated by modulation of the temporal position and duration of the stimuli-evoked

transient magnetic field.

Konn et al. [25] provided a more complete theoretical and experimental validation of previous work. They examined the feasibility of NMFD-fMRI and predict MR phase and magnitude changes induced by neural currents based on the simulation; it modeled neural currents as extended current dipoles located in a homogeneous conducting sphere modeling the head. Simulation results suggested that a dipole of 4.5 nA could be detected with MRI and established that phase shifts represents the better sensitivity to MR signal changes than magnitude changes. Theoretical predictions were verified by experiments using a dipole phantom and GE-EPI imaging with a 3 T MRI scanner; they found that magnetic fields of 110 ± 50 pT could be detected.

Another study was published by Xiong et al. [50] in 2003. They claimed success in using MRI to directly map neural currents in humans. With visual stimulus, they demonstrated a 1 % magnitude changes primarily in mortar cortex that occurred within 150 ms of the onset of the finger movement. In the experiment, special paradigm were employed to achieve such a great temporal resolution.

Moreover, a NMFD-fMRI method using low-field (LF) or ultra-low-field (ULF) NMR [51, 52, 53] has been attracting attention due to its advantage that they have much lower main magnetic field (a few micro teslas) compared to conventional MRI, and therefore they can avoid possible problems of BOLD contamination and susceptibility artifacts. Kraus Jr. et al. [51] presented a physical basis and an experimental evidence for the resonant interaction between magnetic fields such as those produced by neural activities, with the spin population in ULF-NMRexperiments. Using current phantoms, they demonstrated that, in case of correlated zero-mean current distributions such that can be expected to result from neural activities, resonant interactions will provide larger changes in MR signals than those arising from MR phase shifts or MR magnitude changes observed in high-field MRI measurement.

Furthermore, Cassará et al. [52] investigated two methods of NMFD-fMRI using LF-NMR: resonant mechanism (RM) scheme, which was first described by Kraus Jr., and DC method. Nora et al. [53] mentioned two different techniques: a DC and an AC mechanism (AC mechanism is referred to RM scheme in Cassará's study), and carried out a phantom study to verify the application of these two measuring principles by means of LF-NMR. Through the experiment, they found the resolution limits of the two measuring procedures and concluded that it is necessary to improve the signal-to-noise ratio of the measurement system by at least a factor of 38 in order to directly detect typical human neural activities by means of LF-NMR. In addition, LF- or ULF-NMR has another advantage of compatibility with other brain function investigation tools like MEG, EEG and NIRS. Therefore, we can expect mulstimodal imaging acquisition techniques.

As we mentioned above, many researchers attempted to fMRI measurement by direct

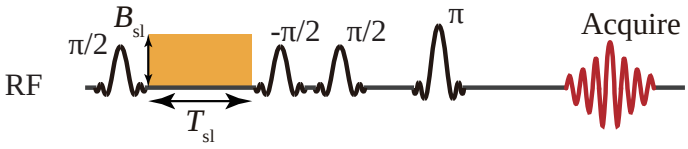

Figure 2.24: Spin-lock prepared spin echo pulse sequence. Spin-lock module consisting of two $\pi/2$ pulses with a spin-lock pulse between them proceeds a conventional spin-echo sequence. B_{sl} and T_{sl} are amplitude and duration time, respectively, of the spin-lock pulse.

detecting of neural currents; however they discussed a problem that we still do not know the precise manner in which neural currents add up in the brain and how it produce the magnetic field fluctuations that are detected at the surface by means of MEG. It is indeed possible that significant current polarity cancellation might take place at a spatial scale of MRI, however, some researchers insist that it should produce a set of greater magnetic fields at the "dipole" sources than those predicted by a simple model; it takes into consideration a 100 fT field at the surface of the scull and a radius cubed or radius squared falloff in magnetic fields from the source, which is several centimeters away [30].

Recently, a new fMRI approach challenging to detect neural magnetic fields was reported by Witzel et al. in 2008 [31]. They proposed that MR signal intensities decrease owing to interactions between a pulse in the spin-lock imaging sequence [54], which is one of sequences of MRI, and externally applied magnetic fields oscillating at its resonant frequency. This phenomenon is called stimulus-induced rotary saturation (SIRS) and has been demonstrated by means of simulations and phantom studies. Witzel et al. used a dipole phantom and detected 1 nT at 1.5 mm from the dipole. Furthermore, Halpern-Manners et al. reported fundamental studies on this fMRI approach [32]. They used a loop coil phantom and mapped its magnetic field to achieve the desired detection sensitivity. In this approach, magnetic field detection is not related to the observation of changes in the phase or magnitude of the magnetization. Therefore, many issues related to the cancellation of accumulated phase can be ignored. Moreover, it has an advantage of being able to detect oscillating magnetic fields such as α (8–13 Hz) and γ (25–150 Hz, including high-γ) waves [55] because there is no limitation on imaging oscillating magnetic fields with frequencies above –10 Hz [32, 51]. We describe the mechanism of this new NMFD-fMRI approach in Chapter 5.

2.4.2 Spin-lock imaging sequence

A spin-lock imaging is one of the MRI methods and it provides $T_{1\rho}$-weighted images. It was first described in 1955 [54], but has only recently been applied to biomedical MRI

[56]. $T_{1\rho}$-weighted imaging is expected to create an alternative contrast mechanism to conventional T_1- and T_2- weighted images. $T_{1\rho}$ is also called spin-lattice relaxation time in the rotating frame and is somewhat of a hybrid between T_1 and T_2. Actually, it always takes value between values of T_1 and T_2. Relaxation phenomenon of $T_{1\rho}$ in biological tissues has been extensively researched and they showed the sensitivity of $T_{1\rho}$- weighted imaging to physio-chemical processes (e.g., spin-spin interaction, chemical exchange) that occur at small interaction frequencies which is typically 0.1–100 kHz [57].

The spin-lock imaging sequence, which is shown in Figure 2.24, consists of a spin-lock module containing two $\pi/2$ pulses with a long-duration and low-power RF pulse, which is referred to as spin-lock pulse, between them and a conventional SE sequence. The first $\pi/2$ pulse is applied parallel to the x-axis in order to flip the magnetization into the transverse plane. The spin-lock pulse is applied as a second pulse and "lock" the magnetization in the transverse plane forcing the transverse magnetization to relax under the influences of itself [58]. If the spin-lock pulse is appropriately aligned with the transverse magnetization, the magnetization no longer relaxed according to T_2, but instead relaxes according to $T_{1\rho}$ [56]. The third pulse of the spin-lock module, a $\pi/2$ pulse, is applied in the inverse direction to the first $\pi/2$ pulse to restore the magnetization locked in the transverse plane.

The spin-lock pulse generates a small new magnetic field that is parallel to the magnetization flipped by the first $\pi/2$ pulse. If we definite the amplitude as B_{sl}, it is commonly referenced in terms of the precession frequency (γB_{sl}) [58]. In ordinary T_2 relaxation, the magnetization decays owing to dephased spin components. The presence of the spin-lock field prevents the dephasing and slows down the magnetization decay dramatically. This is why $T_{1\rho}$ is longer than T_2.

The signal obtained from the spin-lock imaging can be written as

$$S(T_{\mathrm{sl}}) \approx S_0 \exp\left(-\frac{T_{\mathrm{sl}}}{T_{1\rho}}\right), \tag{2.43}$$

where, S, S_0 and T_{sl} are an observed signal intensity, a signal intensity without a decay from $T_{1\rho}$ relaxation and a duration of the spin-lock pulse, respectively [58]. With the Equation (2.43), we can measure the $T_{1\rho}$ parameter by acquiring a series of $T_{1\rho}$-weighted images at varying T_{sl}. Moreover, using linear regression enables us to measure the $T_{1\rho}$ on a pixel-to-pixel basis and create a quantitative spatial map of $T_{1\rho}$ values.

There is another characteristic of $T_{1\rho}$ relaxation. T_1 and T_2 are pure properties of tissue and are virtually never affected by pulse sequence parameters [56]. Other than properties of tissues, both of them are affected by static magnetic field strength as described in Section 2.1, and therefore, have always fixed values in a specific MRI scanner. In contrast, $T_{1\rho}$ is unique because its value is determined by not only properties of tissues and static magnetic field strength but also features of the applied spin-lock pulse, B_{sl}. We can change

B_{sl} of the spin-lock pulse and it determine the precession frequency γB_{sl} of the spin-lock pulse, what we call spin-lock frequency. Therefore, we have to be aware that $T_{1\rho}$ depends on the amplitude of spin-lock pulse and this dependence is referred to as "$T_{1\rho}$ dispersion".

In addition, in Figure 2.24, we showed an example of the spin-lock imaging sequence which is based on the conventional SE sequence, however, it can be applied to most imaging sequences of MRI by adding the spin-lock module at the beginning of the pulse sequence of interest. For example, a 3D GE sequence with spin-lock module was developed recently and it provides 3D images of $\mathrm{T}_{1\rho}$-based contrast. Moreover, the combination of the spin-lock module and the fast imaging such as EPI of FSE is effective to obtain images with $\mathrm{T}_{1\rho}$-based contrast for reduction of imaging time.

Chapter 3

Appropriate MPG Parameters for DW-fMRI

DWI visualizes water self-diffusion in microscopic structures such as cellular tissues by using MRI; for measurements of living tissues, we need to consider restricted diffusion of water molecules. In the restricted diffusion, signal intensities of DWI vary intricately with MPG parameters.

In this chapter, we describe determination of appropriate MPG parameters for DW-fMRI based on simulations and phantom studies. To determine appropriate MPG parameters for fMRI measurement, we investigated influences of the MPG parameters on signal intensities by the Monte Carlo simulation of motions of water molecules diffusing in restricted structures whose sizes were comparable to those of neurons. The simulation results indicated that the signal intensities varied greatly depending on the MPG parameters and the size of the restricted structures. According to this simulation, we estimated values of MPG parameters that maximize differences in DWI signal intensities before and after cell swelling. The phantom studies also presented consistent results with simulations.

3.1 Previous studies

Recently, an increased number of studies have used DWI for fMRI [11, 15, 16, 17, 14]. Hereafter, we call this method diffusion weighted fMRI (DW-fMRI). Although several groups propose the mechanism of signal changes in DW-fMRI following brain activation, it is remain controversial. In some cases, an apparent diffusion coefficient (ADC), which indicates an apparent amplitude of water molecules diffusion considering the restricted diffusion, is referred to as signal changes originated from the brain activation because we use it as an index of water diffusion. It replaces the diffusion coefficient D in case of restricted diffusion and can be calculated by the DWI signal like D using Equation (2.42).

D. Le Bihan et al. reported that DWI could be used to visualize changes in tissue

microstructure, and changes in the water ADC during neural activation would probably reflect transient microstructual changes of the neurons and/or glial cells during activation [13]. Since the microstructual changes of neurons and/or glial cells would be directly linked to neural events, observing such effects would have a significant impact on the imaging of brain activation.

In 2001, their group reported that a transient decrease in ADC of water molecules was observed in the visual cortex of the human brain during a visual stimulus of a flickering black-and-white checkerboard [11]. Although the decrease in ADC was less than 1 %, it was significant and reproducible, and moreover, its time course followed closely that of the stimulus. They proposed that the origin of this change in the ADC depends on a transient swelling of cortical cells based on the characteristics of DWI and early studies on optical measurement; an early study of optical imaging techniques in tissue preparations and *in vivo* have confirmed that there are intrinsic regional changes in light transmittance during stimulation of synaptic pathways, which can attribute to cell swelling at the site of action potential initiation [18].

In 2006, they revealed that an early physiological marker of neural activation can be monitored to produce maps of cortical activation in the human brain with DWI [15]. In this report, they observed decreased water diffusion following brain activation by the fMRI experiments with visual stimulus. To investigate the observed changes in water diffusion, they modeled water diffusion of the brain cortex as a slow diffusion phase and a fast diffusion phase. Through this modeling and fMRI experiments, they found that the slowly diffusing water pool was expanding upon activation on the human visual cortex, while the fast diffusing pool was decreasing. Finally, they concluded that the transient water diffusion decrease observed upon activation primarily resulted from water phase transition from the fast phase to the slow phase.

Moreover, in 2009 they observed temporal dynamics of changes in water diffusion and BOLD responses in brain cortex [17]. They compared these temporal dynamics with changes of vascular hemoglobin content through near infrared spectroscopy. In this measurement, the rise time for the DWI signal was statistically significantly shorter than that of the BOLD signal and vascular hemoglobin content, which is assumed to be the fastest observable vascular signal. As a result, they suggested that the observed decrease in water diffusion reflects events that occur earlier than the vascular responses and it is originated from changes in the extravascular tissue. Another research also reported in 2009 by this group supported the faster response of fMRI measurement with DWI by extracting the raw signal in volume of interest [14].

Another interpretation for stimulus-induced signal changes in DW-fMRI is proposed by J. Kershaw et al. [16]. They analyzed data using a three-compartment signal model, with one compartment being purely vascular and the other two dominated by fast- and

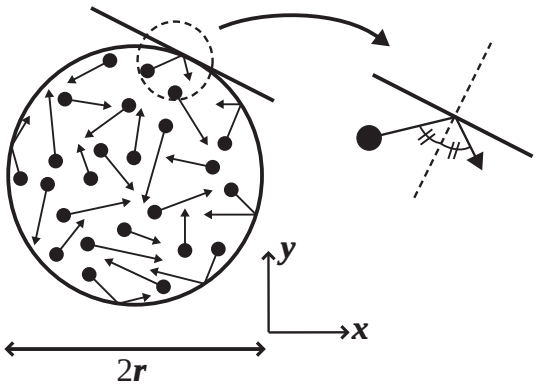

Figure 3.1: Simulation model with 2D circle structure. Radius of the circle is r. Water molecules diffuse in this restricted structure.

slow-diffusing molecules in the brain tissue. In their experiment the stimulus-induced signal changes can be decomposed into independent contributions from each of the three components. As a result, they suggested that these decomposed responses are interpreted in terms of the SE BOLD effect, and the signals produced by fast- and slow-diffusing molecules reflecting sensitivity to susceptibility changes in arteriole/venule- and capillary-sized vessels, respectively. Therefore, they concluded that signal changes in DW-fMRI was not originated from the diffusion phenomenon itself.

Tao et al. also investigated signal sources of ADC changes induced by neural activities in DW-fMRI [19]. In their fMRI measurement, isoflurane-anesthetized cats were used. They observed functional ADC changes and concluded that these changes arose from mostly vascular origin not from tissue origin. Furthermore, Song et al. reported that ADC changes during brain activation using DWI [20, 21, 22]. They investigated spatial and temporal characters of ADC changes of DW-fMRI, and suggested capillaries and upstream arterial contributions as sources of these functional ADC changes [20, 21]. In addition, they performed DW-fMRI sutudies in human subjects and demonstrated that the fucntional ADC changes were better localized compared to the BOLD contrast [22].

3.2 Simulation model

Neural cells in the brain mainly consist of cell bodies, dendrites and axons all of them swell with brain activation [18]. In the simulation, we focused on water diffusion around cell bodies whose diameters were approximately 5-100 μm [59], and modeled motion of water molecules around the cell bodies with those in a 2D circle, which has a diameter of the same value as the average distance of water molecules moving around the cell bodies.

The model used in the simulations is shown in Figure 3.1; it is a 2D circle with only

1 component. We set the diameters $2r$ of this circle as about 10–50 μm in order to compare these values with the diameters of the cell bodies. Hereafter, we refer to the diameter as "size of restriction". In the circle water molecules move according to the normal distribution simulating the Brownian motion unless they reach the edge of the circle. When a water molecule reaches the edge, its direction of motion is changed to inside the circle as if they are bounced at the edge; the exact direction is symmetric with the direction before the bounce making an axis of the line between the center of the circle and bounce point (Figure 3.1). Namely, the edge of the circle acts like a barrier to the water molecules. In addition, we ignore the permeation of water molecules because the total volume of interest should be much larger than those containing water molecules which permeate the barrier.

As described above, we employed quite simple model such as 2D circle with one component to simulate the restricted diffusion of water molecules around the neural cells; this is because we prioritize simplicity and investigation of the influence which barriers have on the motion of water molecules in the restricted diffusion over the reproducibility.

3.3 Simulation algorism

Simulations were conducted using Microsoft Visual C++. In the simulation, the obtained signal is represented as normalized signal intensities, which can be obtained by dividing the signal intensity with MPG by that without MPG, because it is usually used to emphasize influences of water diffusion in actual DWI measurement.

1. We used an circle with a diameter of $2r$ in the 2D space as a simulation model assuming water molecules can move only inside the circle. The center of the circle is located on the origin of the orthogonal coordinate system.

2. We arranged Z water molecules whose default positions were distributed uniformly in the circle.

3. We set Δt as a time step and renewed the position of each water molecule according to the Einstein–Smoluchowski equation. We renewed the positions of each water molecule according to a normal distribution with mean 0 and variance $2D\Delta t$ in each direction as follows:

$$\begin{aligned} \mathbf{p}_k(t+\Delta t) &= \mathbf{p}_k(t) + N[\mathbf{a}, \mathbf{C}] \\ k &= 1, 2, 3, \cdots, Z \\ \mathbf{a} &= \begin{pmatrix} 0 & 0 \end{pmatrix} \\ \mathbf{C} &= \begin{pmatrix} 2D\Delta t & 0 \\ 0 & 2D\Delta t \end{pmatrix} \end{aligned} \tag{3.1}$$

where $\mathbf{p}_k(t+\Delta t)$ is the position of each water molecule, and $N[\mathbf{m},\ \sigma^2]$ is a 2D random number following a normal distribution with mean $\mathbf{m}$ and variance σ^2. In addition, D is the diffusion coefficient of water molecules. When a water molecule reached the edge of the circle during the time step, we renewed its position so that the water molecule was reflected at the edge.

4. We renewed the phases of transverse magnetization in each water molecule, while MPG was applied according to the Stejskal-Tanner plus sequence shown in Figure 2.21. Thus, phase changes (θ) at each coordinate axis was calculated as follows:

$$\begin{aligned} \theta_{k,i}(t) &= \gamma g_i \int_t^{t+\Delta t} p_{k,i}(\tau) d\tau \\ k &= 1, 2, 3, \cdots, Z \\ i &= x, y \end{aligned} \tag{3.2}$$

where g_x and g_y are the amplitudes of MPG along the x- and y-axis, respectively. In addition, all phases were inverted when the π RF pulse was applied. The phase of each water molecule obtained at $t = TE$ was calculated as follows:

$$\begin{aligned} \theta_{k,i} &= -\sum_{j=0}^{n} \theta_{k,i}(j\Delta t) + \sum_{j=0}^{n} \theta_{k,i}(\Delta + j\Delta t) \\ k &= 1, 2, 3, \cdots, Z \\ i &= x, y \\ n &= \frac{\delta}{\Delta t} \end{aligned} \tag{3.3}$$

where the first MPG was applied at $t = 0$ and TE is an echo time.

5. We calculated the normalized signal intensity E of DWI from the phases of transverse magnetization as follows:

$$\begin{aligned} E &= \frac{S}{S_0} \\ &= \frac{1}{Z}\sqrt{\left(\sum_{k=1}^{Z}\cos\theta_k\right)^2 + \left(\sum_{k=1}^{Z}\sin\theta_k\right)^2} \\ \theta_k &= \theta_{k,x} + \theta_{k,y} \end{aligned} \tag{3.4}$$

where S is the signal intensity with MPG and S_0, that without MPG.

6. We obtained the final normalized signal intensities by repeating the same procedure R times and calculating the average of all normalized signal intensities.

3.4 Setting of simulations

As stated at the beginning of this section, we performed simulations of DWI to determine appropriate parameters for fMRI measurements with the DWI method. Considering the use of DWI as fMRI, differences of the normalized signal intensities between before and after the brain activation should be markers of neural activities; therefore, the differences should be maximized for better measurements of fMRI.

Equation (2.42) shows that the normalized signal intensity depends on the diffusion coefficient D and the b-value. In DW-fMRI, the apparent diffusion coefficient ADC replaces the diffusion coefficient D as stated in Chapter 2; and therefore, Equation (2.42) can be rewrite as;

$$\frac{S}{S_0} = \exp\left(-b \cdot ADC\right). \tag{3.5}$$

As a result, the normalized signal intensity depends on ADC and b, and we have to find out appropriate values for them to carry out DW-fMRI measurement. First of all, ADC is determined by an intrinsic diffusion coefficient D of water molecules and a size of regions where molecules can move (e.g., the diameter of the circle $2r$ in our simulation model). Thus, only the latter component should be considered because the intrinsic diffusion coefficient is fixed. Second, b is a complicated parameter and depends on three parameters, the amplitude g, the duration time δ and the separation time Δ of MPG as shown in Equation (2.39). Since all these three parameters can be decided on apparatuses, we have to take these three parameters into consideration.

Therefore, we introduced the other parameter 'q-value', which is usually used in q-space imaging (QSI) [60, 61], to use in DW-fMRI as a typical parameter of DWI with restricted diffusion. QSI can measure the microscopic construction of the object based on the DWI with restricted diffusion and indicates an impact of the restriction of the

construction on the normalized signal intensities; it is considered to be effective in DW-fMRI to choose the q-value as a parameter to investigate because water diffusion in living bodies is the restricted diffusion.

The q-value is expressed as

$$q = \frac{\gamma g \delta}{2\pi}. \tag{3.6}$$

As γ is fixed for the proton, the q-value depends on g and δ. Here, if we fix g, the q-value can be determined only by δ; and therefore it can be used as a DWI parameter instead of δ. Actually, it is preferable to use a large value for g so that we choose wide range of values for other parameters. Once we fix g, δ determines q, and δ and Δ determines b (Equation (2.39)). Consequently, b and q replaces δ and Δ. In this chapter, we focused on b-value and q-value to investigate appropriate values for DW-fMRI by the simulations because they are the parameters that can be determined on the apparatus, while the size of region and the diffusion coefficient are characteristics of a tissue of interest.

In the simulations, we first performed the case of free diffusion to confirm the validity of the simulation and that of restricted diffusion to understand the influences of parameters b-value and q-value on the normalized signal intensities of DWI. Furthermore, we investigated appropriate values for these two parameters by calculating differences of the normalized signal intensities between before and after the diameter of the circle $2r$ changed assuming the cell swellings. We obtained the differences ΔE by subtracting the normalized signal intensities after cell swelling from those before cell swelling and the normalized value $\Delta E/E$ by dividing the differences by the normalized signal intensities E befrore the cell swelling.

3.4.1 Free diffusion

There were nine parameters to determine in the simulation: the number of water molecules Z, the time step Δt, the repetition number of the simulation M, the diffusion coefficient D, the size of restriction (the diameter of the circle) $2r$, the duration time δ and separation time Δ of MPG, the amplitude of the x and y component, g_x and g_y, of MPG. The first three parameters, Z, Δ, and R, were necessary for the simulation algorism and the next two parameters, D and $2r$, determined ADC; D was fixed to the diffusion coefficient of water molecules. The last four parameters determined b-value and q-value. As for g_x and g_y, the sum of squares of them g can decide $g_x = g_y$ as $\sqrt{2}g$ because we assumed $g_x = g_y$.

Initially, to find out the values for Z and Δt which produce sufficient accuracy we obtained the simulation results while changing them. Through the simulation R was set to 10. Moreover, the simulation in case of the free diffusion requires the size of the region to be sufficiently large compared with the motion of water molecules; and therefore we defined $2r$ much larger than D. With these settings, we confirmed the accuracy of the

Table 3.1: Parameter sets for simulation with variation of Z.

Z	$\Delta t[\mu s]$	$D[mm^2/s]$	$g[mT/m]$	$\delta[ms]$	$\Delta[ms]$	R	$b[s/mm^2]$	$q[/mm]$
10^2								
10^3								
10^4	100	1.6×10^{-3}	400	2.936	11.111	10	1000	50
10^5								
10^6								

Table 3.2: Parameter sets for simulation with variation of Δt.

Z	$\Delta t[\mu s]$	$D[mm^2/s]$	$g[mT/m]$	$\delta[ms]$	$\Delta[ms]$	R	$b[s/mm^2]$	$q[/mm]$
	1							
10^6	10	1.6×10^{-3}	400	2.936	11.111	10	1000	50
	100							
	1000							

simulation by comparing the normalized signal intensity obtained from the simulation E and the theoretical equations (Equation (2.42)) E' $(=S/S_0)$. They provide an error P as follows;

$$P = \frac{E - E'}{E'} \times 100. \tag{3.7}$$

Z varies from 10^2 to 10^6 fixing Δt to 100 μs, while Δt varies from 1 to 1000 μ fixing Z 10^6. Among the rest of parameters, D took the value of 1.6×10^{-3} mm^2/s, which was the diffusion coefficient of purified water obtained by the DWI measurement. In addition, b and q took the values of 1000 s/mm^2 and 50 /mm, which were reasonable for the 7 T MRI apparatus, fixing g, δ and Δ to 400 mT/m, 2.936 ms and 11.111 ms, respectively. Table 3.1 and 3.2 show these parameters with variations of Z and Δt, respectively.

After the verification of the simulation and the determination of Z and ΔD, choosing values for those parameters which provided sufficient accuracy, we performed the similar verification of the simulation with variations of rest of parameters: D, b, q and g. Tables 3.3–3.6 show parameters for these verification in detail.

3.4.2 Restricted diffusion

The simulation of restricted diffusion also requires the nine parameters mentioned in case of the free diffusion above. Among the parameters, we chose the same values for the parameters defined for simulation algorism, Z, Δ, and R. D also took the same value as in the simulation of free diffusion because the object was also the diffusion of water molecules. Table 3.7 shows these parameters which were fixed through the simulation.

Table 3.3: Parameter sets for simulation with variation of D.

Z	$\Delta t[\mu s]$	$D[mm^2/s]$	$g[mT/m]$	$\delta[ms]$	$\Delta[ms]$	R	$b[s/mm^2]$	$q[/mm]$
10^6	100	0.5×10^{-3} 1.0×10^{-3} 1.5×10^{-3} 2.0×10^{-3} 2.5×10^{-3} 1.6×10^{-3}	400	2.936	11.111	10	1000	50

Table 3.4: Parameter sets for simulation with variation of b.

Z	$\Delta t[\mu s]$	$D[mm^2/s]$	$g[mT/m]$	$\delta[ms]$	$\Delta[ms]$	R	$b[s/mm^2]$	$q[/mm]$
10^6	100	1.6×10^{-3}	400	2.936	6.045	10	500	50
					11.111		1000	
					16.177		1500	
					21.243		2000	
					26.309		2500	
					31.375		3000	

Table 3.5: Parameter sets for simulation with variation of q.

Z	$\Delta t[\mu s]$	$D[mm^2/s]$	$g[mT/m]$	$\delta[ms]$	$\Delta[ms]$	R	$b[s/mm^2]$	$q[/mm]$
10^6	100	1.6×10^{-3}	400	0.587	253.499	10	1000	10
				1.174	63.717			20
				1.761	28.732			30
				2.349	16.614			40
				2.936	11.111			50
				3.523	8.211			60
				4.110	6.539			70
				4.697	5.524			80

Table 3.6: Parameter sets for simulation with variation of g.

Z	$\Delta t[\mu s]$	$D[mm^2/s]$	g[mT/m]	δ[ms]	Δ[ms]	R	$b[s/mm^2]$	q[/mm]
			100	11.743	14.046			
			200	5.871	12.089			
			300	3.914	11.437			
			400	2.936	11.110			
			500	2.349	10.915			
10^6	100	1.6×10^{-3}	600	1.957	10.785	10	1000	50
			700	1.678	10.691			
			800	1.468	10.621			
			900	1.305	10.567			
			1000	1.174	10.524			
			10000	0.117	10.171			

Table 3.7: Parameters in simulations of restricted diffusion. The value of Z, Δt, D, R is used through the simulations.

Z	$\Delta t[\mu s]$	$D[mm^2/s]$	M
10^6	100	1.6×10^{-3}	10

As for $2r$, we chose values of 10, 20, 30, 40 and 50 μm in order to compare them with the size of the cell bodies [59]. The rest of parameters, which we can determine on the apparatus and use to set b-value and q-value, were varied in order to investigate the influences of b-value and q-value on the normalized signal intensities of DWI. Although it is impracticable, g was fixed to 20000 mT/m to acquire results with wide range of b and q. We employed δ and Δ as shown in Table 3.8 to acquire b of 1000, 2000 and 3000 s/mm^2, and q of 0.1–300 /mm with each b, respectively.

3.4.3 Determination of appropriate values for parameters

After the verification of the simulation and the investigation of influences of the parameters b-value and q-value, which we determine on the apparatus, on the normalized signal intensities by the simulations of free and restricted diffusion, we also performed the other simulation of the restricted diffusion to determine appropriate values of the parameters b-value and q-value for DW-fMRI. In DW-fMRI, the marker of neural activities appear as the signal differences of DWI between activated and rest conditions. In the simulation for the appropriate values for the parameters, we assumed that changes in the diameter of the modeled circle reflected the changes in the neural cells of interest. Incidentally, the size of neural cell bodies in the human brain ranges approximately from 5 to 100 μm [59], and rates of swelling of neural cells related to neural activities or brain diseases remains

Table 3.8: Parameters used in simulations of restricted diffusion. $2r$ is assumed to be 10, 20, 30, 40, and 50 μm.

b[s/mm^2]	q[/mm]	g[mT/m]	δ[ms]	Δ[ms]
	0.1		1.17×10^{-4}	2.53×10^{6}
1000	|	20000	|	|
	300		0.352	0.399
	0.1		1.17×10^{-4}	5.07×10^{6}
2000	|	20000	|	|
	300		0.352	0.680
	0.1		1.17×10^{-4}	7.60×10^{6}
3000	|	20000	|	|
	300		0.352	0.962

unrevealed. Considering these facts, we therefore postulated that the region around neural cells with the size of restriction was 10 μm, that is, the diameter of the modeled circle $2r$ was 10 μm. By changing the diameter to 10.1, 10.5 and 11.0 μm, which indicated that the swelling rate of the region were 1, 5 and 10% in diameter, respectively, we obtained the differences of the normalized signal intensities between before and after the changes of $2r$; hereafter we referred the differences as the normalized signal differences.

We used the same values as those of Subsection 3.4.2 as shown in Table 3.7 for the parameters of the simulation itself: Z, Δt, D and R. In this subsection, we assumed two types of MR scanner for the DW-fMRI through the simulation: 7 T and 3 T MR scanners. Since the maximum amplitude of the MPG was approximately 400 and $25\sqrt{2}$ mT/m for 7 T and 3 T MR scanners, respectively, we set g to 400 and $25\sqrt{2}$ mT/m. Moreover, b took 1000, 2000 and 3000 s/mm^2 as used in Subsection 3.4.2, and q took the values with these g and b as follows: while g was 400 mT/m, q was 10–86 /mm with b of 1000 s/mm^2, 10–108 /mm with b of 2000 s/mm^2 and 10–124 /mm with b of 3000 s/mm^2, and while g was $25\sqrt{2}$ mT/m, q was 10–38 /mm with b of 1000 s/mm^2, 10–48 /mm with b of 2000 s/mm^2 and 10–55 with b of 3000 s/mm^2. Incidentally, the minimum q was 10 /mm in the every condition because too small q causes too short δ and too long Δ, which was obvious from the Equations (2.39) and (3.6). As Δ has a limitation to be shorter than TE (approximately 95 ms in usual) in DWI, the long Δ prolong TE and it degrades SNR of obtained images. In addition, the imaging time will also become longer; it is not practicable for DW-fMRI. We therefore set the minimum value of q to 10 /mm to make Δ shorter than several hundreds ms at most. Furthermore, q has also a limitation because δ must be shorter than Δ. We calculated the maximum value which satisfies that condition from Equations (2.39) and (3.6). Tables 3.9 and 3.10 show these parameter sets with g of 400 and $25\sqrt{2}$ mT/m, respectively.

Table 3.9: Parameter sets used in simulations for determination of appropriate values of b and q, when g=400 mT/m. Diameter of the simulation model is assumed to chage from 10.0 μm to 10.1, 10.5, and 11.0 μm.

b[s/mm^2]	q[/mm]	g[mT/m]	δ[ms]	Δ[ms]
	10		0.59	253.50
1000	|	400	|	|
	86		5.05	5.11
	10		0.59	506.80
2000	|	400	|	|
	108		6.34	6.46
	10		0.59	760.10
3000	|	400	|	|
	124		7.28	7.37

Table 3.10: Parameter sets used in simulations for determination of appropriate values of b and q, when g=$25\sqrt{2}$ mT/m. Diameter of the simulation model is assumed to chage from 10.0 μm to 10.1, 10.5, and 11.0 μm.

b[s/mm^2]	q[/mm]	g[mT/m]	δ[ms]	Δ[ms]
	10		6.64	255.52
1000	|	$25\sqrt{2}$	|	|
	38		25.24	25.96
	10		6.64	508.82
2000	|	$25\sqrt{2}$	|	|
	48		31.88	32.63
	10		6.64	762.12
3000	|	$25\sqrt{2}$	|	|
	55		36.53	37.31

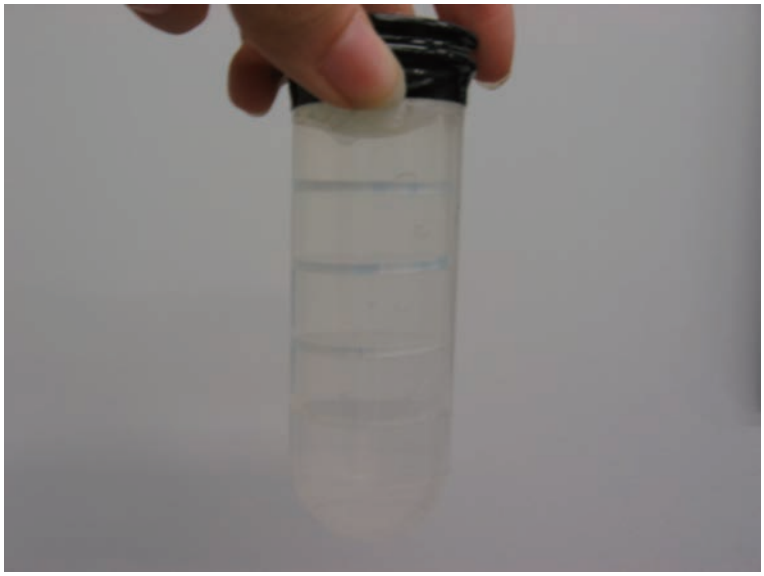

Figure 3.2: Phantom consisted of a plastic tube, purified water and four glass plates with capillaries. The plastic tube and the capillaries were filled with purified water.

3.5 Setting of phantom study

Phantom study supported the validation of the simulation in case of restricted diffusion and the investigation of the influences of the parameters b-value and q-value. We prepared the phantom, which has cylindrical regions with diameters and a length of 6–50 μm and 2 mm, respectively, inside it, to carry out the MR imaging of water molecules whose motions are restricted. We actually observed the normalized signal intensities as MR images from water molecules moving inside the cylindrical regions.

3.5.1 Phantom

The phantom consisted of a plastic tube, purified water and two glass plates with capillaries (Hamamatsu photonics K.K., Hamamatsu, Japan). We showed the phantom in Figure 3.2. The glass plates, which we called capillary plates, had a countless number of capillaries with the same diameter in each plate and all those thickness was 2 mm. They are fixed inside the plastic tube with acrylic pipes whose diameter was a size smaller than that of the plastic tube. The capillaries were arranged perpendicular to the plates and uniformly distributed on the plate; the capillaries with diameters of 10 and 20 μm, respectively. Figures 3.3 and 3.4 show the four capillary plates located in a beaker and images of the capillary plates with the diameter of 10 and 20 μm, magnified with an optical microscope by 20 and 50 times, respectively. Ahead of putting the capillary plates inside the plastic tube, we washed the capillary plates with an ultrasonic cleaning equipment

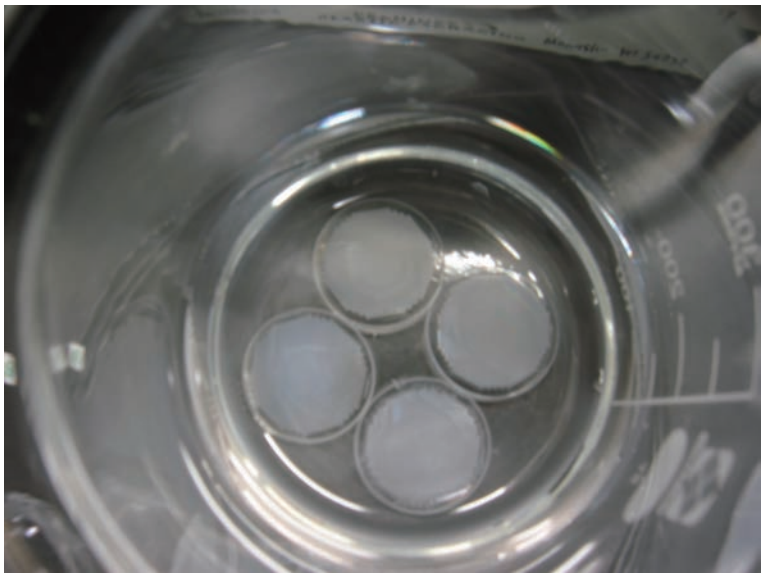

Figure 3.3: Capillary plates used in the imaging experiments.

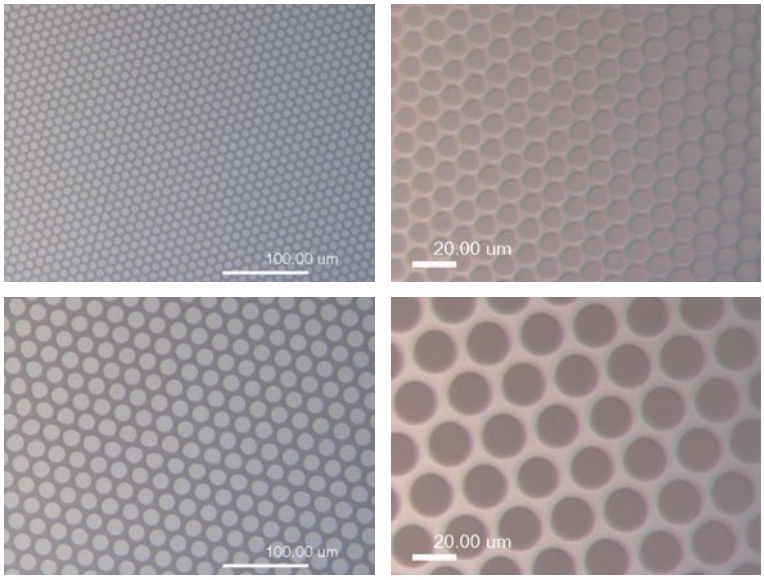

Figure 3.4: Images of capillary plates which were magnified with optical microscope. The upper and lower column shows images of the capillary plates with 10 and 20 μm capillaries, respectively, and the left and right low show images with the magnification of 20 and 50 times, respectively.

Figure 3.5: Ultra sonic cleaning equipment.

(Yamato Scientific Co., Ltd., Tokyo, Japan) shown in Figure 3.5. An oscillating frequency was 42 kHz and we set the temperature of water for washing to 55 degrees. After washing the capillary plates for 1 hour, we put them inside the plastic tube not to mix air bubbles there.

Imaging condition

The imaging equipment was 7 T MR imaging scanner, BioSpin (Bruker), which is originally used for animal experiments. Figure 3.6 shows the MR imaging scanner; it used a quadrature coil whose diameter was 72 mm as a RF coil. We placed the above-mentioned phantom in the quadrature coil.

We chose multi-shot SE-EPI sequence, which is shown in Figure 2.21 for DWI measurements of the phantom. The number of the shot was 16. We set parameters for the MPG in the same way as the simulation of restricted diffusion stated in Subsection 3.4.2; fixing g and choosing b and q determined the required δ and Δ. As for g, we fixed g_x and g_y to $200\sqrt{2}$ mT/m, which was the maximum value set on the apparatus, producing g of 400 mT/m. Here, we defined the plane of capillary plate as x-y plane and the axis which is parallel to the capillaries as z axis. With fixed g of 400 mT/m, we set b to 1000, 2000 and 3000 s/mm^2 similar to the simulation of restricted diffusion; and therefore, we set q to 20–60 /mm with b of 1000 s/mm^2, 25–80 /mm with b of 2000 s/mm^2, and 30–95 /mm with b of 3000 s/mm^2, considering the limitation of the apparatus. Table 3.11–Table 3.13 show parameter sets of MPG with b of 1000, 2000 and 3000 s/mm^2, respectively.

Moreover, we set parameters for imaging as follows: field of view (FOV) of 40 mm $\times$

Figure 3.6: MR scanner used for DWI measurement.

Table 3.11: Parameter set of imaging experiments with b of 1000 s/mm^2

b[s/mm^2]	q[/mm]	g[mT/m]	δ[ms]	Δ[ms]
	20		1.18	63.64
	25		1.47	41.01
	30		1.76	28.71
	35		2.05	21.36
1000	40	400	2.35	16.61
	45		2.64	13.38
	50		2.94	11.11
	55		3.23	9.45
	60		3.52	8.21

Table 3.12: Parameter set of imaging experiments with b of 2000 s/mm^2

b[s/mm^2]	q[/mm]	g[mT/m]	δ[ms]	Δ[ms]
2000	25	400	1.47	81.55
	30		1.76	56.88
	35		2.05	42.02
	40		2.35	32.45
	45		2.64	25.90
	50		2.94	21.24
	55		3.23	17.82
	60		3.52	15.25
	65		3.82	13.26
	70		4.11	11.71
	75		4.40	10.47
	80		4.70	9.48

Table 3.13: Parameter set of imaging experiments with b of 3000 s/mm^2

b[s/mm^2]	q[/mm]	g[mT/m]	δ[ms]	Δ[ms]
3000	30	400	1.76	85.02
	35		2.05	62.71
	40		2.35	48.28
	45		2.64	38.41
	50		2.94	31.37
	55		3.23	26.20
	60		3.52	22.28
	65		3.82	19.26
	70		4.11	16.88
	75		4.40	14.98
	80		4.70	13.44
	85		5.00	12.18
	90		5.28	11.14
	95		5.58	10.28

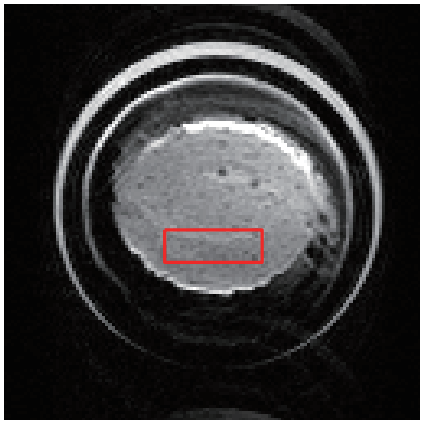

Figure 3.7: Pixels used for calculation of normalized signal images. We divided the image data with MPG by those without MPG. We acquired the average and the standard deviation of pixels surrounded by a red line.

40mm, matrix size of 128 × 128, slice thickness of 1 mm; we also set TE to 80 ms with b of 1000 s/mm^2 and 100 ms with b of 2000 and 3000 s/mm^2. In every imaging scan, we obtained two slices, each of which contained the capillary plate at once with these parameter sets. In addition to these imaging experiments, we acquired one more image set of two capillary plates not applying MPG to obtain the normalized signal intensities.

Imaging processing

We used MATLAB for image processing. The obtained MR images were stored in dicom format with slice by slice. We read the dicom images into the MATLAB as image data of 128 × 128 pixels and each pixel has a MR signal intensity which were acquired at the position of the pixel. To calculate normalized signal intensities, we divided all the image data with MPG by that without MPG. We therefore chose pixels of the divided image data surrounded by a red line shown in Figure 3.7 to avoid contaminations of noise and artifacts, and acquired the average and the standard deviation of those pixels as the normalized signal intensity. The same processing was applied to all the parameter sets.

3.6 Results

3.6.1 Simulations for free diffusion

Tables 3.14 – 3.19 show the results of simulations for free diffusion: normalized signal intensities E and their errors P for the calculated normalized signal intensities obtained from the theoretical equation (Equation (2.42)) E' as expressed in Equation (3.7) with the variations of Z, Δt, D, b, q and g, respectively.

Table 3.14: Normalized signal intensities and errors for simulations with variation of Z.

Z	E'	E	P[%]
10^2	0.202	0.226	11.797 ± 25.360
10^3	0.202	0.205	1.666 ± 12.175
10^4	0.202	0.202	0.169 ± 3.232
10^5	0.202	0.203	0.535 ± 0.910
10^6	0.202	0.202	-0.065 ± 0.310

Table 3.15: Normalized signal intensities and errors for simulations with variation of Δt.

$\Delta t[\mu s]$	E'	E	P[%]
1	0.202	0.202	-0.118 ± 0.171
10	0.202	0.202	0.095 ± 0.495
100	0.202	0.202	0.144 ± 0.284
1000	0.202	0.204	0.959 ± 0.248

Table 3.16: Normalized signal intensities and errors for simulations with variation of D.

D[mm^2/s]	E'	E	P[%]
0.5×10^{-3}	0.607	0.607	0.014 ± 0.076
1.0×10^{-3}	0.368	0.368	-0.007 ± 0.137
1.5×10^{-3}	0.223	0.223	-0.087 ± 0.273
2.0×10^{-3}	0.135	0.136	0.153 ± 0.368
2.5×10^{-3}	0.082	0.082	-0.010 ± 0.880
1.6×10^{-3}	0.202	0.202	-0.122 ± 0.386

Table 3.17: Normalized signal intensities and errors for simulations with variation of b (Δ).

b[s/mm^2]	δ[ms]	Δ[ms]	E'	E	P[%]
500	2.936	6.045	0.449	0.449	0.012 ± 0.117
1000	2.936	11.111	0.202	0.200	0.080 ± 0.264
1500	2.936	16.177	0.091	0.091	0.319 ± 0.795
2000	2.936	21.243	0.041	0.041	-0.063 ± 1.595
2500	2.936	26.309	0.018	0.018	-0.458 ± 3.349
3000	2.936	31.375	0.008	0.008	-2.046 ± 10.177

Table 3.18: Normalized signal intensities and errors for simulations with variation of q (δ, Δ).

q[/mm]	δ[ms]	Δ[ms]	E'	E	P[%]
10	0.587	253.499	0.202	0.202	0.017 ± 0.313
20	1.174	63.717	0.202	0.202	-0.034 ± 0.287
30	1.761	28.732	0.202	0.202	-0.124 ± 0.151
40	2.349	16.614	0.202	0.202	0.007 ± 0.339
50	2.936	11.110	0.202	0.202	0.071 ± 0.450
60	3.523	8.210	0.202	0.202	0.106 ± 0.314
70	4.110	6.539	0.202	0.202	0.034 ± 0.309
80	4.697	5.524	0.202	0.202	-0.098 ± 0.379

Table 3.19: Normalized signal intensities and errors for simulations with variation of g.

g[mT/m]	E'	E	P[%]
100	0.202	0.202	-0.162 ± 0.266
200	0.202	0.202	-0.145 ± 0.466
300	0.202	0.202	-0.081 ± 0.270
400	0.202	0.202	-0.048 ± 0.428
500	0.202	0.202	0.047 ± 0.421
600	0.202	0.202	-0.002 ± 0.337
700	0.202	0.202	0.059 ± 0.152
800	0.202	0.202	0.084 ± 0.325
900	0.202	0.202	-0.021 ± 0.222
1000	0.202	0.202	0.022 ± 0.404
10000	0.202	0.202	0.268 ± 0.409

First of all, the parameters which determine accuracy of simulations, Z and Δt, had great impacts on errors. Table 3.14 demonstrates that a large value of Z enhances simulation accuracy. This is probably because the distribution of phase change of each molecule was biased and therefore, the normalized signal intensities did not followed the theoretical equation in case of a small value of Z. As for Δt, Table 3.15 indicates that a small value of Δt enhances simulation accuracy. Too large value of Δt is considered to cause degradation in accuracy because it decreases the number of renewal of the molecules' positions and phases. Therefore, a large value of Z and a small value of Δt are preferable to obtain high accuracy. Here, Table 3.14 shows the error of -0.06% for Z of 10^6, which presents sufficient accuracy. Table 3.15 also shows that we obtain sufficient accuracy with a maximum of 0.15% error if we chose Δt of 1, 10 or 100 μs; Δt of 100 μs is preferable considering the calculation time. Consequently, as stated in Section 3.4, we chose Z of 10^6 and Δt of 100 μs as parameters determining the simulation accuracy through our simulations.

Secondly, we showed the simulation results of free diffusion with the determined Z and Δt in Tables 3.16 – 3.19. They indicate that we can obtain sufficient accuracy with almost all the parameter sets; the errors between the simulation results and theoretical values are smaller than 1%. These results suggest that our simulation with Z of 10^6 and Δt of 100 μs guarantees the sufficient accuracy with possible parameters of DWI in case of free diffusion.

In addition, we fixed R for 10 all through the simulations to avoid increases of simulation time although we can expect higher accuracy with a larger value of R.

3.6.2 Simulations for restricted diffusion

Figure 3.8 shows that the simulation results in case of restricted diffusion with the variation of q-value. Figure 3.8 (a), (b) and (c) show the normalized signal intensities E at each diameter of the circle with b of 1000, 2000 and 3000 s/mm^2, respectively. From these results, we confirmed that normalized signal intensities decrease with the increase of the q-value under all conditions. If the b and the g are fixed, a shorter δ and a longer Δ are obtained, and a lower q is also obtained according to Equations (2.39) and (3.6). When the separation time is long, the elapsed time between a pair of MPG is also long and water molecules move long during that time. Thus, with a small q-value, the time during which water molecules collide against the edge of the circle increases, and the normalized signal intensities are strongly affected by the restricted diffusion of water molecules. Consequently, the normalized signal intensities with the smallest q-value decrease minimally and are approximately equal to 1.0. As the q-value increases, the normalized signal intensities largely decrease and approach to those obtained in case of free diffusion.

In addition, Figures 3.8 (a), (b) and (c) indicate that normalized signal intensities begin to decrease from 1.0, approaching that obtained in case of free diffusion at different

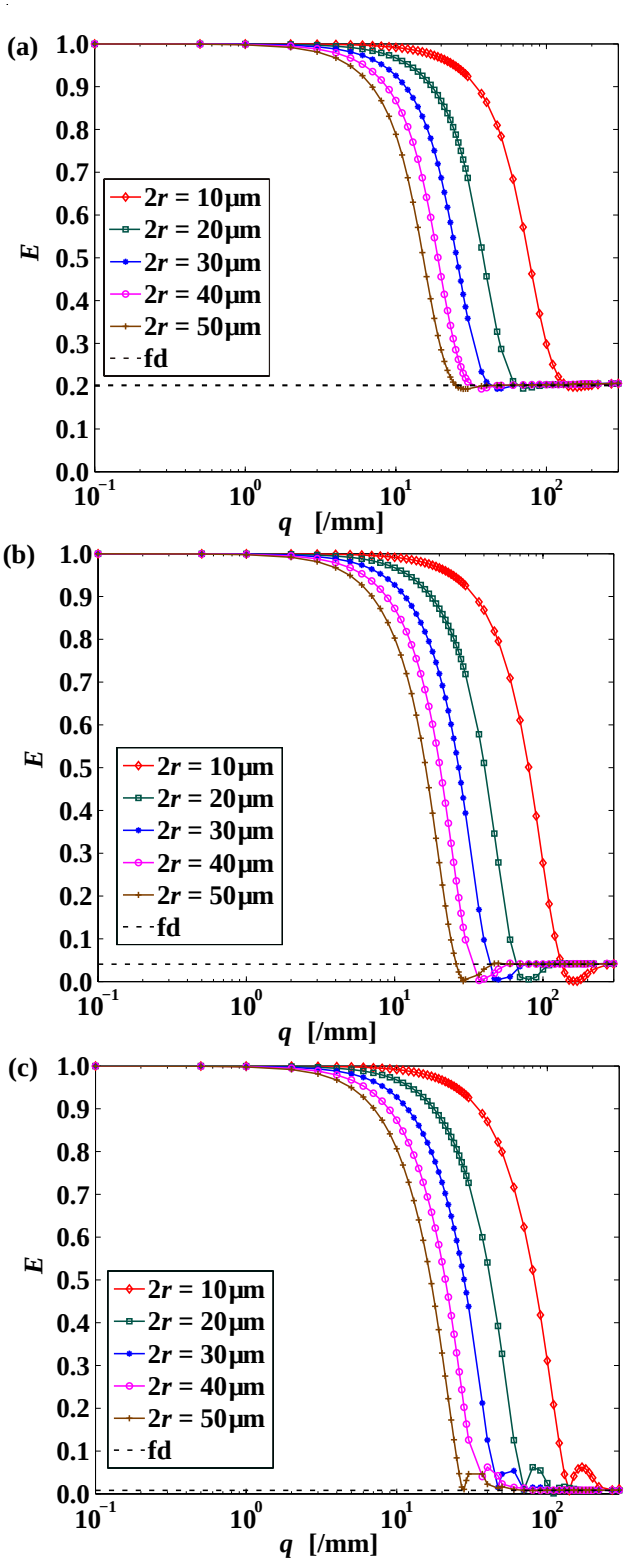

Figure 3.8: Normalized signal intensities, as function of various q, for 3 different b of 1000 s/mm^2 (a), 2000 s/mm^2 (b) and 3000 s/mm^2 (c). Dotted lines indicate normalized signal intensities in free diffusion.

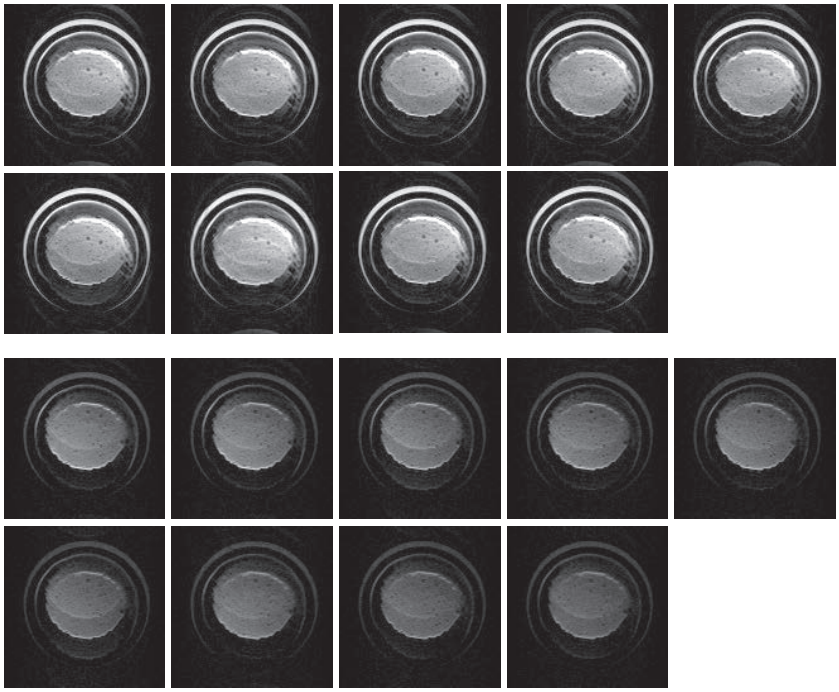

Figure 3.9: MR images of slices including capillary plate with capillaries of 10 μm in diameter while b was fixed to 1000 s/mm^2. The first half of images are MR images without MPG and the others are those with MPG applied along both x- and y- axis. The q was set to 20, 25, 30, 35, 40, 45, 50, 55 and 60 /mm in order from left upper side.

q-value and various diameters. The normalized signal intensities begin to decrease from 1.0 at smaller q-value with larger diameters. Similarly, the normalized signal intensities also approach those obtained in case of free diffusion at smaller q-value with larger diameters. This is because the larger diameters increase the size of the restricted structure in which water molecules can diffuse, and therefore, normalized signal intensities are less affected by the restriction. Moreover, we also found that normalized signal intensities decrease with an increase of b-value, which is obvious from Equation (2.42). Finally, we investigated the relationship between the q-value and normalized signal intensities of DWI by observing the influences of the duration and the separation time on normalized signal intensities obtained in case of restricted diffusion. Our results suggest that the q-value has a great impact on DWI measurement where the restricted diffusion is dominant and that the q-value should be carefully set similar to the b-value.

3.6.3 Comparison between simulation and phantom study

Figures 3.9 – 3.14 show MR images of the capillary phantom obtained by the DWI measurements. Figures 3.9 – 3.11 display the images of slices including the capillary plate with capillaries whose diameter is 10 μm while b is fixed to 1000, 2000 and 3000 s/mm^2.

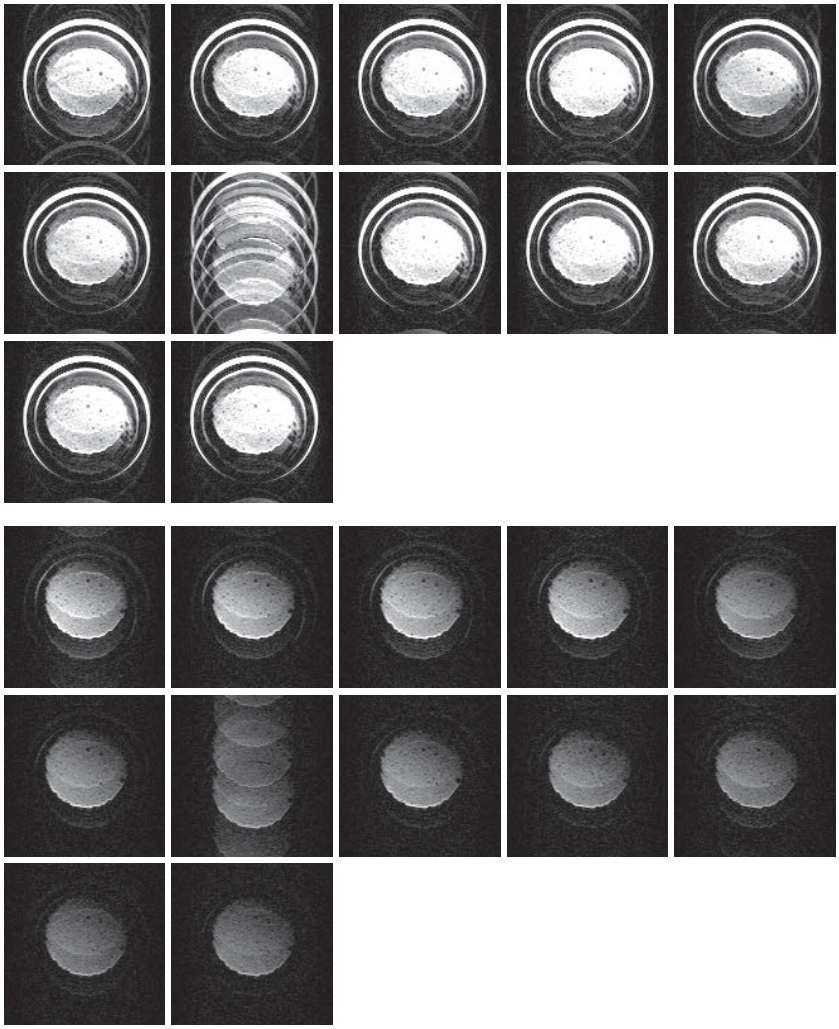

Figure 3.10: MR images of slices including capillary plate with capillaries of 10 μm in diameter while b was fixed to 2000 s/mm^2. The first half of images are MR images without MPG and the others are those with MPG applied along both x- and y- axis. The q was set to 25, 30, 35, 40, 45, 50, 55, 60, 65, 70, 75 and 80 /mm in order from left upper side.

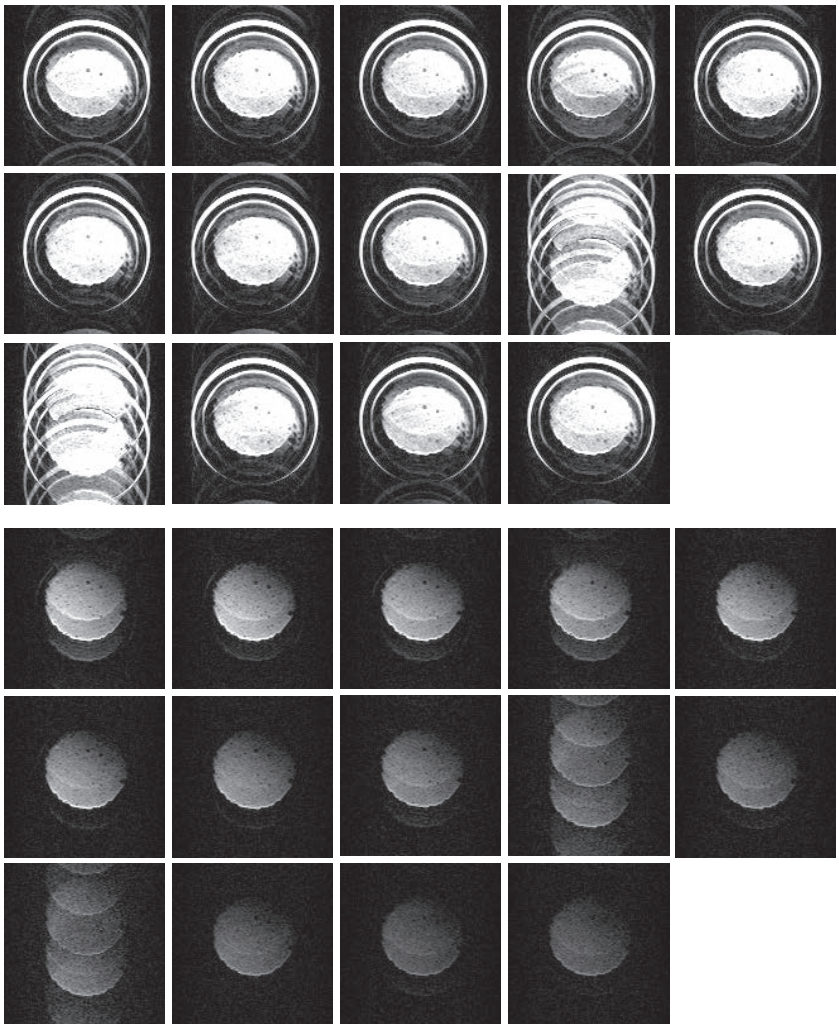

Figure 3.11: MR images of slices including capillary plate with capillaries of 10 μm in diameter while b was fixed to 3000 s/mm^2. The first half of images are MR images without MPG and the others are those with MPG applied along both x- and y- axis. The q was set to 30, 35, 40, 45, 50, 55, 60, 65, 70, 75, 80, 85, 90 and 95 /mm in order from left upper side.

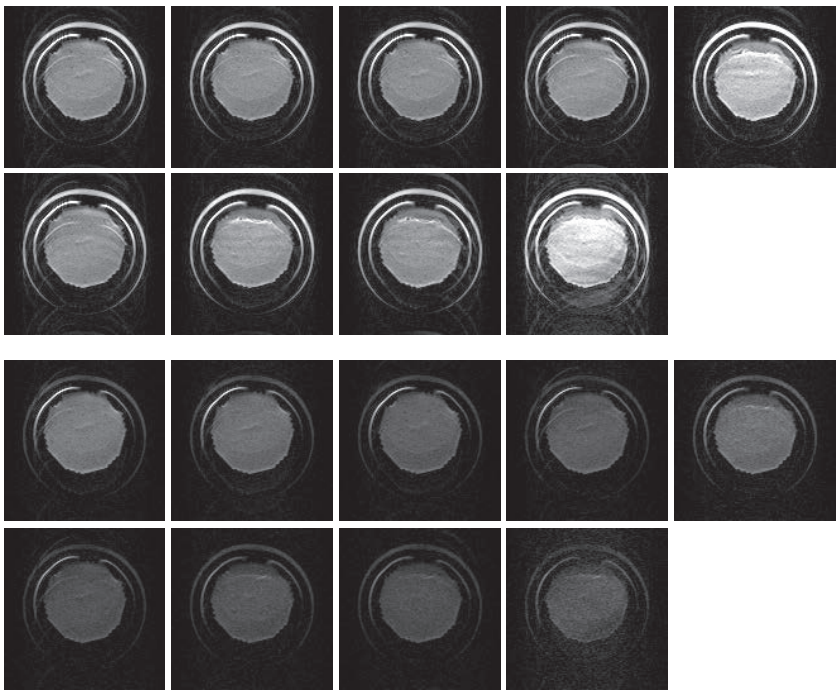

Figure 3.12: MR images of slices including capillary plate with capillaries of 20 μm in diameter while b was fixed to 1000 s/mm^2. The first half of images are MR images without MPG and the others are those with MPG applied along both x- and y- axis. The q was set to 20, 25, 30, 35, 40, 45, 50, 55 and 60 /mm in order from left upper side.

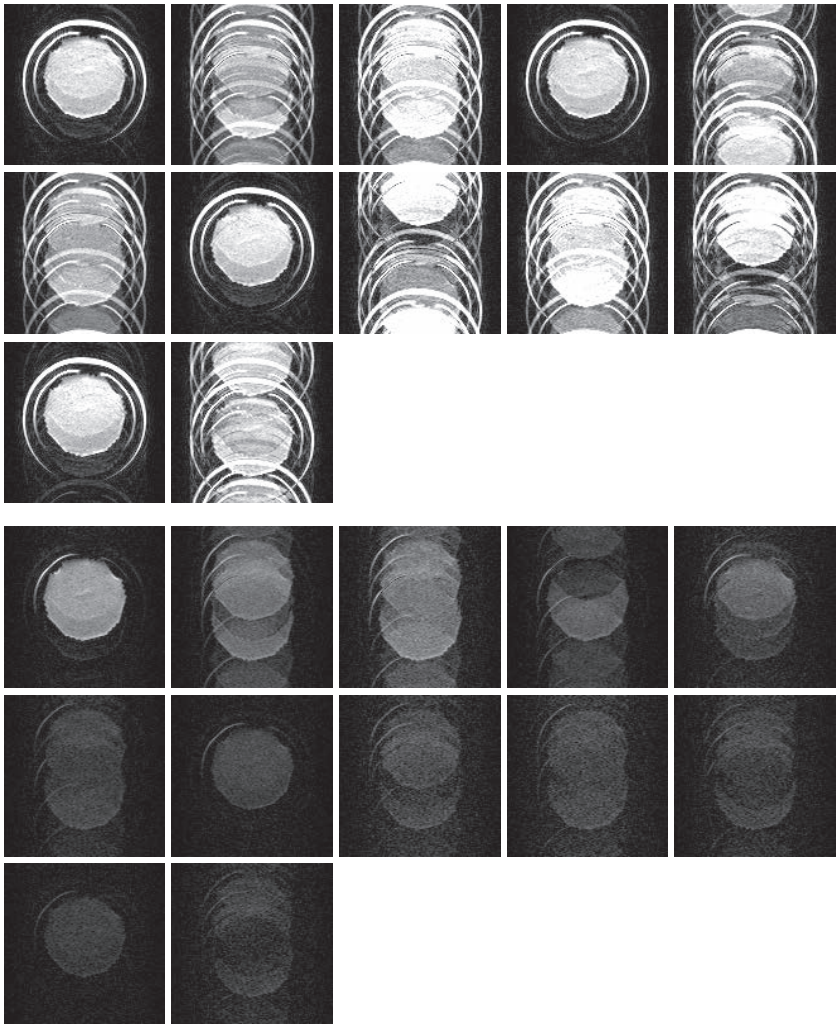

Figure 3.13: MR images of slices including capillary plate with capillaries of 20 μm in diameter while b was fixed to 2000 s/mm^2. The first half of images are MR images without MPG and the others are those with MPG applied along both x- and y- axis. The q was set to 25, 30, 35, 40, 45, 50, 55, 60, 65, 70, 75 and 80 /mm in order from left upper side.

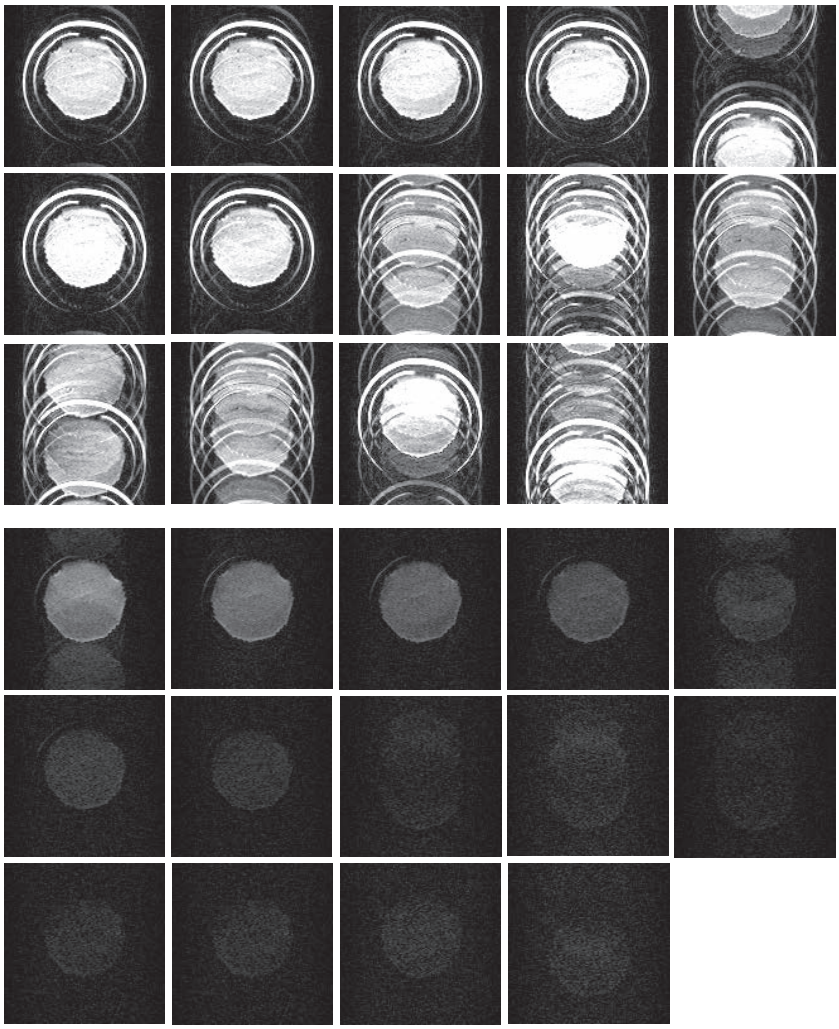

Figure 3.14: MR images of slices including capillary plate with capillaries of 20 μm in diameter while b was fixed to 3000 s/mm^2. The first half of images are MR images without MPG and the others are those with MPG applied along both x- and y- axis. The q was set to 30, 35, 40, 45, 50, 55, 60, 65, 70, 75, 80, 85, 90 and 95 /mm in order from left upper side.

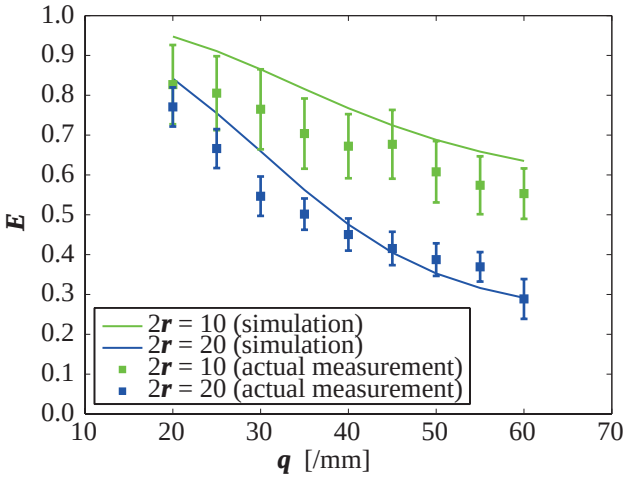

Figure 3.15: Plots of normalized signal intensity E of simulations and DWI measurement of phantom. We chose the variation of q and fixed b of 1000 s/mm^2.

The first half of images are MR images without MPG, which we call b_0 images, and the others are those with MPG applied along both x- and y- axis. Figures 3.12 – 3.14 also display the images of slices including the capillary plate with capillaries whose diameter is 20 μm while b is fixed to 1000, 2000 and 3000 s/mm^2; the first half of images are MR images without MPG and the others are those with MPG. We can observe great effect of noises or artifacts in Figures 3.10, 3.11, 3.13 and 3.14 than Figures 3.9 and 3.12. The reason may be that the large b-value largely decreases the signal intensities of MR images with MPG as noted in Equation (2.42), and therefore, SNR deteriorates greatly. Thus, we decided to investigate the MR images with b of 1000 s/mm^2 considering the difficulty of processing MR images with b of 2000 and 3000 s/mm^2 owing to great effect of noises and artifacts.

Figure 3.15 shows the comparison between the normalized signal intensities of the simulation and the DWI measurement; the solid lines and the dots with error bars of the standard deviation (SD) indicate the normalized signal intensities calculated from the simulation and the averaged normalized signal intensities of the ROI obtained from DWI measurement, respectively. In the simulation for the comparison with the DWI measurement, the same parameters used in the DWI measurement was used. Both of the results presented the same tendency with $2r$ of 10 and 20 μm. Although the largest difference between the normalized signal intensities of the simulation and the DWI measurement was -11.773 $\pm$ 2.079% with $2r$ of 10 μm, it was less than 1SD of the result of DWI measurement. In the case with $2r$ of 20 μm, the largest difference was -2.774 $\pm$ 10.989%, which was less than 2SD.

3.6.4 Determination of appropriate parameters

We investigated the parameters, especially q-value and b-value, that enhance normalized signal differences in DWI measurements when the size of restriction changes. The simulation produced the normalized signal differences assuming that the diameter of the cell body increased from 10.0 to 10.1, 10.5, and 11.0 μm due to cell swelling. Figures 3.17 (a), (b) and (c) show the normalized signal differences with the variation of q, while b is set to 1000, 2000 and 3000 s/mm^2, respectively. We chose 400 mT/m for g to assume MR scanners with B_0 of 7 T. Figures 3.16 (a), (b) and (c) also show the normalized signal differences with g of $25\sqrt{2}$ assuming MR scanners with B_0 of 3 T; the b was also set to 1000, 2000 and 3000 s/mm^2.

MPG parameters that are appropriate for DW-fMRI should cause the large normalized signal differences between before and after swelling. As for results with g of 400 mT/m, Figure 3.17 (a) demonstrates that q of 80 /mm, which is the largest value, maximizes the differences with every swelling ratio. Figure 3.17 (b) also shows that the largest q-value provides the largest differences in every swelling ratio. We, however, observed the largest differences with q of approximately 80 /mm with b of 3000 s/mm^2 in Figure 3.17 (c), which indicates that the largest q-value does not always maximize the differences. Moreover, we found that the largest q-value provided the largest differences with every swelling ratio in Figures 3.16 (a), (b) and (c), when we set g to $25\sqrt{2}$; this may be because the small value of g limits the range of the q-value.

In addition to the q-value, we should consider an appropriate b-value. As mentioned above, while g was fixed, we had the similar tendency of the q-value dependence on normalized signal differences. The results showed that the large b-value caused large differences.

3.7 Discussion

First of all, the simulations for free diffusion showed that the parameters Z of 10^6 and Δt of 100 μs were suitable to simulate the motions of water molecules. It also showed that we could obtain sufficient accuracy using these parameters in the simulation by comparing the simulation results with the normalized signal intensities calculated with the theoretical equation.

Second, the simulations for restricted diffusion indicated that the normalized signal intensities of DWI significantly depended on q-value as well as b-value. While the b-value is well known as the important parameter for DWI, the q-value has not been focused on. However, as is evident from the results, the q-value has a large influence on the signal intensities in case of restricted diffusion; the dotted lines in Figure 3.8 showed the results of free diffusion and they did not depend on the q-value. The q-value is defined as Equation

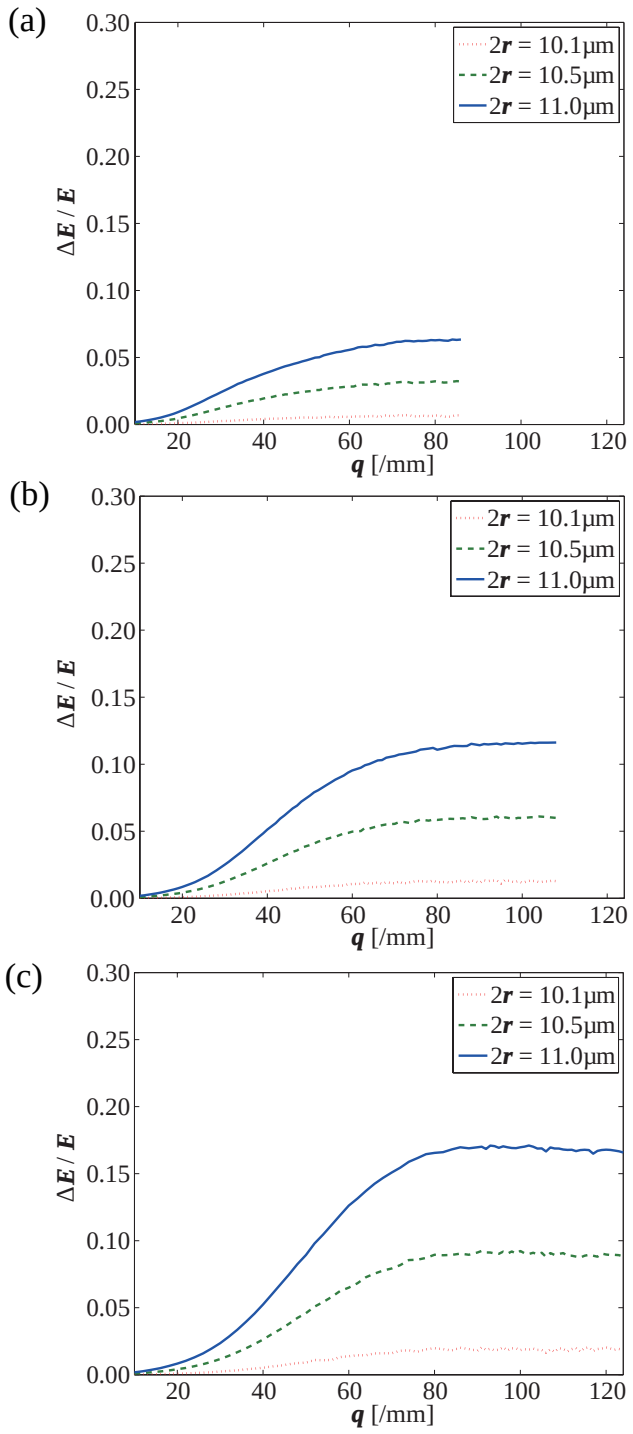

Figure 3.16: Normalized signal differences $\Delta E/E$, as function of various q, for 3 different b of 1000 s/mm^2 (a), 2000 s/mm^2 (b) and 3000 s/mm^2 (c), when g=400 mT/m.

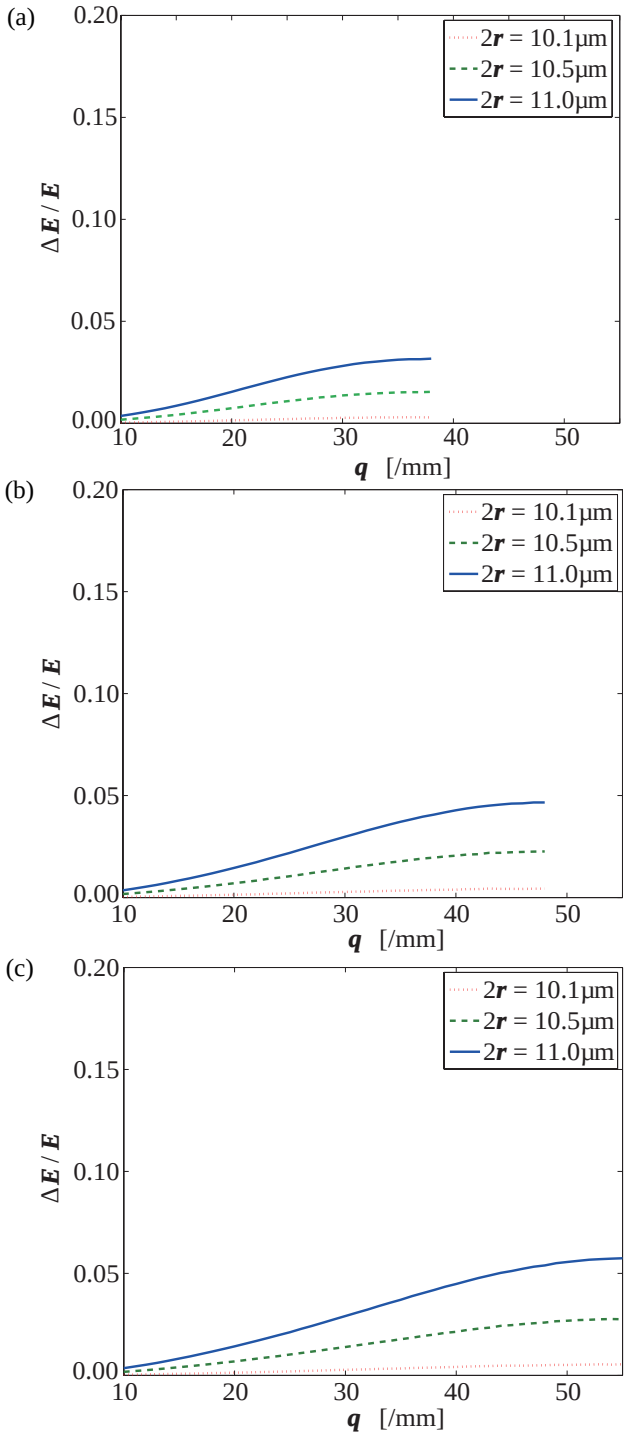

Figure 3.17: Normalized signal differences $\Delta E/E$, as function of various q, for 3 different b of 1000 s/mm^2 (a), 2000 s/mm^2 (b) and 3000 s/mm^2 (c), when g=25$\sqrt{2}$ mT/m.

(3.6) and determined by gyromagnetic ratio γ, the amplitude g and the duration time δ of MPG. For the DWI measurement, γ is fixed because we just focus on protons, and therefore, the q-value is determined by g and δ. In the simulation, to observe the impact of the q-value with wide range of values we set q from 0 to 300 /mm assuming g of 20000 mT/m. Consequently, we could observe how the q-value affected the normalized signal intensities of DWI based on its relationship to the duration time and the separation time of MPG as we stated in Subsection 3.6.2; we propose the importance of q-value for DWI.

Furthermore, the phantom studies with capillary plates revealed that the normalized signal intensities of DWI changed depending on both of the b-value and q-value; they decreased with increasing q-value as the simulations showed. The comparison between the simulation results and the results of phantom studies showed that they had the same tendency for the q-value dependence; this result suggests that we could properly simulated the motions of water molecules and acquired signals for DWI measurement.

Thereafter, the simulation results of determination of appropriate parameters demonstrated that the normalized signal differences between before and after cell swelling change with various q-values; similar tendencies were observed in all b-values. As shown in Figures 3.16 and 3.17, we could obtain the larger differences with larger b-values thus, we should select a large b-value as the appropriate MPG parameter for DW-fMRI. However, if we select a large b-value such as b of 2000 s/mm^2 or 3000 s/mm^2, we acquire too-large reduction in signal intensities, as well as noisy images in actual imaging. Hence, though we should select as large a b-value as possible, it must not be so large as to be greatly influenced by noise, in which case, we would need to improve the SNR.

Moreover, we discuss the q-value dependence of the normalized signal differences. As for the case with g of 400 mT/m, the normalized signal differences largely depended on the q-value and the differences reached the peak value at the q-value of approximately 80 /mm with all the b-values. The resuts indicated that there exist appropriate values for the q-value in every settings to emphasize the normalized signal differences caused by the change in the size of restriction. Therefore, we should choose appropriate values for q-value in DW-fMRI.

The simulation with g of $25\sqrt{2}$ mT/m showed similar results with those with g of 400 mT/m; the normalized signal differences largely depended on the q-value. However, the range of q-value was smaller than that in the simulation with g of 400 mT/m, and therefore, the normalized signal differences were also smaller than those of that simulation with all the b-values. The results indicate that we can obtain the larger differences with the larger q-value with g of $25\sqrt{3}$ mT/m. In addition, since the 3 T MR scanner requires at least 3 ms for the π pulse between MPG, the q-value that we can set on the apparatus is limited in actual measurements as follows: 36, 46 and 53 /mm for b of 1000, 2000 and 3000 s/mm^2, respectively. Considering these facts that the 3 T MR scanner provides the

small amplitude of MPG and there is 3 ms required for π pulse, we should choose as large values as possible with the current apparatus for DW-fMRI.

Additionally, in actual measurements the normalized signal differences has to be distinguished from noise. The noise of MR images depend on the MR scanner, sequence and condition that we use. In the study, we investigated appropriate values for the parameters based on the simulations, we did not considered the SNR of MR images. However, Le Bihan et al., who achieved imaging studies of DW-fMRI, reported that they could detect differences of MR signals and observed the differences by 1.73–2.02% with a 3 T MR scanner using b of 1800 s/mm^2 and TE of 87 ms [15]. Here, in our simulations, which we assumed the 3 T MR scanner, the parameter set with b of 1000, 2000 s/mm^2 and assumed TE of 135 ms (at most) are similar to their values. The results acquired with the setting showed the normalized signal differences by approximately 2–5%. The value of TE that we used was longer than that used by Le Bihan et al. and we expect the larger decay of the normalized signal intensities and the decrease of SNR, however, we can solve this problem by choosing b of 1000 s/mm^2. Therefore, the comparison of our simulation results with those by Le Bihan et al. suggests that the normalized signal differences observed in our simulations are detectable in DWI measurement. However, further investigations such as improvement of SNR or suppression of influences of noises or artifacts are still necessary to detect smaller differences of MR signal.

Chapter 4

An explanation of signal changes in DW-fMRI

In the previous chapter, we showed the importance of choosing certain DW-fMRI parameters and observed the influences of these parameters on the DWI signal intensities by using Monte Carlo simulations [62]. In that study, we employed a simple 2D circle simulation model with only one compartment to determine the influence of the size of the restricted structures and to simplify the required calculations. We assumed the presence of water molecules around cortical cells while ignoring the differences between intracellular and extracellular regions. Thus, we could not simulate the changes in water diffusion in the intracellular and the extracellular regions simultaneously.

In the present chapter, we improved our simulation model to a 3D cube with two compartments, corresponding to the intracellular and extracellular regions, and we investigated the DWI signal intensities and the differences between them before and after cell swelling. By using this simulation model with two compartments, we can discriminate the intracellular and extracellular regions, and observe not only the changes in DWI signal intensities in each region individually but also the changes in the total DWI signal intensities. Moreover, we can observe how water molecules in the two regions affect the DWI signal intensities simultaneously. Our new models should enable the implementation of a more detailed simulation.

In the DW-fMRI method, we observed that the DWI signal intensities changed because of changes in the ADCs of water molecules. To investigate how and why the DWI signal intensities change, i.e., how and why the ADCs change after cell swelling, we estimated the DWI signal intensities by using Monte Carlo simulations.

4.1 Simulation model

Cortical cells in the brain primarily consist of neurons and glial cells that swell upon brain activation [18]. In this simulation, we modeled water diffusion around cells whose

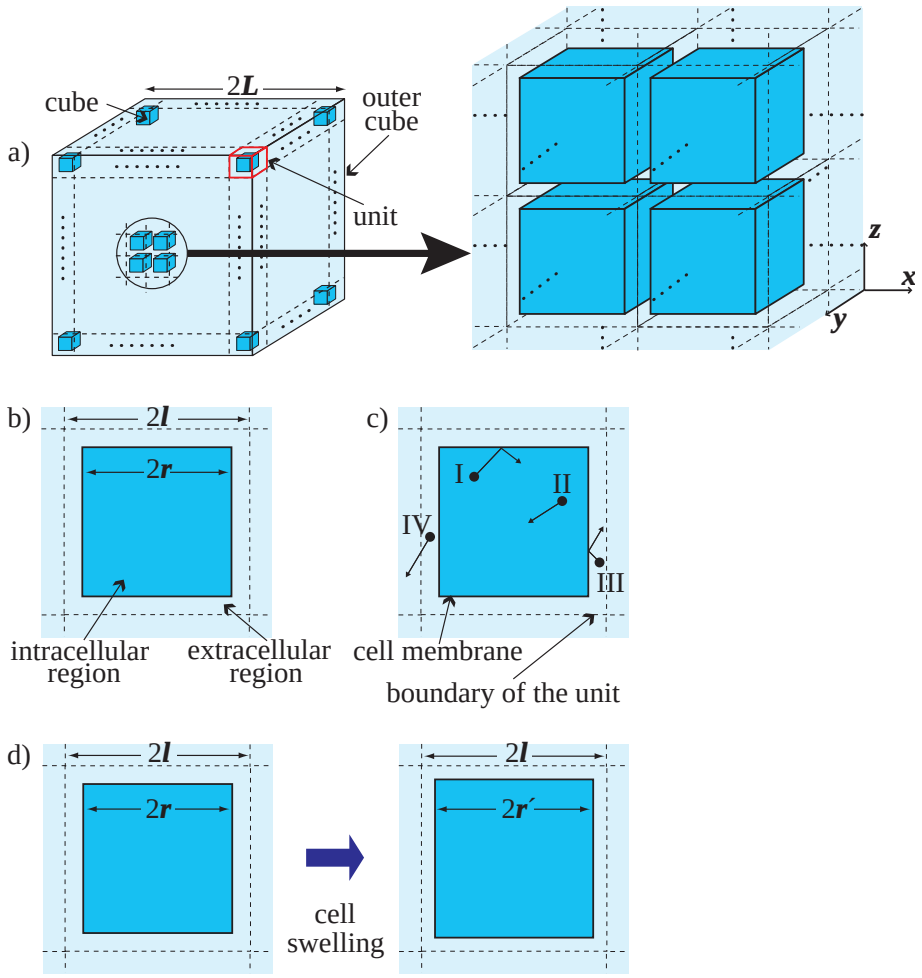

Figure 4.1: 3D cubic simulation model with two compartments. (a) Cubic cells are arranged regularly in the x, y, and z directions. (b) Dark- and light-color regions represent the intracellular and the extracellular regions, respectively. (c) Solid lines indicate the boundaries of the intracellular and the extracellular regions and mean cell membranes. Dotted lines indicate the boundaries of the units used for calculation. In the intracellular region, water molecules that reach the solid lines are reflected (I). Water molecules that do not reach the solid lines diffuse within the intracellular region (II). In the extracellular region, water molecules that reach the solid lines are reflected (III). Water molecules that reach the dotted lines diffuse through the dotted lines (IV). (d) With respect to cell swelling, the size of the cubic cells increased from $2r$ to $2r'$, whereas that of the cubic units did not change.

diameters were approximately 5–100 μm [59], and we employed a 3D cubic simulation model (Figure 4.1) with two compartments. The cells are modeled as cubes; the inner region of the cube with solid lines indicates the intracellular region, and the region outside these lines indicates the extracellular region. In Chapter 3 we simulated water molecules diffusing in the 2D circle region and observed how the restriction for water diffusions affected DWI signal intensities. In the present chapter we employed the 3D simulation model and made the restricted regions cubic to achieve arbitrary filling factor of the intracellular regions. The filling factor was prioritized to the shape of restricted regions in the simulation. By using this simulation model, we investigated the influences of changes in the volume ratio on DWI signal intensities.

We assumed that water molecules diffused according to a normal distribution and were reflected at the solid lines, which are the boundaries between the intracellular and extracellular regions, as shown in Figure 4.1. Water molecules in the extracellular region diffused through the dotted lines, which are the boundaries for the units of calculation. Water molecules are reflected at the surface of the outer cube. The effect of reflection at the surface of the outer cube should be considered because water diffusion in the extracellular region is restricted. Therefore, we set as many cubic units as possible in the outer cube and decreased the ratio of volume in which water molecules are reflected at the surface of the outer cube.

In this simulation, we calculated the changes in positions and the phase of the magnetization precession of protons in water molecules diffusing near restricted structures.

4.2 Simulation algorithm

Simulations were conducted using Microsoft Visual C++. As is the same with the simulation in Chapter 3, the obtained signal is represented as normalized signal intensity, which can be obtained by dividing the signal intensity with MPG by that without MPG.

1. We used an outer cube with a length of $2L$ on each side, which included X cubes with a length of $2r$ on each side, in the 3D space as a simulation model. This cube was divided into X sub-sections with lengths of $2l$ on each side. These sub-sections were referred to as units. X cubes in the intracellular regions were regularly spaced in three directions and separated by the extracellular region at an interval of $2l-2r$.

2. We arranged Z water molecules whose default positions were distributed uniformly in the outer cube.

3. We set Δt as a time step and renewed the position of each water molecule according to the Einstein–Smoluchowski equation. We renewed the positions of each water

molecule according to a normal distribution with mean 0 and variance $2D\Delta t$ in each direction as follows:

$$\begin{aligned} \mathbf{p}_k(t+\Delta t) &= \mathbf{p}_k(t) + N[\mathbf{a}, \mathbf{C}] \\ k &= 1, 2, 3, \cdots, Z \\ \mathbf{a} &= \begin{pmatrix} 0 & 0 & 0 \end{pmatrix} \\ \mathbf{C} &= \begin{pmatrix} 2D\Delta t & 0 & 0 \\ 0 & 2D\Delta t & 0 \\ 0 & 0 & 2D\Delta t \end{pmatrix} \end{aligned} \tag{4.1}$$

where $\mathbf{p}_k(t+\Delta t)$ is the position of each water molecule, and $N[\mathbf{m},\ \sigma^2]$ is a 3D random number following a normal distribution with mean $\mathbf{m}$ and variance σ^2. When a water molecule reached the intracellular and the extracellular boundaries or the surface of the outer cube, we renewed its position to reflect that it was at the boundary or surface.

4. We renewed the phases of transverse magnetization in each water molecule, while MPG was applied according to the Stejskal-Tanner plus sequence shown in Figure 2.21. Thus, phase changes (θ) at every coordinate axis were calculated as follows:

$$\begin{aligned} \theta_{k,i}(t) &= \gamma g_i \int_t^{t+\Delta t} p_{k,i}(\tau) d\tau \\ k &= 1, 2, 3, \cdots, Z \\ i &= x, y, z \end{aligned} \tag{4.2}$$

where g_x, g_y, and g_z are the amplitudes of MPG along the x-, y-, and z-axis, respectively. In addition, all phases were inverted when the 180 ° RF pulse was applied. The phase of each water molecule obtained at $t = TE$ was calculated as follows:

$$\begin{aligned} \theta_{k,i} &= -\sum_{j=0}^{n} \theta_{k,i}(j\Delta t) + \sum_{j=0}^{n} \theta_{k,i}(\Delta + j\Delta t) \\ k &= 1, 2, 3, \cdots, Z \\ i &= x, y, z \\ n &= \frac{\delta}{\Delta t} \end{aligned} \tag{4.3}$$

where the first MPG was applied at $t = 0$. TE is an echo time.

5. We calculated the normalized signal intensity E of DWI from the phases of transverse magnetization as follows:

$$\begin{aligned} E &= \frac{S}{S_0} \\ &= \frac{1}{Z}\sqrt{(\sum_{k=1}^{Z}\cos\theta_k)^2 + (\sum_{k=1}^{Z}\sin\theta_k)^2} \\ \theta_k &= \theta_{k,x} + \theta_{k,y} + \theta_{k,z} \end{aligned} \tag{4.4}$$

where S is the signal intensity with MPG and S_0, that without MPG.

6. We obtained the final normalized signal intensities by repeating the same procedure R times and calculating the average of all normalized signal intensities.

4.3 Setting of simulations

In this section, we state parameter settings for simulations. The previous study in Section 3, we proposed importance of b-value and q-value as DWI parameters for DW-fMRI fixing the amplitude of MPG g and investigated their influences on the acquired DWI signal intensities by the Monte Carlo simulations. As is the same with the previous study, we used the same value of g in all the simulations and fixed it to $25\sqrt{3}$ assuming the value used in clinical 3 T-MR scanners in the simulations with 3D and 2 compartment model for DW-fMRI. However, we focused on b-value and separation time Δ in the simulation. This is because the q-value depends on duration time δ with fixed g and it determines Δ if b-value is fixed. As a result, the influences of Δ is considered to be dominant for acquiring the normalized signal intensities in the simulations as we realized in Subsection 3.6.2. Thus, it is not q-value but Δ that we should investigate and choose appropriate values for. Furthermore, there are both intracellular and extracellular regions in the simulation model, and therefore, we also focused on the size of restriction, that is the length of cubic cells, to demonstrate impact of volume ratio of intracellular regions on the simulation results.

First, we investigated how the DWI signal intensities change in the intracellular and extracellular regions after cell swelling, respectively. We calculated the normalized signal intensities in the intracellular and the extracellular regions as well as in the total region when the size of cubic cells changes in our model. We set b and Δ to 1000 s/mm^2 and 45.05 ms, respectively while changing the r range. These parameters are shown in Table 4.1.

Next, we observed the normalized signal differences by assuming that the size of the cubic cells increases from 10.0 μm to 10.1, 10.5 and 11.0 μm. We calculated the signal

differences ΔE by subtracting the normalized signal intensities before the cell swelling from those after the cell swelling as we did in the previous chapter. In addition, by dividing the signal differences by the normalized signal intensities after the cell swelling, we obtained the normalized signal differences $\Delta E/E$ with the unit of %. The simulation offered b and Δ dependence of $\Delta E/E$ to show how large $\Delta E/E$ are affected by those parameters after cell swelling under our assumption. The parameters of these simulations are shown in Tables 4.2 and 4.3.

In every simulation, we set $2r$ to 10 μm to consider the size of the cell and $2l$ to 11.262 μm to set the volume ratio of the intracellular and extracellular regions to 70% [63, 64]. Moreover, we assumed that a cell with a length of 10 μm on each side swelled by 1–10% in length, while $2l$ is fixed to 11.262μm. $2L$ was fixed to 112.62 μm, resulting in $X = 10$. In the simulations, water molecules were reflected at the surface of the outer cube. We also set D_{int} to 1.0×10^{-3} mm^2/s and D_{ext} to 3.0×10^{-3} mm^2/s [63, 64]. The remaining parameters were $Z = 10^6$, $\Delta t = 100$ μs, and $R = 10$. These parameters were fixed for every simulation, as shown in Table 4.4. To investigate influences of the diffusion of water molecules on DWI signal intensities, we focused on the normalized signal intensities while ignoring the T_2 decay.

4.4 Results

This section demonstrates the results of simulations to investigate the influences of the size of restriction and MPG parameters, b and Δ. First, we obtained the normalized signal intensities in the intracellular and extracellular regions by the simulation while changing the length of cubic cells from 10.0 to 11.0. As well as the normalized signal intensities in each regions, we obtained those of total regions.

In addition, we obtained the normalized signal intensities of the intracellular, extracellular and total region to determine the influences of the b-value and the separation time. We also calculated the normalized signal differences, which can be calculated by subtracting the normalized signal intensities after cell swelling from those before cell swelling, in the simulations for investigating the influences of the b-value and the separation time.

Table 4.1: Parameters for simulations to determine r dependence in intracellular and extracellular regions.

b[s/mm^2]	$2r$[μm]	g[mT/m]	δ[ms]	Δ[ms]
1000	10.0 | 11.0	$25\sqrt{3}$	13.56	45.05

Table 4.2: Parameters for simulations to observe b dependence.

b[s/mm^2]	$2r$[/mm]	$2r'$[/mm]	g[mT/m]	δ[ms]	Δ[ms]
500		10.1		11.97	
|	10.0	|	$25\sqrt{3}$	|	30
2400		11.0		29.87	
500		10.1		9.44	
|	10.0	|	$25\sqrt{3}$	|	45
3000		11.0		24.65	
500		10.1		8.07	
|	10.0	|	$25\sqrt{3}$	|	60
3000		11.0		20.51	

Table 4.3: Parameters for simulations to determine Δ dependence.

b[s/mm^2]	$2r$[/mm]	$2r'$[/mm]	g[mT/m]	δ[ms]	Δ[ms]
		10.1		10.85	66.94
1000	10.0	|	$25\sqrt{3}$	|	|
		11.0		22.24	22.48
		10.1		10.85	130.27
2000	10.0	|	$25\sqrt{3}$	|	|
		11.0		27.66	28.70
		10.1		10.85	193.59
3000	10.0	|	$25\sqrt{3}$	|	|
		11.0		32.00	32.50

4.4.1 Size of restricted region

Simulation results of the intracellular and extracellular regions are shown in Figure 4.2 with b of 1000 s/mm^2. These results show the normalized signal intensities with changes in the length of the cubic cell. Squares and triangles indicate the normalized signal intensities in the intracellular and extracellular regions, respectively. These results indicated that the DWI signal intensities decreased with the increase of $2r$ in the intracellular region, whereas the intensities increased with the increase of $2r$ in the extracellular region. These changes in the DWI signal intensities resulted from changes in the apparent diffusion coefficients. In the intracellular region, water molecules can move for a longer distance when $2r$ increases, and therefore, the apparent diffusion coefficient of this region seems to increase with larger $2r$. In contrast, in the extracellular region, the restriction for the movement of water molecules becomes stronger when $2r$ increases, and therefore, the apparent diffusion coefficient of this region seems to decrease with larger $2r$. Figure 4.2

Table 4.4: Values of parameters Z, Δt, D_{int}, D_{ext}, and M were used in all simulations.

Z	$\Delta t[\mu s]$	$D_{\mathrm{int}}[\mathrm{mm}^2/\mathrm{s}]$	$D_{\mathrm{ext}}[\mathrm{mm}^2/\mathrm{s}]$	R
10^6	100	1.0×10^{-3}	3.0×10^{-3}	10

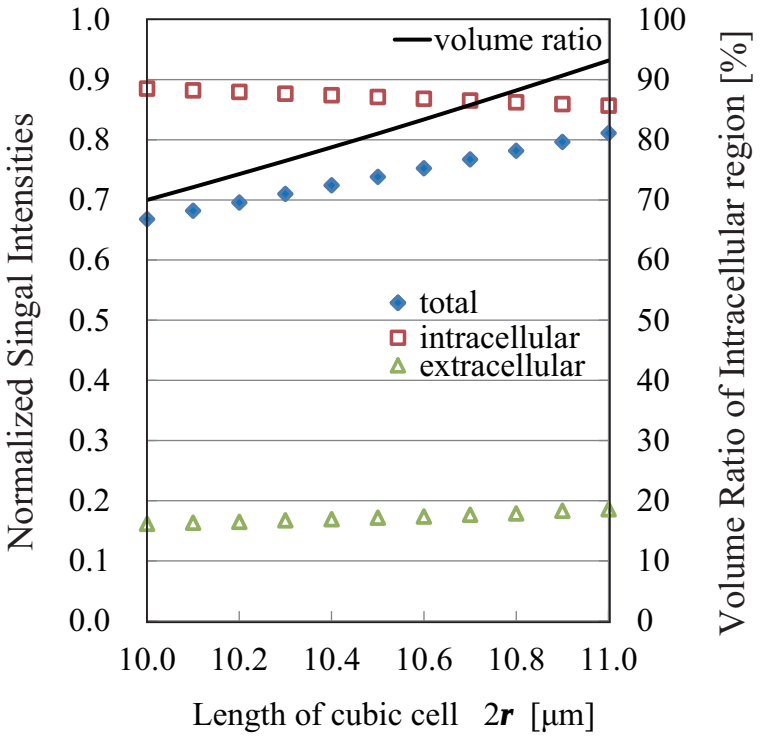

Figure 4.2: Normalized signal intensities E as function of $2r$ for b-values of 1000 s/mm^2 and Δ of 45.05 ms, when g=25$\sqrt{3}$ mT/m; total signal intensities (♦), intracellular ones (□), extracellular ones (△), and intracellular volume ratio(–).

also shows that the normalized signal intensity is much larger in the intracellular region than in the extracellular region. The reason for these results is that the apparent diffusion coefficient in the intracellular region is much smaller than that in the extracellular region.

Moreover, diamonds and a solid line indicate the total normalized signal intensities and the intracellular volume ratio, respectively. Considering the volume ratio between the intracellular and extracellular region, the intracellular volume is much larger than the extracellular one, and then, the contribution of the intracellular region to total normalized signal intensities is supposed to be dominant. Therefore, we can interpret that the total normalized signal intensities decrease after cell swelling because these intensities decrease in the intracellular region. The diamonds, however, suggest that the total normalized signal intensities increase with the increase in $2r$. This is because the intracellular volume

ratio increases and the ratio of water molecules in the intracellular region, which have larger normalized signal intensities, increases. According to these results, we can conclude that the increases in the intracellular volume ratio have greater effect on the changes in the total normalized signal intensities than the DWI signal changes in each region.

4.4.2 B-value

Figures 4.3 – 4.5 showed the normalized signal intensities E_{total}, E_{int} and E_{ext} as a function of b for Δ of 30, 45 and 60 ms, respectively. E_{total}, E_{int} and E_{ext} indicate the normalized signal intensities in total, intracellular and extracellular regions of the simulation model, respectively. The size of restriction was set as $2r$ = 10.0, 10.1, 10.5 and 11.0. All the figures showed that the normalized signal intensities decreased with increasing b-value, which can be expect from the Equation (2.42). They also showed that the normalized signal intensities decreased with the increase of $2r$ in intracellular region because a larger value of $2r$ provided a larger space where water molecules could move longer. In contrast, the normalized signal intensities in the extracellular region increased with the increase of $2r$ because a larger value of $2r$ decreased the space for diffusion of water molecules. As for the results in the total region, we obtained the increasing normalized signal intensities with the increase of $2r$, which was consistent with the results in Subsection 4.4.1.

Additionally, we examined the b-value dependence of the normalized signal differences $\Delta E/E$ with the changes in cell size. Figure 4.6 showed the results with Δ of 30 ms (a), 45 ms (b), and 60 ms (c) assuming that the cell size increased from 10 μm to 10.1, 10.5 and 11.0 μm. From the results of the b-value dependence, we obtained the largest differences for b of 1700–1800 s/mm^2. Thus, we expect larger ΔE values using such b-values in DW-fMRI experiments.

4.4.3 Duration of MPG

Figures 4.7 – 4.9 showed the normalized signal intensities E_{total}, E_{int} and E_{ext} as a function of Δ for b of 1000, 2000 and 3000 s/mm^2, respectively. E_{total}, E_{int} and E_{ext} indicate the normalized signal intensities in total, intracellular and extracellular regions of the simulation model, respectively. The size of restriction was set as $2r$ = 10.0, 10.1, 10.5 and 11.0. All the figures showed that the normalized signal intensities increased with increasing Δ. This is because Δ determines the time during which water molecules can move and also the distance of their movement. Therefore, Δ affects how the restriction is weighted in acquiring the DWI signal intensities, as we stated in Subsection 3.6.2. They also showed that the normalized signal intensities decreased with the increase of $2r$ in the intracellular region because a larger value of $2r$ provided a larger space where water molecules could move longer. In contrast, the normalized signal intensities in the

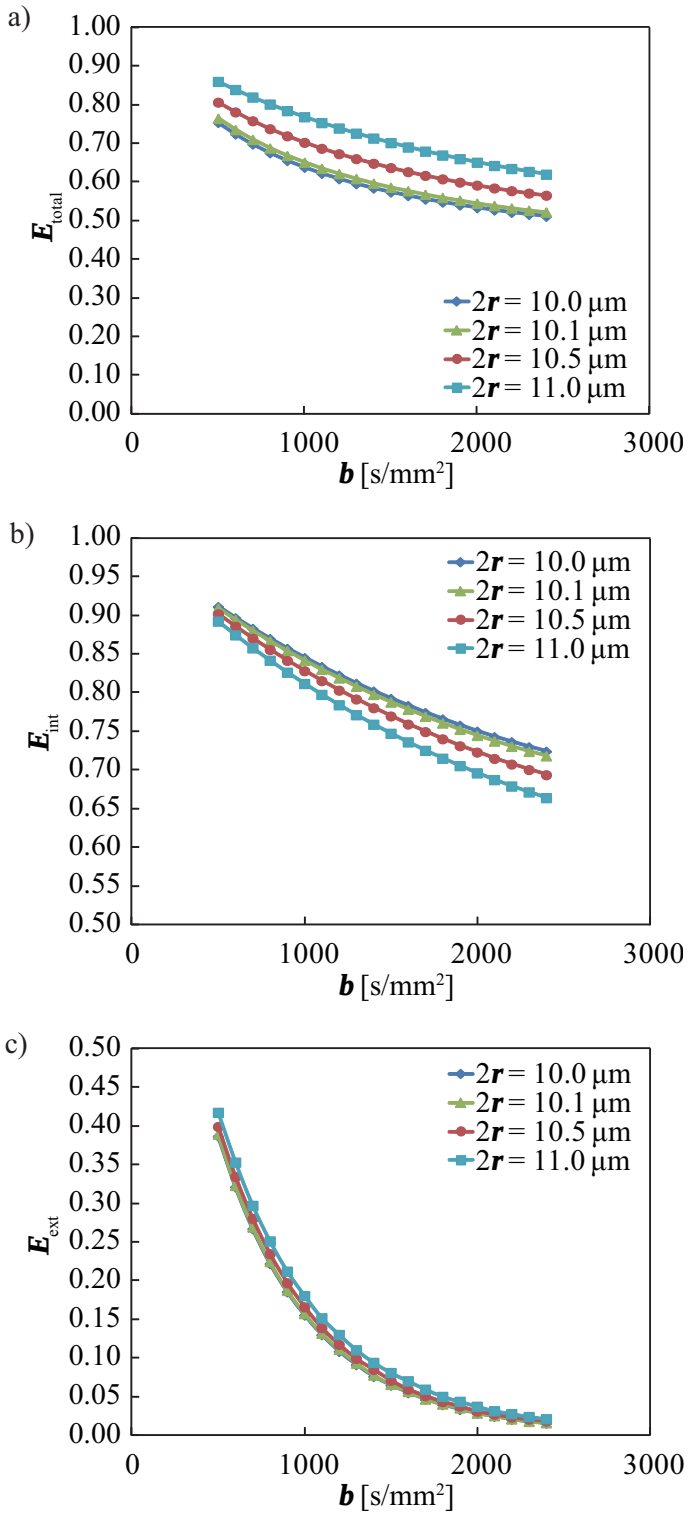

Figure 4.3: Normalized signal intensities E_{total}, E_{int} and E_{ext} in total (a), intracellular (b), and extracellular (c) regions as function of b for Δ of 30 ms when g=$25\sqrt{3}$ mT/m.

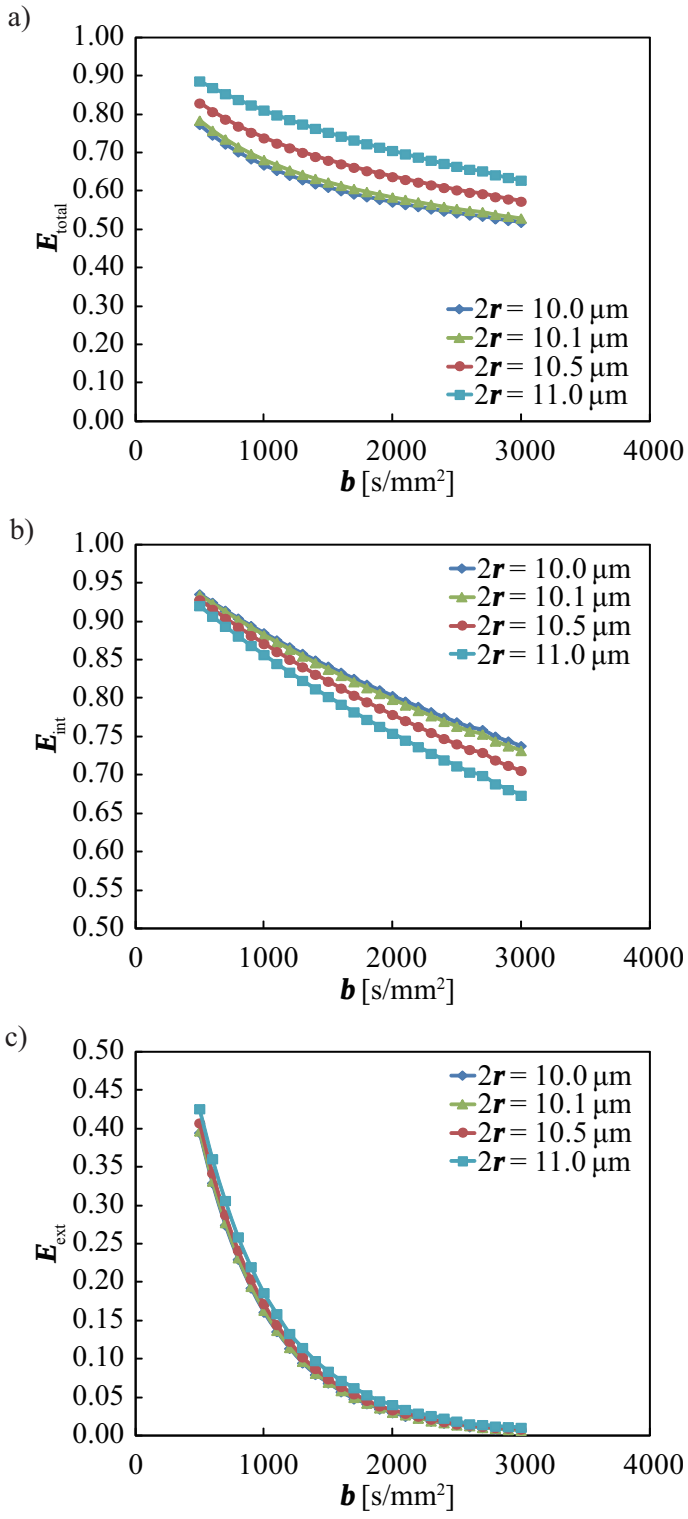

Figure 4.4: Normalized signal intensities E_{total}, E_{int} and E_{ext} in total (a), intracellular (b), and extracellular (c) regions as function of b for Δ of 45 ms when g=$25\sqrt{3}$ mT/m.

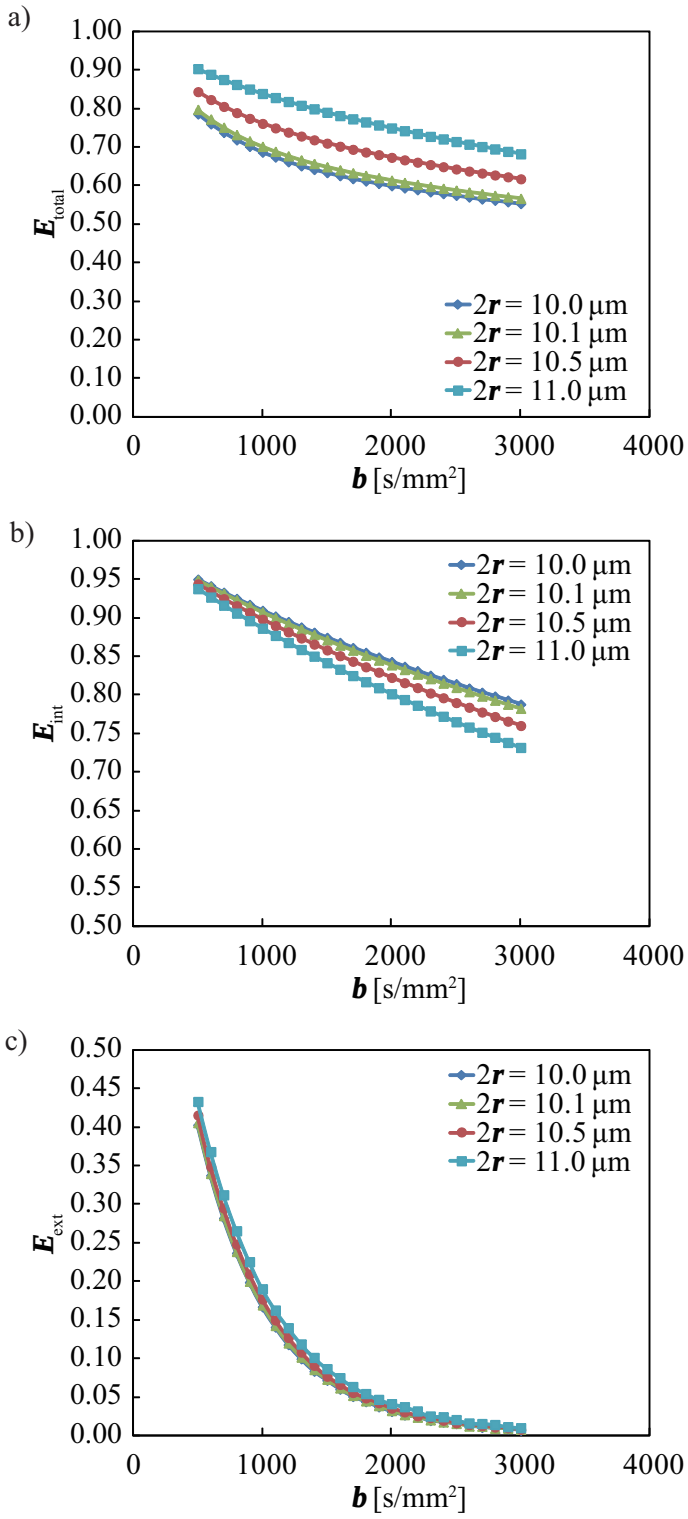

Figure 4.5: Normalized signal intensities E_{total}, E_{int} and E_{ext} in total (a), intracellular (b), and extracellular (c) regions as function of b for Δ of 60 ms when g=$25\sqrt{3}$ mT/m.

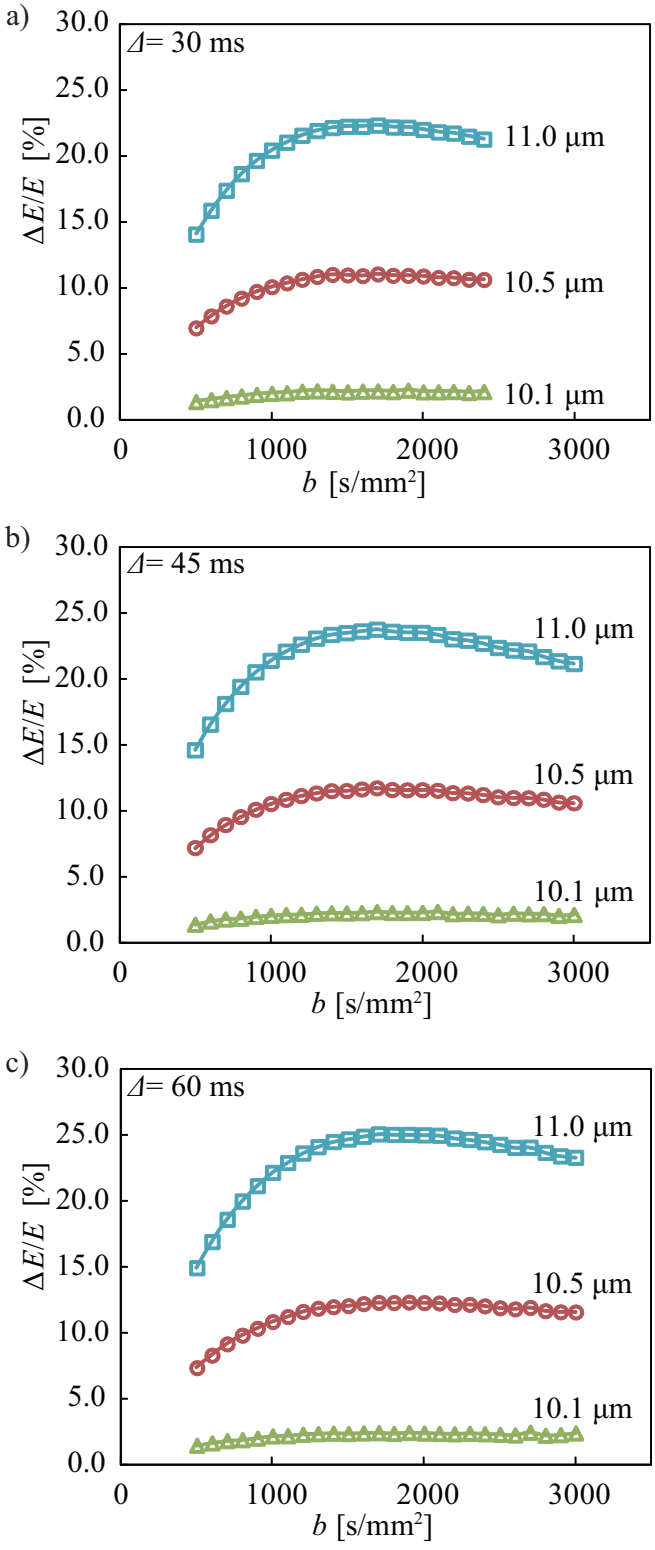

Figure 4.6: Normalized signal differences $\Delta E/E$ as function of b for Δ of 30 ms (a), 45 ms (b), and 60 ms (c) when g=$25\sqrt{3}$ mT/m.

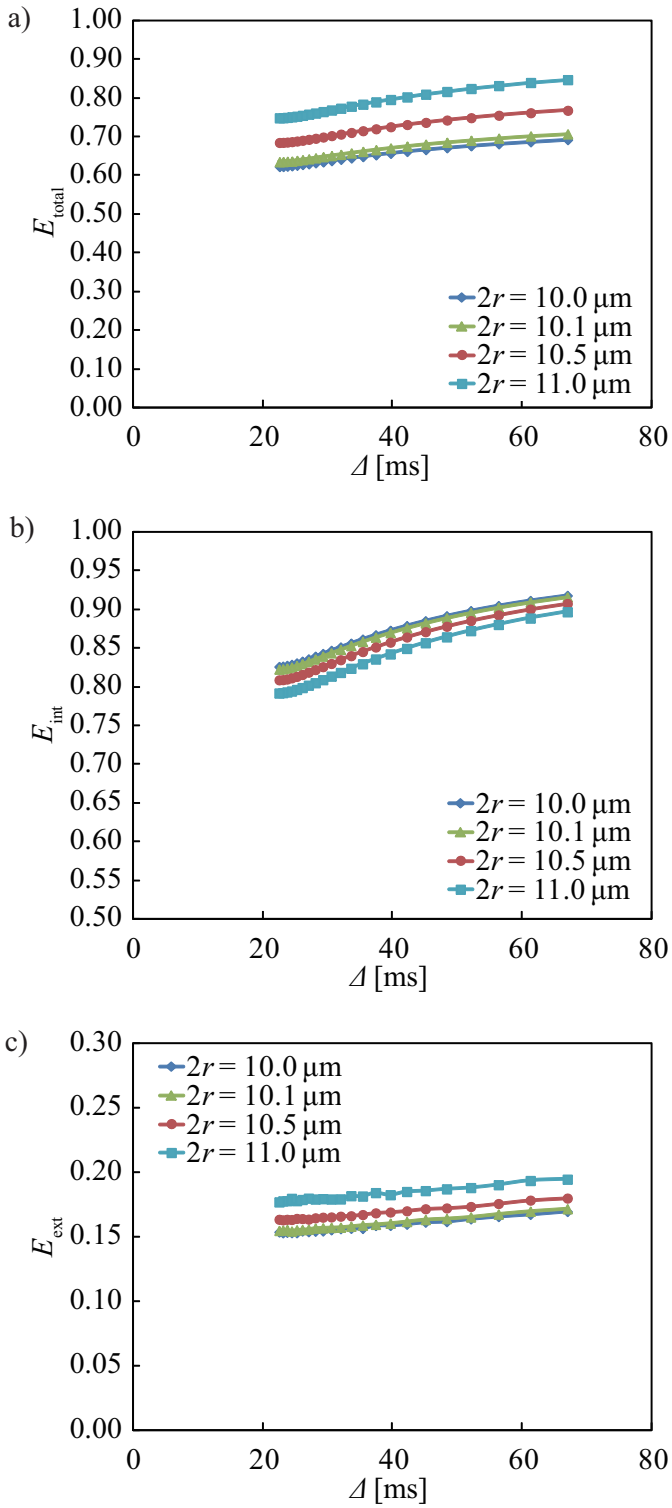

Figure 4.7: Normalized signal intensities E_{total}, E_{int} and E_{ext} in total (a), intracellular (b), and extracellular (c) regions as function of Δ for b of 1000 s/mm^2 when g=$25\sqrt{3}$ mT/m.

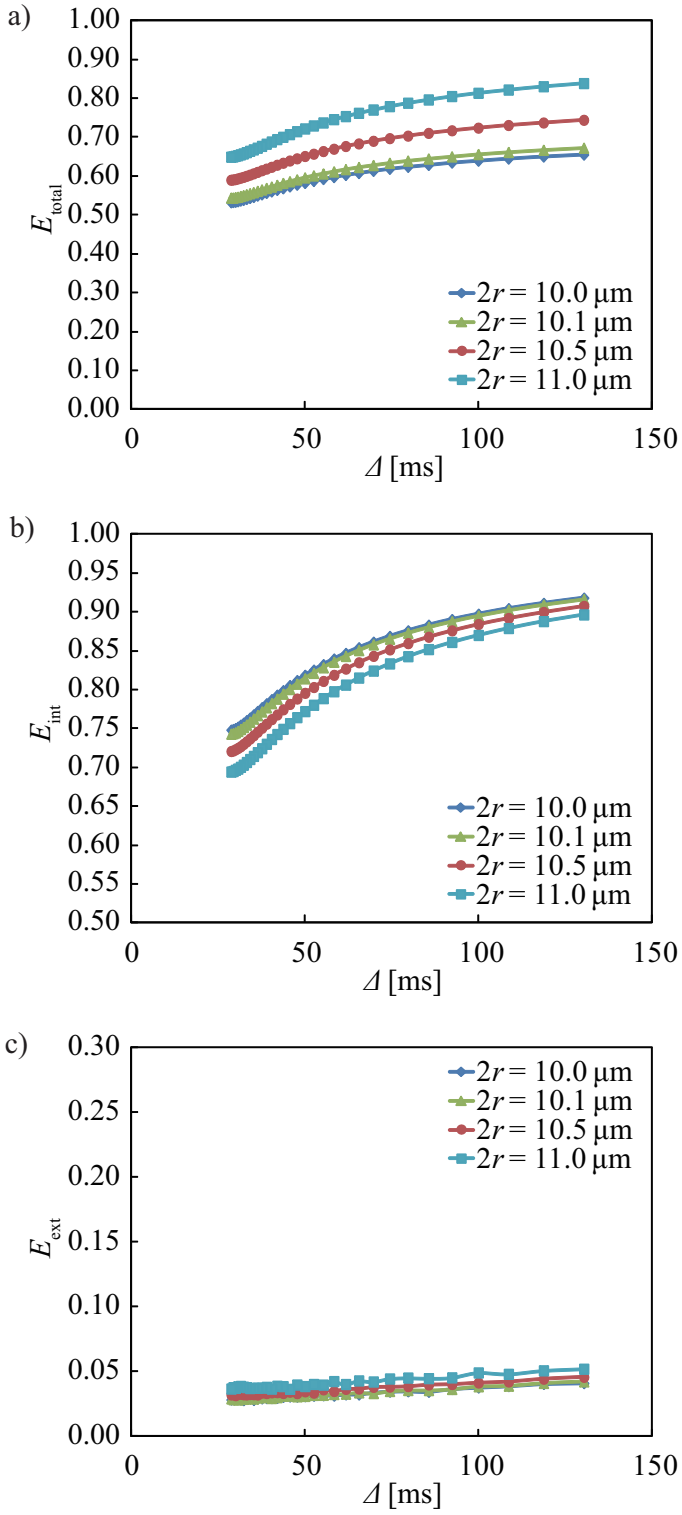

Figure 4.8: Normalized signal intensities E_{total}, E_{int} and E_{ext} in total (a), intracellular (b), and extracellular (c) regions as function of Δ for b of 2000 s/mm^2 when g=$25\sqrt{3}$ mT/m.

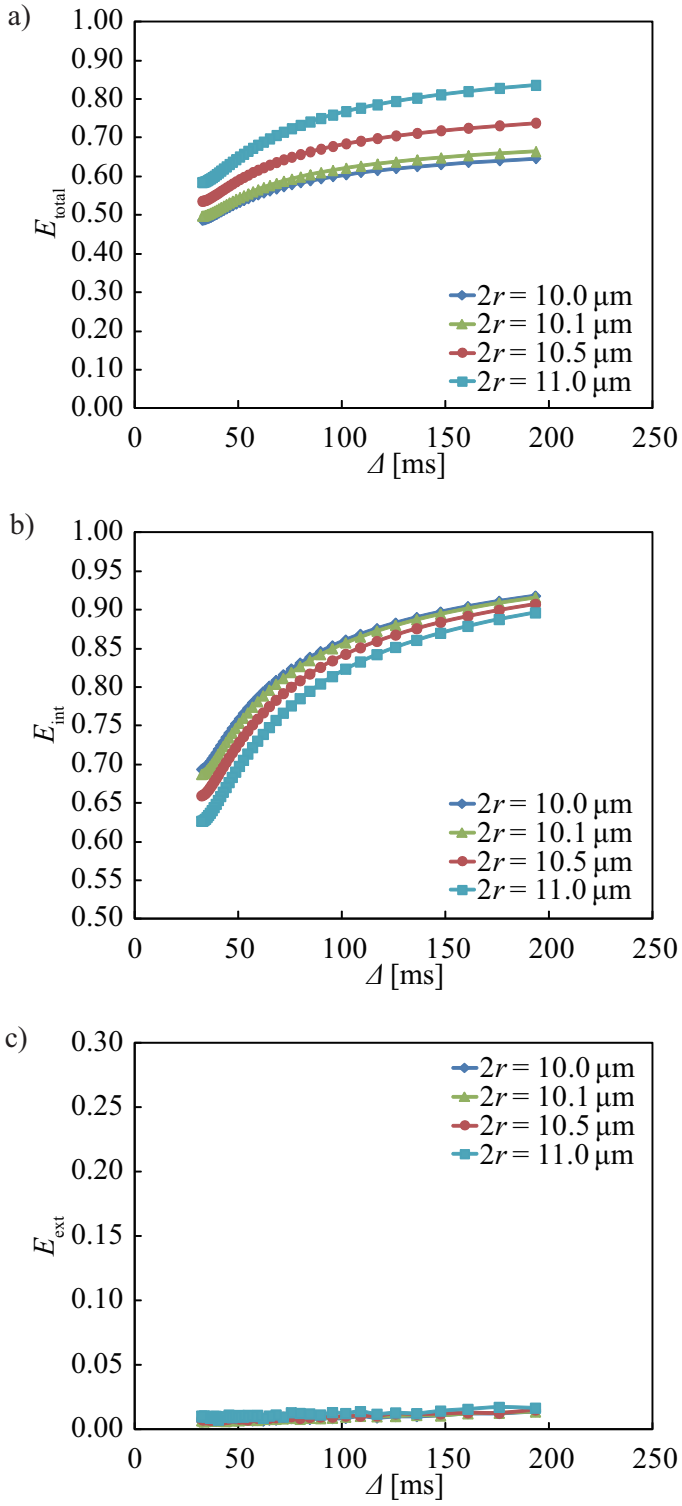

Figure 4.9: Normalized signal intensities E_{total}, E_{int} and E_{ext} in total (a), intracellular (b), and extracellular (c) regions as function of Δ for b of 3000 s/mm^2 when g=$25\sqrt{3}$ mT/m.

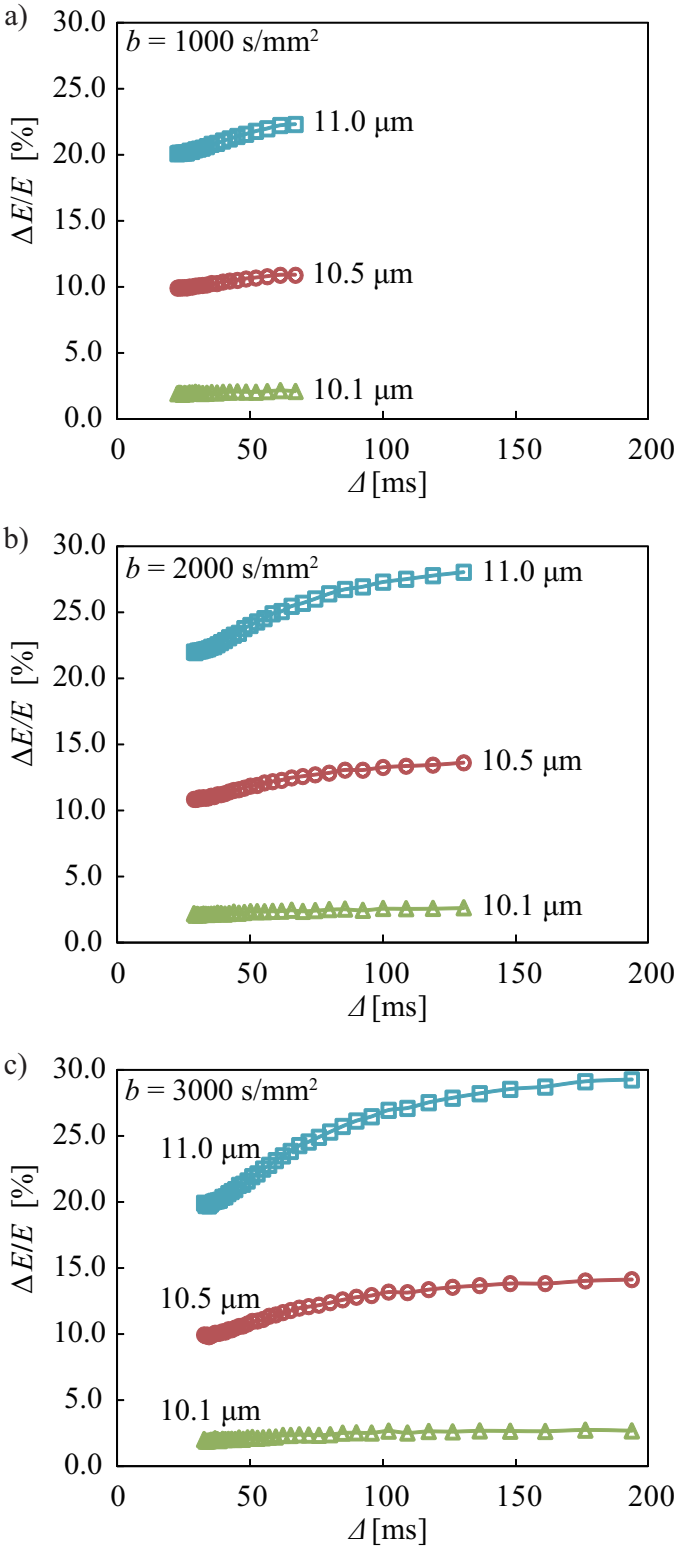

Figure 4.10: Normalized signal differences $\Delta E/E$ as function of Δ for b-values of 1000 s/mm^2 (a), 2000 s/mm^2 (b), and 3000 s/mm^2 (c), when g=25$\sqrt{3}$ mT/m.

extracellular region increased with the increase of $2r$ because a larger value of $2r$ decreased the space for diffusion of water molecules. As for the results in the total region, we obtained the increasing normalized signal intensities with the increase of $2r$, which was consistent with the results in Subsection 4.4.1.

Figure 4.10 showed the normalized signal differences $\Delta E/E$ as the length of the cubic cells increased from 10.0 μm to 10.1, 10.5 and 11.0 μm assuming cell swelling. We set the b to 1000 s/mm^2 (a), 2000 s/mm^2 (b), and 3000 s/mm^2 (c) and changed Δ to investigate the Δ dependence of $\Delta E/E$. As in the case of the simulation results of the b-value dependence, the differences increased with an increase in Δ for all b-value settings. On the basis of these results, the largest value of the separation time is preferable to emphasize the differences.

4.5 Discussion

We simulated the diffusion of water molecules and investigated the changes in the DWI signal intensities after cell swelling. In the simulation, we assumed that water molecules did not pass through the cell membrane (except when cell swelling occured) in order to observe how water diffusion affects the differences in the normalized signal intensities of DW-fMRI and to simplify the calculations. We also assumed that the density ratio of water molecules in the intracellular and extracellular regions was constant during cell swelling.

We expanded our previous simulation model in the present study to consider influences of the intracellular and extracellular regions on DWI signal intensities in DW-fMRI. As we showed in the result section, we obtained increased normalized signal intensities after cell swelling. This is because the intracellular volume ratio increased in the present simulation. This implies that the increase in the number of water molecules in the intracellular regions, which have smaller apparent diffusion coefficients, results in larger DWI signal intensities after cell swelling. On the other hand, in our previous simulation model with one compartment, we could only observe a change in the apparent diffusion coefficients of water molecules resulting from the increase of the size of the restricted region.

Our previous simulation model had only one compartment modeling one region and we could calculate the motion of water molecules only in that compartment. In that model, we assumed that the region expanded due to cell swelling. Therefore, the apparent diffusion coefficients increased and the normalized signal intensities decreased, which can be seen in Figure 4.2 as the decrease of the normalized signal intensities in the intracellular regions ($\square$).

In contrast, Figure 4.2 showed that the total normalized signal intensity increased when the size of cell increased. This is because the intracellular volume ratio increased.

This result might represent the advantage of the present model.

Previous studies by other groups [11, 15, 16, 17, 14] observed increased signals in DW-fMRI. For instance, a study showed decreased apparent diffusion coefficients, implying increased normalized signal intensities for about 1.57 % with b of 1443-1461 mm^2/s and this result was consistent with our result that the normalized signal intensities increased for about 2.17 % with b of 1400 mm^2/s, Δ of 30 ms, and r' of 10.1 μm [11]. In other studies, 1$\sim$2% increases of the raw signal intensities with the b of 1600–1800 mm^2/s ware reported [15, 16, 14]. In our simulations, we obtained 2.15–2.18 % increases in the normalized signal intensities with the b of 1600–1800 mm^2/s, Δ of 30 ms, and r' of 10.1 μm. Moreover, another study showed that the normalized signal intensities increased about 2–3 % with b of 1800 mm^2/s, which is comparable with 2.15 % signal increase with b of 1800 mm^2/s [17], Δ of 30 ms and r' of 10.1 μm in the present simulation results. These facts suggest that the present simulation model with two compartments is more reliable than our previous simulation model with one compartment.

Moreover, we obtained not only the normalized signal differences $\Delta E/E$ before and after cell swelling but also the duration time and the b-value dependences on ΔE. The simulation results showed ΔE after cell swelling as a function of Δ with three b-values; a similar tendency was observed for all the b-values. The separation time has a significant role in the DWI measurement, and, of course, in DW-fMRI, when focusing on restricted diffusion. In the human brain, water molecules undergo restricted diffusion, and therefore, we should consider the effect of the separation time in DW-fMRI. As shown in Figure 4.10, we determined how the separation time affected the differences. However, it should be ensured that the separation time is shorter than TE. If TE is too long, the normalized signal intensities decay to a great extent. The TE value in DWI is typically of the order of hundreds of milliseconds, although we use a stimulated echo sequence to avoid decay in signal intensities for long TE in DWI [65, 66]. Therefore, we should select the separation time smaller than TE in practical use.

In addition to the separation time dependence, we also observed the normalized signal differences between before and after cell swelling as a function of the b-value. Figure 4.6 shows that the b-value has an optimal value that emphasizes the differences while the separation time is fixed. A large b provides a large δ with fixed Δ and g. In addition, large δ provides large a θ because the large δ stacks the changes in θ, which can be seen in Equation (4.2). However, we should consider that θ larger than π or smaller than $-\pi$ is equal to $(\theta - \pi)$ or $(\theta + \pi)$, respectively, in the DWI signal intensities. Therefore, if we use a large b, we can obtain many water molecules with θ larger than π or smaller than $-\pi$, and we cannot reflect the diffusion of water molecules to the DWI signal intensities exactly. Then, there might be an optimal range of the b-value for DWI and DW-fMRI. This result implies that the b-value also plays a significant role when we observe the

normalized signal differences in DW-fMRI. In this regard, in a previous study by another group [15], we found that a b-value consistent with our proposal (around 2000 s/mm^2) was used. As for separation time, TE was set to 87 ms, and therefore, we should select as large a value as possible for the separation time in order to set TE to $\sim$ 90 ms considering experimental studies.

Chapter 5

Spin-lock imaging for direct detection of oscillating magnetic fields with MRI

In recent years, new fMRI methods, which are able to detect neural magnetic fields directly, have been expected [23, 24, 25, 26, 27, 28, 29]. Although no fMRI experiments have been reported in which neural magnetic fields have been successfully detected, some researchers claim that such fields are observable with MRI scanners [24, 26, 28, 29]. Researchers have been attempting to detect changes in the phase or magnitude of the magnetization generated by subtle and transient alternations of static magnetic fields (B_0) resulting from neural activities. However, these changes are weak and may be difficult to detect. In addition, phase cancellation induced by incoherent neuron orientation can influence the results obtained using this method [23, 25]. Among approaches of this fMRI method, the one that uses a spin-lock imaging sequence has attracted wide attention because it can possibly detect small oscillating magnetic fields.

In this chapter, we visualized magnetization performance during the spin-lock imaging sequence with externally applied oscillating magnetic fields, what we call the secondary magnetic resonance, to understand the mechanism of this approach. A fast-and-simple method with matrix operations was used to solve a time-dependent Bloch equation. Finally, we represented how the spin-lock imaging sequence interacts the oscillating magnetic fields based on the Bloch equation and we carried out fMRI measurements with the spin-lock imaging sequence. In addition, we investigated the influence of the duration of the spin-lock pulse in the spin-lock module, which interacts with the external oscillating magnetic fields, on MR signals. Furthermore, to detect minute magnetic fields of the order of sub-nT, we carried out phantom studies on the practical use of this method as an fMRI approach.

5.1 Principles of NMFD-fMRI

We begin with the Bloch equation [67, 68, 69] describing the relations between spin magnetizations and magnetic fields to describe the mechanism of the interaction between spin-lock imaging sequence and oscillating magnetic fields. The Bloch equation can be written as

$$\frac{d\boldsymbol{M}}{dt} = \gamma \boldsymbol{M} \times \boldsymbol{B}, \tag{5.1}$$

where $\boldsymbol{M} = (M_x, M_y, M_z)$ and $\boldsymbol{B} = (B_x, B_y, B_z)$ are the net magnetization of interested spins and applied magnetic fields, respectively. In the equation, $d\boldsymbol{M}/dt$ is a speed vector of $\boldsymbol{M}$ and denotes a direction of which $\boldsymbol{M}$ move into.

In addition, if we assume that the equilibrium state of the net magnetization $\boldsymbol{M} = (0, 0, M_0)$, influences of relaxation of the net magnetization can be written as

$$\begin{aligned} \frac{dM_x}{dt} &= -\frac{M_x}{T_2} \\ \frac{dM_y}{dt} &= -\frac{M_y}{T_2} \\ \frac{dM_z}{dt} &= -\frac{M_z - M_0}{T_1}, \end{aligned} \tag{5.2}$$

where T_1 and T_2 are the T_1 and T_2 relaxation time, respectively. Therefore, combining the Equation (5.1) and Equation (5.2), we can obtain

$$\frac{d\boldsymbol{M}}{dt} = \gamma \boldsymbol{M} \times \boldsymbol{B} - \frac{M_x \boldsymbol{e}_x + M_y \boldsymbol{e}_y}{T_2} + \frac{(M_0 - M_z)\boldsymbol{e}_z}{T_1}. \tag{5.3}$$

Here, $\boldsymbol{e} = (\boldsymbol{e_x}, \boldsymbol{e_y}, \boldsymbol{e_z})$ means the orientation vector in the laboratory frame.

Magnetic fields which are applied in MRI measurement are roughly divided into three types: main magnetic field, gradient magnetic field and RF magnetic field. The main magnetic field, which is strong, static and uniform, is applied along the z-axis with the amplitude of B_0. The gradient magnetic fields $\boldsymbol{\beta}$, which are applied for the purpose of image encoding, can be rewrite using a spatial gradient of magnetic field $\boldsymbol{G} = (G_x, G_y, G_z)$ and a position vector $\boldsymbol{r} = (x, y, z)$ as $\boldsymbol{\beta} = \boldsymbol{G} \cdot \boldsymbol{r}$. However, as the amplitude of $\boldsymbol{\beta}$ is small enough compared with that of the main magnetic field, the sum of $\boldsymbol{B_0}$ and $\boldsymbol{\beta}$ is aligned along z-axis, and therefore, it can be approximated as

$$\begin{aligned} \boldsymbol{B}_0 + \boldsymbol{\beta} &\simeq |\boldsymbol{B}_0 + \boldsymbol{\beta}| \boldsymbol{e}_z \\ &= (B_0 + \boldsymbol{G} \cdot \boldsymbol{r}) \boldsymbol{e}_z. \end{aligned} \tag{5.4}$$

The RF magnetic fields $\boldsymbol{B}_1$ are magnetic fields rotating at ω_{rot}, which is usually equal to the Larmor frequency of B_0 ($\omega_0 = \gamma B_0$), and they are applied so that magnetic field vector rotate in the x-y plane:

$$\boldsymbol{B}_1 = (b_x \cos \omega_{\mathrm{rot}} t + b_y \sin \omega_{\mathrm{rot}} t) \boldsymbol{e}_x + (-b_x \sin \omega_{\mathrm{rot}} t + b_y \cos \omega_{\mathrm{rot}} t) \boldsymbol{e}_y, \tag{5.5}$$

where b_x, b_y and t are the x and y component of the RF magnetic field and time, respectively.

Finally, we can describe the magnetic fields applied to the MR system as

$$\begin{aligned}\boldsymbol{B} = (b_x \cos\omega_{\rm rot} t + b_y \sin\omega_{\rm rot} t)\boldsymbol{e}_x + (-b_x \sin\omega_{\rm rot} t + b_y \cos\omega_{\rm rot} t)\boldsymbol{e}_y \\ +(B_0 + \boldsymbol{G}\cdot\boldsymbol{r})\boldsymbol{e}_z \end{aligned} \tag{5.6}$$

Next, we employ a viewpoint of a frame rotating at $\omega_{\rm rot}$ around the z-axis for simplicity. The relation between the unit vector of laboratory frame $\boldsymbol{e} = (\boldsymbol{e_x}, \boldsymbol{e_y}, \boldsymbol{e_z})$ and that of rotating frame $\boldsymbol{e'} = (\boldsymbol{e'_x}, \boldsymbol{e'_y}, \boldsymbol{e'_z})$ are

$$\begin{aligned} \boldsymbol{e'}_x &= \boldsymbol{e}_x \cos\omega_{\rm rot} t - \boldsymbol{e}_y \sin\omega_{\rm rot} t \\ \boldsymbol{e'}_y &= \boldsymbol{e}_x \sin\omega_{\rm rot} t + \boldsymbol{e}_y \cos\omega_{\rm rot} t \\ \boldsymbol{e'}_z &= \boldsymbol{e}_z. \end{aligned} \tag{5.7}$$

Using Equations (5.7), we can rewrite Equation (5.6):

$$\boldsymbol{B} = b_x\boldsymbol{e'} + b_y\boldsymbol{e'}_y + (B_0 + \boldsymbol{G}\cdot\boldsymbol{r})\boldsymbol{e'}_z. \tag{5.8}$$

Moreover, the net magnetization $\boldsymbol{M}$ can be rewrite as

$$\begin{aligned} \boldsymbol{M} &= M_x\boldsymbol{e} + M_y\boldsymbol{e}_y + M_z\boldsymbol{e}_z \\ &= M'_x\boldsymbol{e'} + M'_y\boldsymbol{e'}_y + M'_z\boldsymbol{e'}_z. \end{aligned} \tag{5.9}$$

Considering that $\boldsymbol{e'}_x$, $\boldsymbol{e'}_y$ and $\boldsymbol{e'}_z$ are time-dependent, we differentiate Equation (5.9) and we obtain

$$\begin{aligned} \frac{d\boldsymbol{M}}{dt} &= \frac{dM'_x}{dt}\boldsymbol{e'}_x + \frac{dM'_y}{dt}\boldsymbol{e'}_y + \frac{dM'_z}{dt}\boldsymbol{e'}_z + M'_x\frac{d\boldsymbol{e'}_x}{dt} + M'_y\frac{d\boldsymbol{e'}_y}{dt} + M'_z\frac{d\boldsymbol{e'}_z}{dt} \\ &= \left(\frac{dM'_x}{dt} + \omega_{\rm rot}M'_y\right)\boldsymbol{e'}_x + \left(\frac{dM'_y}{dt} - \omega_{\rm rot}M'_x\right)\boldsymbol{e'}_y + \frac{dM'_z}{dt}\boldsymbol{e'}_z. \end{aligned} \tag{5.10}$$

Here, if we assume that the RF magnetic fields are applied along x-axis and there is no gradient magnetic fields, we can fix b_x, b_y and $\boldsymbol{G}$ to B_1, 0 and 0, respectively:

$$\boldsymbol{B} = B_1\boldsymbol{e'}_x + B_0\boldsymbol{e'}_z. \tag{5.11}$$

We, therefore, rewrite the Equation (5.3) in the rotating frame by substituting Equations (5.9), (5.10) and (5.11) to Equation (5.3):

$$\begin{aligned} \frac{dM'_x}{dt} &= -\frac{M'_x}{T_2} + (\gamma B_0 - \omega_{\rm rot})M'_y \\ \frac{dM'_y}{dt} &= -(\gamma B_0 - \omega_{\rm rot})M'_x - \frac{M'_y}{T_2} + \gamma B_1 M'_z \\ \frac{dM'_z}{dt} &= -\gamma B_1 M'_y - \frac{M'_z - M_0}{T_1}. \end{aligned} \tag{5.12}$$

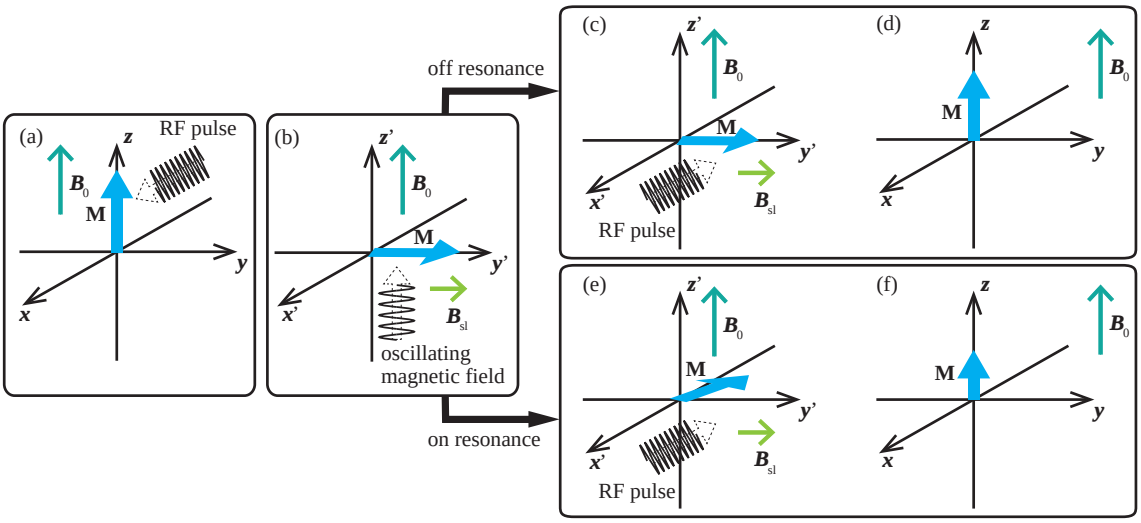

Figure 5.1: Externally applied oscillating magnetic fields decrease M_z because of secondary magnetic resonance. $(x,\ y,\ z)$ and $(x',\ y',\ z')$ are the coordinate of laboratory frame and singly rotating frame.

Furthermore, as we can define $\gamma B_0 = \omega_0$ and $\gamma B_1 = \omega_1$, we obtain

$$\begin{aligned} \frac{dM'_x}{dt} &= -\frac{M'_x}{T_2} + (\omega_0 - \omega_{\rm rot})M'_y \\ \frac{dM'_y}{dt} &= -(\omega_0 - \omega_{\rm rot})M'_x - \frac{M'_y}{T_2} + \omega_1 M'_z \\ \frac{dM'_z}{dt} &= -\omega_1 M'_y - \frac{M'_z - M_0}{T_1}. \end{aligned} \tag{5.13}$$

If we set $\omega_{\rm rot}$ to ω_0, we can diminish the influences of ω_0, that is B_0, and the magnetic resonance between the magnetization and the applied RF magnetic field occurs.

Now, we move to the spin-lock imaging sequence. As it is shown in Figure 2.24, there is three RF pulses in the spin-lock module. When the spin-lock imaging sequence runs, the first $\pi/2$ pulse flips the initial magnetization $\boldsymbol{M}$, which is aligned along the direction of the static magnetic field B_0 (the z-axis), into the transverse plane (the x-y plane), as shown in Figure 5.1 (a). After that, while the spin-lock pulse is applied along the y-axis, this flipped $\boldsymbol{M}$ is locked into the transverse plane by the spin-lock field $B_{\rm sl}$. Especially, on the viewpoint of the frame rotating at ω_0, which is the Larmor frequency of B_0, $\boldsymbol{M'}$ is locked into y'-axis. As a result, $B_{\rm sl}$ acts as a secondary main magnetic field like B_0 (Figure 5.1 (b)) in the rotating frame. If there is no externally applied magnetic field or there is an externally applied magnetic fields oscillating at off-resonant frequency of $B_{\rm sl}$ ($\omega_{\rm sl} = \gamma\ B_{\rm sl}$), it does not interact $\boldsymbol{M'}$ (Figure 5.1 (c)). In contrast, a magnetic field oscillating at $\omega_{\rm sl}$, it can be regarded as an excitation pulse for $\boldsymbol{M'}$ like the $\pi/2$ RF pule for $\boldsymbol{M}$ flipping $\boldsymbol{M'}$ (Figure 5.1 (e)) into the perpendicular plane of y' axis.

Accordingly, similar to the Equation (5.7), we introduce the viewpoint of doubly rotating frame, $\boldsymbol{e''} = (\boldsymbol{e''_x}, \boldsymbol{e''_y}, \boldsymbol{e''_z})$, rotating at ω, which is the frequency of oscillating magnetic field. In addition, we relabel the axes of doubly rotating frame (x'', y'', z) as x'' to y'', y'' to z'' and z'' to x'' to treat the $B_{\rm sl}$ applied along y'-axis as the main magnetic field which is usually applied along z-axis in the laboratory frame. Finally, we obtain the time-dependent Bloch equation about the performance of $\boldsymbol{M''}$ during the spin-lock pulse:

$$\begin{aligned}
\frac{dM''_x}{dt} &= -\frac{M''_x}{T_2^*} + (\omega_{\rm sl} - \omega)M''_y \\
\frac{dM''_y}{dt} &= -(\omega_{\rm sl} - \omega)M''_x - \frac{M''_y}{T_2^*} + \omega_{\rm m}M''_z \\
\frac{dM''_z}{dt} &= -\omega_{\rm m}M''_y - \frac{M''_z - M''_0}{T_{1\rho}},
\end{aligned} \tag{5.14}$$

where $\omega_{\rm m} = \gamma B_{\rm m}$. $B_{\rm m}$ and ω are the amplitude and frequency of the oscillating magnetic field, and $T_{1\rho}$ and T_2^* represent the $T_{1\rho}$ and T_2^* relaxation time, respectively. As well as Equation (5.13), the magnetic resonance between the magnetization and the externally applied oscillating magnetic field occurs; hereafter we call the magnetic resonance the secondary magnetic resonance.

After time $T_{\rm sl}$, the second $\pi/2$ pulse is applied and restores the magnetization $\boldsymbol{M}$ into the z-axis in the laboratory frame. Figure 5.1 (d) shows that the externally applied oscillating magnetic field does not affect final M_z, while Figure 5.1 (f) shows that the externally applied oscillating magnetic field decreases final M_z. Following application of the spin-lock module, a SE imaging sequence runs and generates MR signals; since M_z at the end of the spin-lock module is the initial value of $\boldsymbol{M}$ in the SE sequence, it affects the MR signals.

In conclusion, through the second magnetic resonance, an externally applied magnetic field oscillating at on-resonant frequency of $B_{\rm sl}$ decreases the MR signal. Based on this effect, by focusing on neural magnetic fields oscillating at specific frequencies—such as α and γ waves— it is possible to conduct fMRI studies with the spin-lock imaging sequence[31, 32].

5.2 Simulation algorism

The spin-lock imaging sequence (Figure 2.24) consists of a spin-lock module including a spin-lock pulse, which is a long-duration and low-power pulse, and is used to lock the spins in the transverse plane and a spin-echo sequence [58]. It provides images based on $T_{1\rho}$ relaxation, which is the spin-lattice relaxation time in the rotating frame [56].

We simulated the magnetization performance during the spin-lock module based on the time-dependent Bloch equation (Equation (5.14)) and the spin-lock imaging sequence

(Figure 2.24), which we stated in Subsection 5.1. The simulation started with the initial magnetization $\boldsymbol{M} = (M_x,\ M_y,\ M_z) = (0,\ 0,\ M_0)$, which is aligned along the direction of the static magnetic field $\boldsymbol{B}_0 = (0,\ 0,\ B_0)$. The first $\pi/2$ pulse is applied parallel to the x'-axis in the rotating frame. This flips the initial magnetization, which is aligned along the z-axis, into the transverse plane (the x-y plane). During the first $\pi/2$ pulse, we simulated the magnetization performance $\boldsymbol{M'} = (M'_x,\ M'_y,\ M'_z)$ based on Equation (5.13) on the rotating frame. In that equation we set ω_{rot} to ω_0 because we assumed using the $\pi/2$ RF pulse which was resonant with the protons for excitation. Thus, we obtained the equation below:

$$\begin{aligned} \frac{dM'_x}{dt} &= -\frac{M'_x}{T_2} \\ \frac{dM'_y}{dt} &= -\frac{M'_y}{T_2} + \omega_1 M'_z \\ \frac{dM'_z}{dt} &= -\omega_1 M'_y - \frac{M'_z - M_0}{T_1}. \end{aligned} \tag{5.15}$$

Next, if the spin-lock pulse, which is the RF pulse oscillating at ω_0, is applied parallel to the y'-axis, it can be expressed as magnetic fields $\boldsymbol{B}_{\mathrm{sl}} = (B_{\mathrm{sl}}\sin\omega_{0\mathrm{t}},\ B_{\mathrm{sl}}\sin\omega_{0\mathrm{t}},\ 0)$, where $\omega_0 = \gamma\, B_0$. In the frame rotating at ω_0, B_{sl} acts as a secondary B_0 field, and therefore, it locks the flipped $\boldsymbol{M}$ into the transverse plane (the x-y plane) by the viewpoint of the laboratory frame of reference and into the y'-axis by the viewpoint of rotating frame of reference. After simulating the magnetization performance during the $\pi/2$ pulse, we simulated the magnetization performance during the spin-lock pulse on the doubly rotating frame of reference. For convenience' sake, we relabeled the axes of rotating frame (x', y', z') as x' to y', y' to z', and z' to x', which indicated that we regard B_{sl} as the secondary B_0 and its direction was considered to be parallel to the z'-axis. Furthermore, we introduced the doubly rotating frame rotating at the same frequency ω as the oscillating magnetic field applied parallel to the x'-axis after relabeling of the axes. Fixing the magnetization $\boldsymbol{M''} = (M''_x,\ M''_y,\ M''_z)$ at the beginning of the spin-lock pulse to that $\boldsymbol{M'} = (M'_y,\ M'_z,\ M'_x)$ at the ending of the $\pi/2$ pulse, we solved the Equation (5.14).

After the spin-lock pulse, we relabeled the axes of doubly rotating frame (x'', y'', z'') as x'' to z', y'' to x'', and z'' to y'' and converted the magnetization $\boldsymbol{M''}$ in the doubly rotating frame of reference into the rotating frame of reference. We also calculated the magnetization performance $\boldsymbol{M'}$ in the rotating frame of reference during the the the second $\pi/2$ pulse based on the Equation (5.15).

For all the calculation, we solved the Bloch equation (Equations (5.14) and (5.15)) during the $\pi/2$ pulse and the spin-lock pulse, by means of a matrix operation proposed by Murase and Tanki [70]. To implement the matrix operation method, we transform

Equations (5.14) and (5.15) into a matrix form as:

$$\frac{d}{dt}\begin{pmatrix} M_x'' \\ M_y'' \\ M_z'' \\ 1 \end{pmatrix} = \begin{pmatrix} -R_2 & \Delta\omega & 0 & 0 \\ -\Delta\omega & -R_2 & \omega_{\mathrm{m}} & 0 \\ 0 & -\omega_{\mathrm{m}} & -R_{1\rho} & R_{1\rho}M_0 \\ 0 & 0 & 0 & 0 \end{pmatrix} \begin{pmatrix} M_x'' \\ M_y'' \\ M_z'' \\ 1 \end{pmatrix} \tag{5.16}$$

$$\frac{d}{dt}\begin{pmatrix} M_x' \\ M_y' \\ M_z' \\ 1 \end{pmatrix} = \begin{pmatrix} -R_2 & 0 & 0 & 0 \\ 0 & -R_2 & \omega_1 & 0 \\ 0 & -\omega_1 & -R_1 & R_1M_0 \\ 0 & 0 & 0 & 0 \end{pmatrix} \begin{pmatrix} M_x' \\ M_y' \\ M_z' \\ 1 \end{pmatrix}, \tag{5.17}$$

where R_1, $R_{1\rho}$ and R_2 indicate $1/T_1$, $1/T_{1\rho}$ and $1/T_2^*$, respectively. Here, if we put

$$\mathbf{A} = \begin{pmatrix} -R_2 & \Delta\omega & 0 & 0 \\ -\Delta\omega & -R_2 & \omega_{\mathrm{m}} & 0 \\ 0 & -\omega_{\mathrm{m}} & -R_{1\rho} & R_{1\rho}M_0 \\ 0 & 0 & 0 & 0 \end{pmatrix} \tag{5.18}$$

$$\mathbf{B} = \begin{pmatrix} -R_2 & 0 & 0 & 0 \\ 0 & -R_2 & \omega_1 & 0 \\ 0 & -\omega_1 & -R_1 & R_1M_0 \\ 0 & 0 & 0 & 0 \end{pmatrix}, \tag{5.19}$$

we can rewrite Equations (5.16) and (5.17) as:

$$\frac{d\boldsymbol{M''}}{dt} = \mathbf{A} \cdot \boldsymbol{M''} \tag{5.20}$$

$$\frac{d\boldsymbol{M'}}{dt} = \mathbf{B} \cdot \boldsymbol{M'}. \tag{5.21}$$

Therefore, we could obtain the solution $\boldsymbol{M''}(t)$ during the spin-lock pulse in the doubly rotating frame of reference and $\boldsymbol{M'}(t)$ during the $\pi/2$ pulse in the rotating frame of reference as:

$$\begin{aligned} \boldsymbol{M''}(t) &= \mathrm{e}^{\mathbf{A}t}\boldsymbol{M''}(0) \\ \mathrm{e}^{\mathbf{A}t} &= \mathbf{T}\mathrm{diag}\left(\mathrm{e}^{\lambda_1 t}, \mathrm{e}^{\lambda_2 t}, \mathrm{e}^{\lambda_3 t}, \mathrm{e}^{\lambda_4 t}\right)\mathbf{T^{-1}} \end{aligned} \tag{5.22}$$

$$\begin{aligned} \boldsymbol{M'}(t) &= \mathrm{e}^{\mathbf{B}t}\boldsymbol{M'}(0) \\ \mathrm{e}^{\mathbf{B}t} &= \mathbf{U}\mathrm{diag}\left(\mathrm{e}^{\mu_1 t}, \mathrm{e}^{\mu_2 t}, \mathrm{e}^{\mu_3 t}, \mathrm{e}^{\mu_4 t}\right)\mathbf{U^{-1}}, \end{aligned} \tag{5.23}$$

where $\mathbf{T}$ and $\mathbf{U}$ are the eigenvector of $\mathbf{A}$ and $\mathbf{B}$, respectively. In addition, λ_1, λ_2, λ_3 and λ_4 are the eigenvalues of $\mathbf{A}$, and μ_1, μ_2, μ_3 and μ_4 are those of $\mathbf{B}$, respectively.

Through the simulation, we finally obtained the time course of magnetization M_x, M_y and M_z on the laboratory frame of reference during the spin-lock module using this matrix operation method. The simulation provided the time course of magnetization in both case: with and without the secondary magnetic resonance occured. As well as the time course of M_x, M_y and M_z, we also obtained the M_z immediately after the spin-lock module to investigate the net influence of the secondary magnetic resonance on the magnetization. The normalized magnetization $\boldsymbol{M}$ (on) / $\boldsymbol{M}$ (off) immediately after the spin-lock module was calculated by both magnetization $\boldsymbol{M}$ (on) and$\boldsymbol{M}$ (off), which were obtained with and without externally applied on-resonant magnetic fields, respectively. Normalized magnetizations were expected to show the differences originating from the secondary magnetic resonance. Incidentally, we assumed that the traditional spin-echo ran after the spin-lock module. While the traditional spin-echo ran, there was no externally applied magnetic field expected, and therefore, there would be no differences between the magnetization that does and does not experience the externally applied magnetic fields during the spin-lock module. Therefore, the z component of the normalized magnetization M_z (on) / M_z (off) could be indexes to show the influences of the secondary magnetic resonance occurring between the spin-lock pulse and the externally applied magnetic fields oscillating at a certain frequency through the spin-lock imaging sequence.

5.3 Simulation parameters

Simulation studies based on the Bloch equation were implemented to visualize the performance of magnetization under the spin-lock module in the spin-lock imaging sequence. We obtained the time course of the magnetization with and without on-resonant oscillating magnetic fields, which were applied externally. It was also observed that the secondary magnetic resonance of the spin-lock pulse and the oscillating magnetic fields decreased the magnetization. In addition, the effect of the spin-lock time T_{sl} on decreases of MR signal intensities were investigated through the Bloch simulation.

5.3.1 Visualization of magnetization

Bloch simulation visualized the time-dependent performance of the magnetization during the spin-lock module. In this visualization, we used the following parameters for relaxation time: $T_1 = 1100$ ms, $T_{1\rho} = 100$ ms and $T_2^* = 75$ ms for modeling human brain gray matter scanned with a 1.5 T MR scanner [71, 72]. Moreover, we set the parameters of spin-lock pulse as: $B_{\mathrm{sl}} = 2.35$ μT ($\omega_{\mathrm{sl}} = 100$ Hz), $T_{\mathrm{sl}} = 40$ ms. The duration time of $\pi/2$ pulses were fixed to 2 ms and B_0 was set to 1.5×10^5 T to visualize the magnetization behavior clearly. We assumed externally applied magnetic fields with the amplitude of 50 nT (B_{m}) oscillating at 100 Hz (ω). The z component of the magnetization M_z with ω_{sl} and ω of 95

and 50 Hz were also observed to demonstrate the differences of the time course caused by the difference in the secondary magnetic resonant frequency. They were compared with those with ω_{sl} and ω of 100 Hz observed above.

5.3.2 Signal decrease by secondary magnetic resonance

After the visualization of the magnetization performance, we observed the secondary magnetic resonance via Bloch simulation. We obtained the magnetization after the spin-lock module with the spin-lock pulse at fixed amplitudes of B_{sl} of 1.17 and 2.35 μT, while changing the frequency ω of the oscillating magnetic fields. The simulation was carried out to demonstrate that the secondary magnetic resonance occurred when the amplitude of the spin-lock pulse and the frequency of the externally applied oscillating magnetic field satisfied the resonance condition. The Larmor frequencies ω_{sl} corresponding to these fixed amplitudes were 50 and 100 Hz, respectively. As for the relaxation times, we used the same values as Subsection 5.3.1; T_1, $T_{1\rho}$ and T_2^* were set to 1100, 100, and 75 ms, respectively. Additionally, we set B_{m} to 47 nT, and fixed T_{sl} at 100 ms. In actual measurements, the finally obtained MR signal only depends on the z component of the magnetization after the spin-lock module because spoiler RF pulses applied immediately after the spin-lock module to eliminate the x and y components of the magnetization. Therefore, the z component of the magnetization after the spin-lock module was considered to be the signal intensities, and we used the z component of the normalized magnetizations as the normalized signal intensities.

Furthermore, to investigate the amplitude of the externally applied magnetic fields B_{m}, we also obtained the magnetization after the spin-lock module with the spin-lock pulse of fixed parameters: B_{sl} of 0.235, 1.17 and 2.35 μT (ω_{sl} of 10, 50 and 100 Hz), and T_{sl} of 100 ms. As for the externally applied magnetic field, we employed the amplitude B_{m} of 0.5, 1.0 and 5.0 nT, while setting the frequency ω to the same value of ω_{sl}. We chose such small values for B_{m} to approximate neural magnetic fields.

5.3.3 Duration time dependence

Bloch simulations were also used for investigating a parameter of the spin-lock pulse—the influence of T_{sl}— on decreases in the magnetization during the secondary magnetic resonance. At the values of T_1, $T_{1\rho}$ and T_2^* used in the abovementioned simulations, we increased T_{sl} from 0 to 500 ms, while changing B_{m} to 0.5, 1.0, and 2.0 nT, which values are as small as neural magnetic fields. To simulate the secondary magnetic resonance, we set B_{sl} and ω to 2.35 μT (ω_{sl} of 100 Hz) and 100 Hz, respectively.

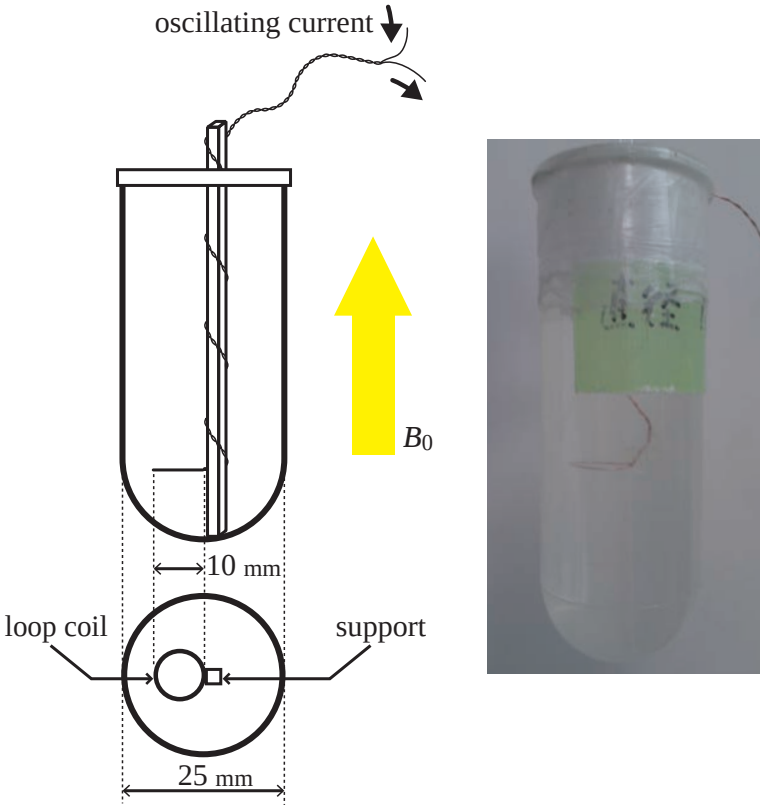

Figure 5.2: Phantom consisting of a single-loop coil. The loop was made of insulated copper wire 0.5 mm in diameter and located in a plastic tube filled with saline solution. The wire was twisted to cancel the magnetic fields generated by the wire except for the loop.

5.4 Phantom

Imaging condition

To verify our simulations, we observed the signal decrease originating from the secondary magnetic resonance through phantom studies. In the phantom studies, we measured the phantom, which consisted of a single-loop coil made of insulated copper wire, 0.5 mm in diameter, and a cylindrical plastic tube as shown in Figure 5.2. The phantom was filled with a solution of saline (0.9% NaCl) in which 0.25 ml of Gadopentetate dimeglumine (Magnevist, Berlex Laboratories) was mixed, yielding $T_1 = 1100$ ms measured by inversion recovery. The diameter of the loop was 10 mm, which was located perpendicular to the B_0 field. It was fixed to a plastic support not to move during measurements. The loop was connected to a function generator (AFG3000, Tektronix), which used a gating pulse controlled by the MR pulse sequence to apply magnetic fields only during the spin-lock pulse of the sequence. In addition, a 2 kΩ resistor was inserted into the circuit. The wire was twisted to cancel the magnetic fields generated by the wire except for the loop.

Figure 5.3: Quadrature coil where phantom was placed. It was set inside the bore of the MR scanner.

5.5 Imaging condition

Spin-lock imaging was implemented with a 7 T MR scanner (Bruker, BioSpin), which is shown in Figure 3.6. The quadrature coil was set in the bore of the scanner and the phantom was placed in it as shown in Figure 5.3. We selected this scanner for the phantom studies because it enabled us to rewrite the pulse sequence easily and obtain a high SNR. We wrote the spin-lock imaging sequence by adding the pulses for the spin-lock module — $\pi/2$ pulse along the x direction, spin-lock pulse along the y' direction and $\pi/2$ pulse along the -x direction— to the conventional spin-echo sequence, and therefore, the conventional spin-echo sequence preceded by the spin-lock module shown in Figure 2.24 was used for this experiment. In all the experiment, we acquired MR images without externally applied magnetic fields for the reference and calculated the normalized signal intensities. The amplitude of voltage applied to the wire loop was controlled by the function generator located outside the shielded MRI room.

5.5.1 Signal decrease by secondary magnetic resonance

Images were acquired to show that the secondary magnetic resonance decreased the normalized signal intensities. We employed the two frequencies, 50 and 100 Hz, for the secondary magnetic resonance. The parameters for spin-lock pulse was employed as follows : T_{sl} was set to 100 ms, and B_{sl} was set to 1.17 and 2.35 μT (ω_{sl} of 50 and 100 Hz). During the spin-lock pulse, the function generator produced an alternating current to generate oscillating magnetic fields around the loop. The amplitude of the current was set to 750 μA, generating B_{m} of 47 nT at the center of the loop. To enable observation of the signal decrease when the secondary magnetic resonance occurred, ω was set to 0–100

and 50–150 Hz, while ω_{sl} was set to 50 and 100 Hz, respectively. An axial image was acquired in every shot and its position was carefully determined to include the wire loop in the image based on localization images. The geometrical parameters of the images were set as follows: a matrix of 64 × 64, a field of view (FOV) of 40 mm × 40 mm, a slice thickness of 2 mm and a slice interval of 2 mm. These indicated that the voxel size was 0.625 mm × 0.625 mm × 2 mm. Additional parameters was determined: echo time (TE) of 14 ms and repetition time (TR) of 1 s.

5.5.2 Detection of minute magnetic fields

A further phantom study was carried out to detect small magnetic fields of the order of sub-nT with this method. For the actual fMRI study with NMFD method, we expect the sensitivity for magnetic field of sub-nT to detect neural magnetic fields in human brain. Three values were chosen: 314, 157, and 31.4 pT at the center of the loop while considering actual magnetic fields in the human brain [24, 27, 31, 32]. The frequency of targeted magnetic fields was adjusted to obtain a maximum signal decrease based on the phantom study in Subsection 5.5.1. Regarding the spin-lock pulse, T_{sl} and B_{sl} were fixed to 200 ms and 2.35 μT, respectively. T_{sl} was set longer than that used in Subsection 5.5.1 expecting that the MR signal intensities would decrease larger than those with T_{sl} of 100 mT. Other imaging parameters were set to the same values as those used for the phantom study mentioned above in Subsection 5.5.1. Moreover, the acquisition of images was repeated for 10 times for the improvement of SNR and the statistical analysis. We alternately obtained MR images with and without externally applied magnetic fields around the wire loop which was oscillating at on-resonant frequency with the spin-lock pulse.

5.6 Results for simulation

5.6.1 Visualization of magnetization

Figures 5.4 (a) and (b) showed the magnetization performances during the spin-lock module with and without externally applied magnetic fields oscillating at on-resonant frequency of B_{sl}, respectively. In the case without resonance, magnetization (M_x, M_y, M_z) commenced at (0, 0, 1) and was then flipped into the x-y plane, as shown in Figure 5.4 (a). After being locked in the x-y plane with the spin-lock pulse, the magnetization returned to the z-axis with the second $\pi/2$ pulse. The decrease of final M_z was caused solely by $T_{1\rho}$ relaxation (Figure5.4 (a-3)). Figures 5.4 (a-1) and (a-2) showed that the magnetization was rotating in the x-y plane during the spin-lock pulse. In contrast, in the case with resonance, the magnetization oscillated three-dimensionally, as shown in

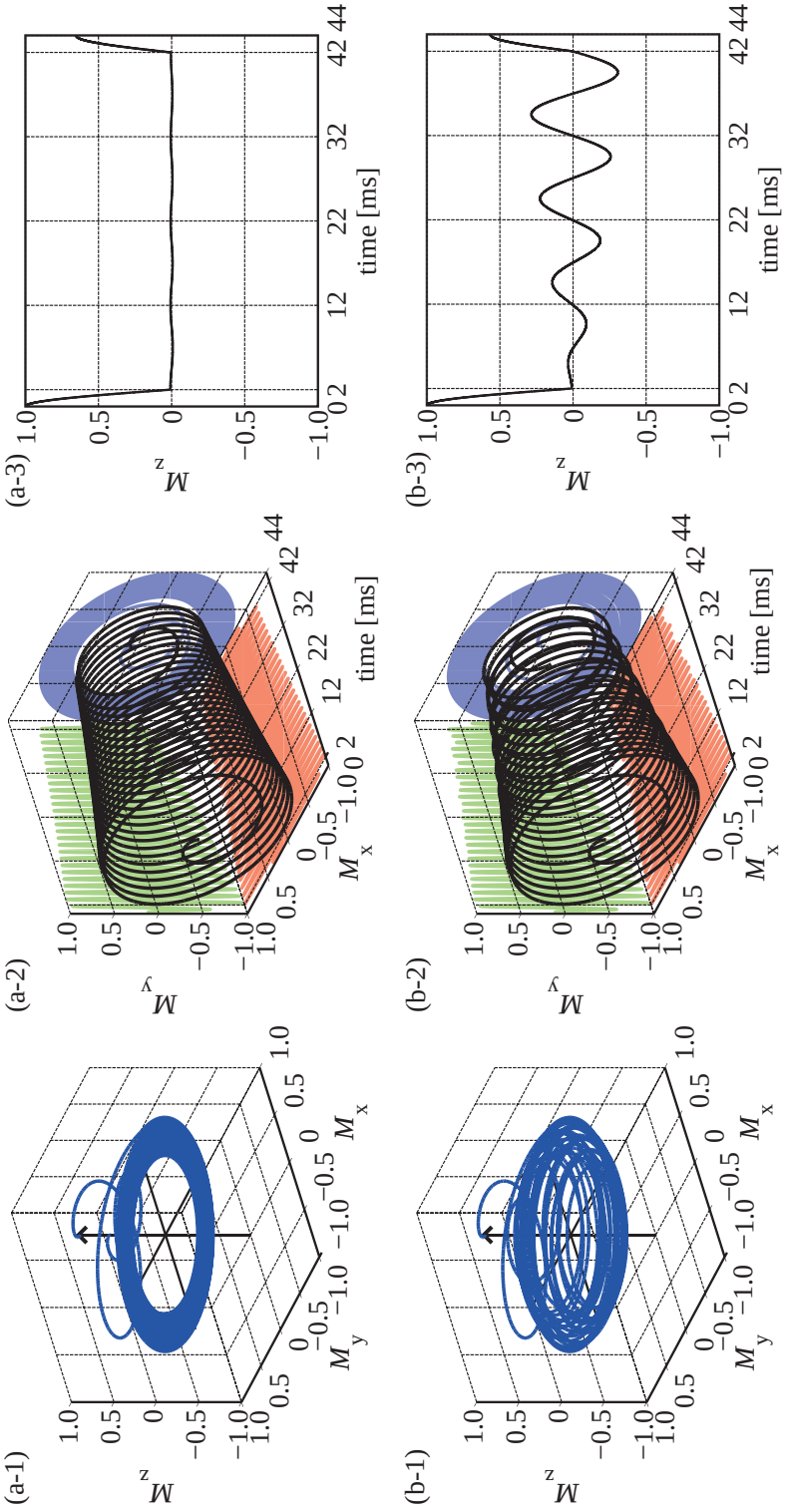

Figure 5.4: Magnetization performance during spin-lock module without on-resonant oscillating magnetic field applied (a-1). Time courses of M_x and M_y (a-2). Time course of M_z (a-3). Magnetization performance during spin-lock module with on-resonant oscillating magnetic field applied (b-1). Time course of M_x and M_y (b-2). Time course of M_z (b-3).

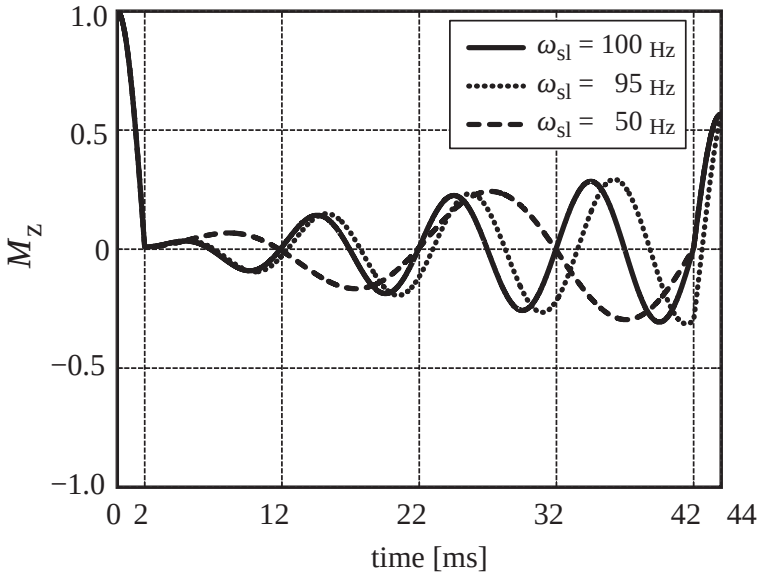

Figure 5.5: Time course of M_z. Resonant frequencies were 100, 95, and 50 Hz.

Figure 5.4 (b-1), because the magnetic field oscillating at the Larmor frequency of the spin-lock pulse flipped it into the plane perpendicular to the spin-lock direction, acting like an excitation pulse in the doubly rotating frame of reference. Consequently, the M_z finally decreased more than that without resonance.

Figure 5.5 showed the time courses of M_z using the spin-lock pulse the amplitude of which was set to provide ω_{sl} of 100, 95, and 50 Hz. In every case, ω was set to the same value as ω_{sl} to satisfy the on-resonant condition. Although the cycle of each M_z differed, M_z exhibited the same value at the end of the spin-lock module. These results suggest that the decreases in M_z caused by the secondary magnetic resonance are independent of the on-resonant frequencies of spin-lock pulse and oscillating magnetic fields.

5.6.2 Signal decrease by secondary magnetic resonance

Figure 5.6 showed the ω dependence of the normalized magnetization M_z (on) / M_z (off). We could observe decreases in M_z (on) / M_z (off) when the applied magnetic field was oscillating at a Larmor frequency of B_{sl}, namely, $\omega = \omega_{\mathrm{sl}}$. Here, M_z (on) and M_z (off) are the z component of the magnetization with and without externally applied on-resonant oscillating magnetic fields, respectively. Decreases in M_z (on) / M_z (off) originated from the secondary magnetic resonance were observed in both cases: ω_{sl} of 50 and 100 Hz. The results also illustrated the same magnitude of decreases in M_z (on) / M_z (off) in both case with the resonant frequency of 50 and 100 Hz, and therefore, we can suggest that the frequency of resonant condition does not affect the magnitudes of decreases in M_z (on) /

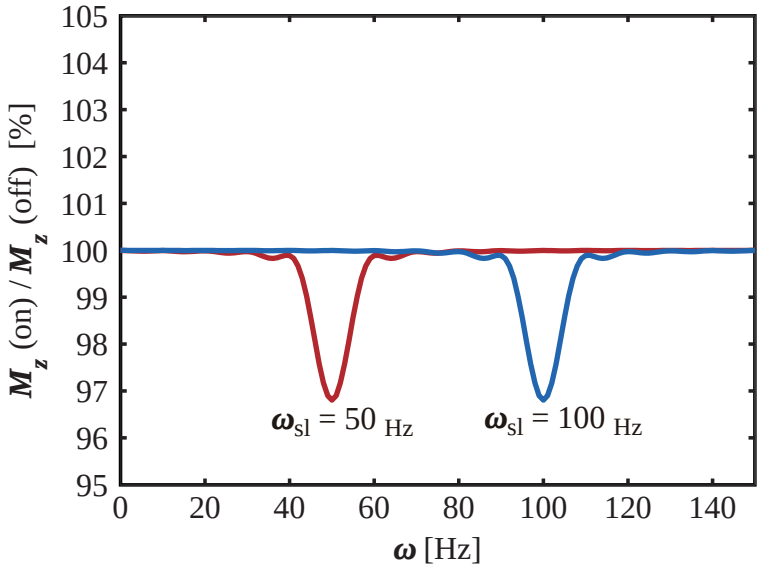

Figure 5.6: Normalized magnetization M_z (on) / M_z (off) with ω_{sl} of 50 and 100 Hz while changing ω.

M_z (off).

Figure 5.7 showed that the normalized magnetization M_z (on) / M_z (off) decreased due to the secondary magnetic resonance as Figure 5.6. Figure 5.7 (a) and (b) illustrated the results with B_{m} of 0.5 and 1.0 nT and 5.0 nT, respectively. It is obvious from these figures that larger values of B_{m} correspond to larger decreases in the M_z (on) / M_z (off); this can be explained as an effect of the increase in the amplitude of rotation of the magnetization during the spin-lock pulse with increasing B_{m}. However, the magnitude of decreases in M_z (on) / M_z (off) were much smaller than those with B_{m} of 47 nT in Figure 5.6, as is evident from the differences in the magnitudes of B_{m}. The fact indicates difficulties for detecting small magnetic fields with amplitudes of 0.1–1.0 nT.

5.6.3 Duration time dependence

Influences of T_{sl} on the decreases of magnetization during the secondary magnetic resonance were observed (Figure 5.8). M_z (on) / M_z (off) meant the same as that shown in Figure 5.6. These results of this assessment show that the decreases in M_z (on) / M_z (off) are larger at larger values of T_{sl}; this may be because the magnetization during the spin-lock pulse is rotated in proportion to the duration of T_{sl}. Thus, a longer T_{sl} causes a longer amplitude of rotation of the magnetization during the spin-lock pulse, and we can finally obtain larger decreases in M_z (on) / M_z (off). The cause of T_{sl} dependence of M_z (on) / M_z (off) is likely to be based on the same principle as that of B_{m} dependence of M_z (on) / M_z (off). Moreover, we obtained consistent results that M_z (on) / M_z (off)

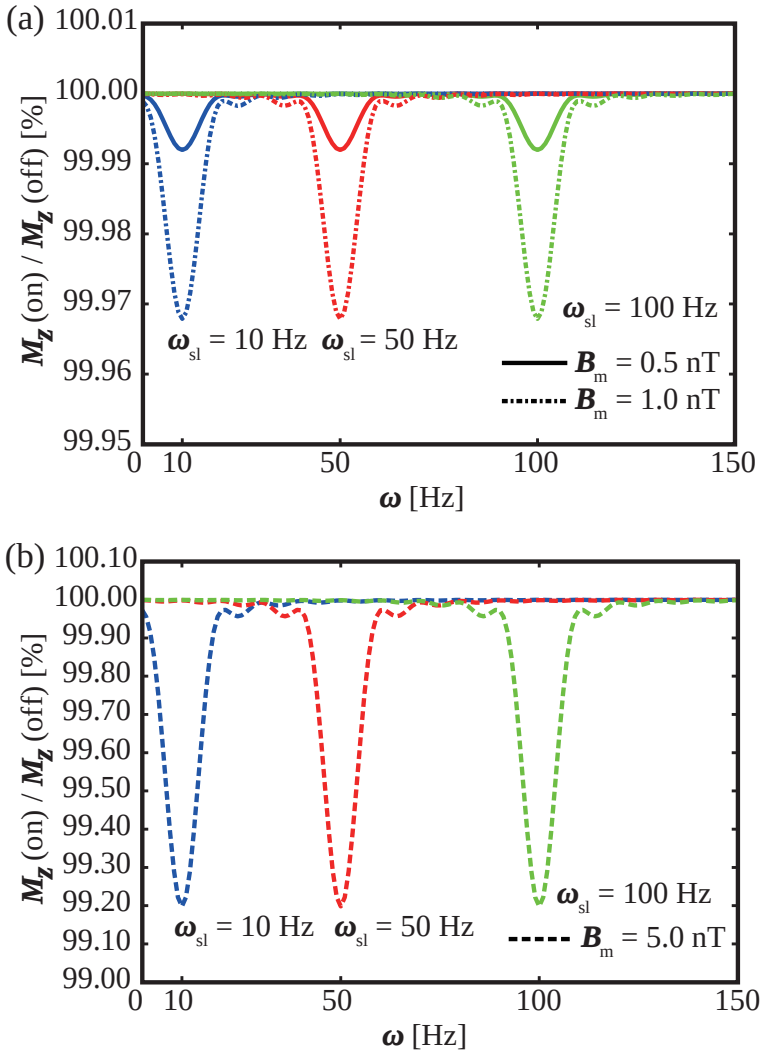

Figure 5.7: Normalized magnetization M_z (on) / M_z (off) originated from secondary magnetic resonance with B_m of 0.5 and 1.0 nT (a), and 5.0 nT (b).

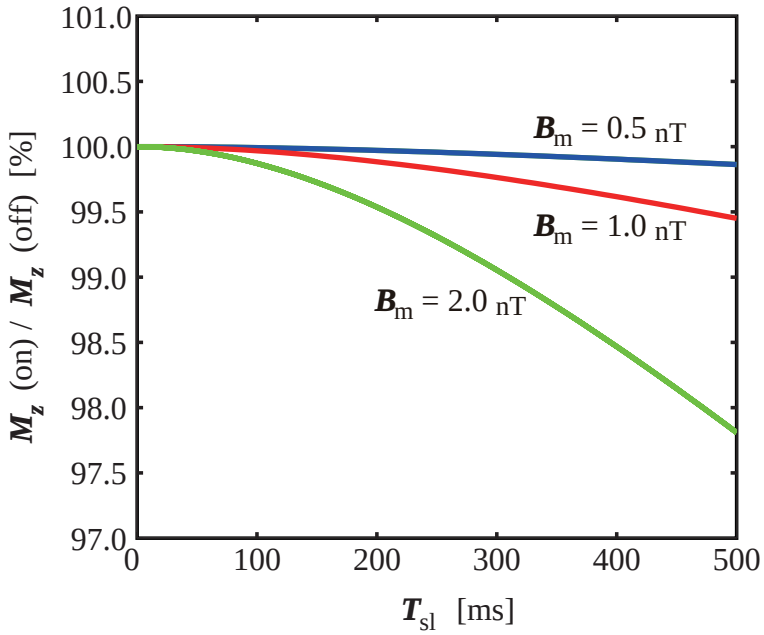

Figure 5.8: Normalized magnetization M_z (on) / M_z (off) with B_m of 0.5, 1.0, and 2.0 nT while changing T_{sl}.

with B_m of larger values provided larger decreases with those in Figure 5.7.

5.7 Results for phantom study

5.7.1 Signal decrease by secondary magnetic resonance

We showed MR images in Figure 5.9 of the loop phantom collected to observe signal decrease caused by secondary magnetic resonance. All of the images are axial slices including the wire loop. Through the acquisitions ω_{sl} was set to 50 (a) and 100 (b). While ω_{sl} was set to 50, the image with the on-resonant (ω of 46 Hz) oscillating magnetic field applied externally showed decrease in signal intensities (a-2) compared to that without the magnetic fields (a-1). There was no decrease in signal intensities in the image with the off-resonant (ω of 20 Hz) oscillating magnetic field (a-3). Similarly, the image with ω of 92 Hz showed decrease in signal intensities (b-2) because of the secondary magnetic resonance while ω_{sl} was set to 100 Hz. There was also no decrease in signal intensities in the images with the magnetic field oscillating at 70 Hz because the secondary magnetic resonance did not occur.

As Figure 5.11 showed, the normalized signal intensities S (on) / S (off) of measurements (solid lines) decreased when the applied magnetic field was oscillating at resonant frequency, as indicated in the simulation results. Here, S (on) and S (off) were signal

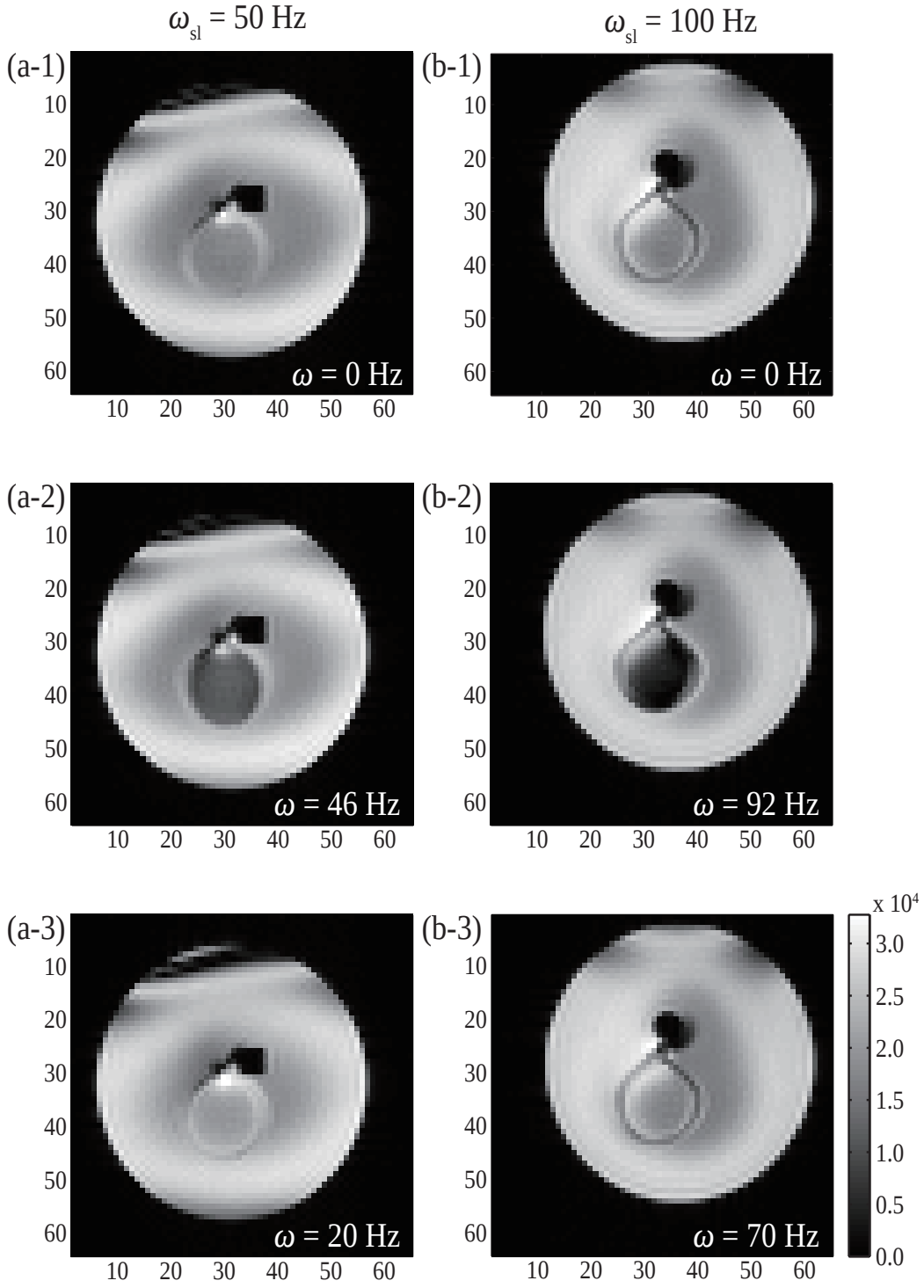

Figure 5.9: MR images of loop phantom. All images are axial slices including the wire loop. Through the acquisitions ω_{sl} was set to 50 (a) and 100 (b). Images without magnetic fields (a-1) and (b-1). Images with on-resonant magnetic fields oscillating at ω of 46 Hz (a-2) and ω of 92 Hz (b-2) Images with off-resonant magnetic fields oscillating at ω of 20 Hz (a-3) and 70 Hz (b-3). Only the images with on-resonant oscillating magnetic fields showed decreases in signal intensities.

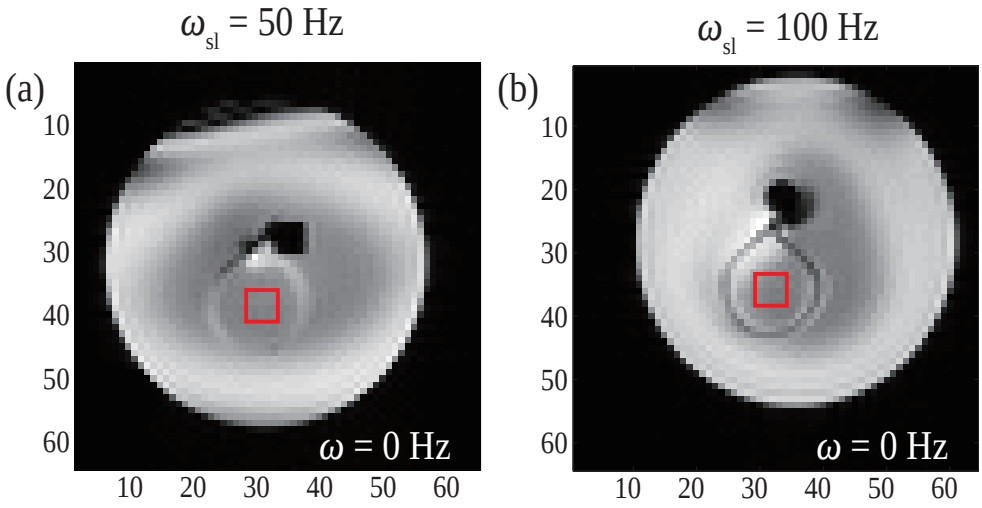

Figure 5.10: Pixels used for calculation of normalized signal intensities with ω_{sl} of 50 and 100 Hz. We divided the image data obtained with externally applied oscillating magnetic fields by those without the magnetic field ($\omega = 0$ Hz). We acquired the average of pixels surrounded by a red line.

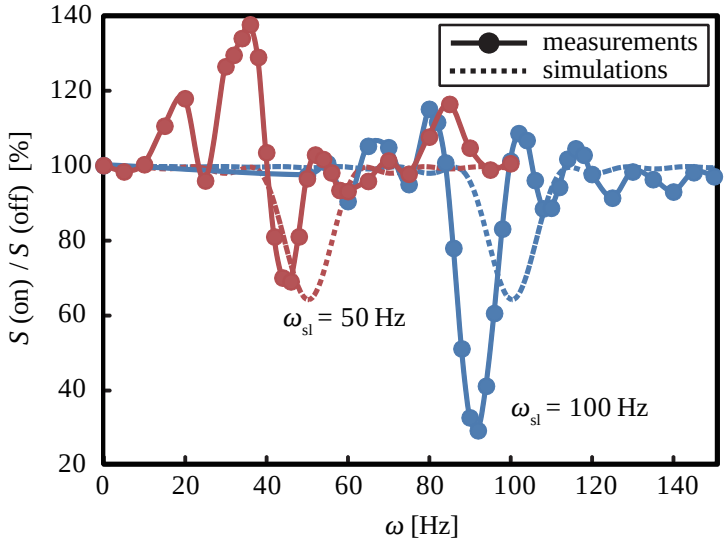

Figure 5.11: Normalized signal intensities S (on) / S (off) with ω_{sl} of 50 and 100 Hz while changing ω.

intensities with and without externally applied oscillating magnetic fields, respectively. These were averages of signal intensities in the region of interest (ROI) of 5 × 5 pixels at the center of the loop coil in the MR images. The ROI of MR images with ω_{sl} of 50 and 100 Hz was shown in Figures 5.10 (a) and (b), respectively. As well as the normalized signal intensities, the normalized magnetizations M (on) / M (off), which were provided by simulations, were shown in Figure 5.11 (broken lines). The same tendencies were observed from simulations and phantom studies. However, the phantom studies showed approximately 40% and 70% decreases of normalized signal intensities at most with ω_{sl} of 50 and 100 Hz, respectively, and simulations showed approximately 40% decreases of normalized magnetization at most with ω_{sl} of 50 and 100 Hz. This difference is considered to have been caused by the difference between the observations of M_z (on) / M_z (off) in simulations and S (on) / S (off) in measurements. Although the signal intensities observed in measurements were proportional to M_z at the end of the spin-lock module, they were influenced by the spin-echo sequence after the spin-lock module. Moreover, the ω that decreased S (on) / S (off) the most was a few Hz lower than ω_{sl} for some reason. Magnetic fields oscillating at ω of 41 and 92 Hz decreased S (on) / S (off) the most when ω_{sl} was 50 and 100 Hz, respectively.

5.7.2 Detection of minute magnetic fields

Influences of magnetic fields of the order of sub-nT on MR signal intensities were observed through the phantom studies. Taking into account the results obtained from Figure 5.11, a magnetic field oscillating at 92 Hz was chosen as the on-resonant oscillating magnetic field with which the largest signal decrease was expected. Ten MR images were obtained in each case: with and without on-resonant oscillating magnetic fields. Figures 5.12 (a-1), (b-1), and (c-1) showed the results of two-sided t-tested MR images and the pixels (yellow), which showed significant differences ($p > 0.05$) between normalized signal intensities with and without on-resonant oscillating magnetic fields. Figures 5.12 (a-2), (b-2), and (c-2) showed the percent signal differences between MR images with and without on-resonant oscillating magnetic fields. Here, B_{m} was 314.0 (a), 157.0 (b), and 31.4 (c) pT at the center of the loop. These results demonstrate that acquiring images 10 times enabled us to detect magnetic fields of the order of sub-nT as shown in Figures 5.12 (a) or (b).

5.8 Discussion

Several previous studies have attempted to detect neural magnetic fields using MRI, cell cultures, and theoretical calculations [23, 24, 25, 26, 27, 28, 29, 30]. Most of these have approached the problem by attempting to observe changes in magnitude or phase images; however, this strategy has disadvantages of cancellation effects caused by spatially

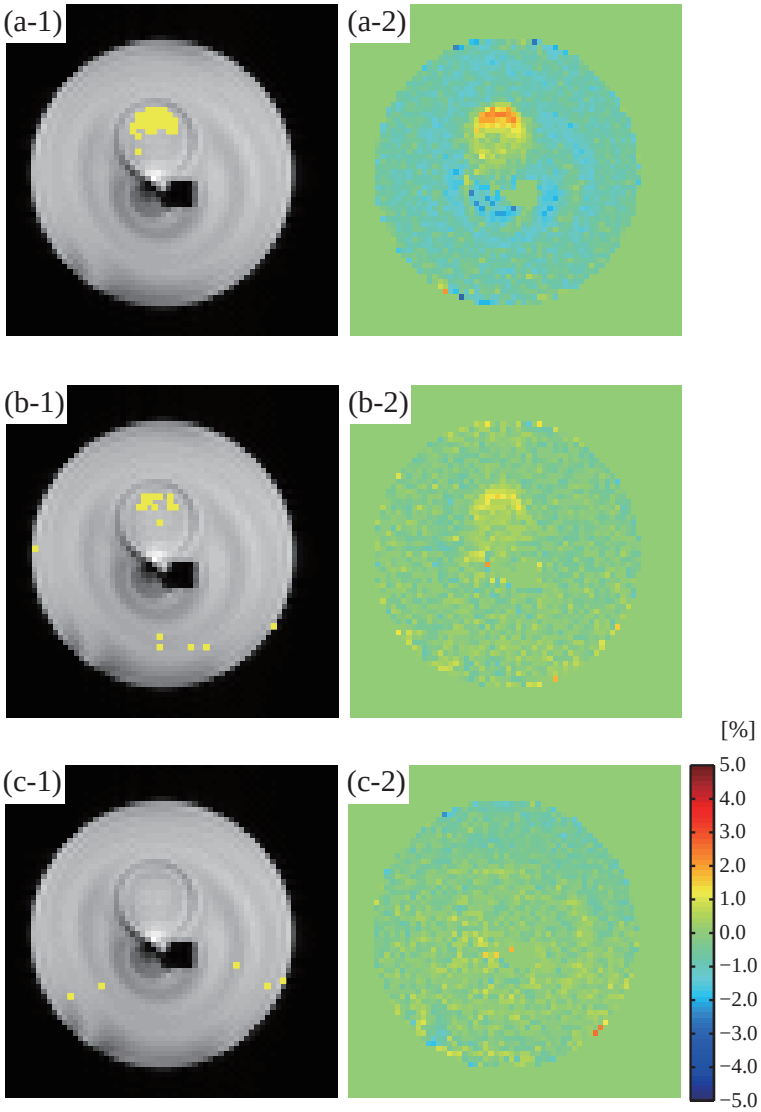

Figure 5.12: (Left column) MR images with pixels indicating significant differences. (Right column) Percent signal differences between MR images with and without on-resonant oscillating magnetic fields. Amplitude of oscillating magnetic fields B_{m} were 314.0 (a), 157.0 (b) and 31.4 (c) pT.

disordered structures, oscillation with a mean phase change of zero, incoherent signals, and the location of the current source within the given image voxel [25, 31, 32].

In contrast to this approach, spin-lock imaging potentially detects such signals without cancellations in the magnitude or phase images; it can provide $T_{1\rho}$-weighted images, which have previously been achieved in biomedical imaging [56, 73], and has the advantage of allowing band-selective variants of experiments such as those shown in Figures 5.6, 5.7 and 5.11. Spin-lock imaging would be of great use in measuring biological sources with multiple consistent frequencies [32]. Witzel et al. and Halpern-Manners et al. proposed the fMRI approach of using the spin-lock imaging sequence based on the secondary magnetic resonance [31, 32]. However, neither research group has explained the mechanism of the secondary magnetic resonance in detail. Moreover, the mechanism of fMRI method using spin-lock imaging sequence is controversial because the results of the fMRI method may be contributed by another component as stated in the study by Jin and Kim [74]. Therefore, in our study we visualized the phenomenon with numerical Bloch simulations to help understand this approach and investigated how we can observe contributions of externally applied magnetic fields to MR images.

To use spin-lock imaging for fMRI, it must be sufficiently sensitive to neural magnetic fields. Although the possibility of detecting such fields is still a matter of debate, some studies have reported measuring magnetic fields of the order of sub-nT with various methods [24, 27, 31, 32]. MEG measurements suggest that evoked or spontaneously synchronized activities in the 50,000 or more cortical neurons occupying an area of 1 or a few mm^2 result in magnetic fields of the order of 0.1–1 pT at a distance of 2–4 cm from the neuronal source. By contrast, MRI focusing on voxels 2–4 mm from the site of activation equates to fields of the order of 0.1–1 nT (based on an inverse-square distance scale $(r_{\mathrm{MEG}}/r_{\mathrm{MRI}})^2$) [27]. It is thus essential to be able to detect magnetic fields of 0.1–1 nT in order to measure brain activation with MRI.

In this regard, we used oscillating magnetic fields with B_{m} of 0.5, 1.0, and 2.0 nT to detect T_{sl} dependence of M_z (on)/M_z (off) in the Bloch simulation. Employing a longer T_{sl} decreases M_z (on)/M_z (off) to a greater extent, and longer T_{sl} is therefore preferable for observing minute magnetic fields with this method. However, the magnetization decrease is less than 1% when B_{m} is 0.5 and 1.0 nT, even when we use the longest T_{sl} of 500 ms. This implies that for the fMRI experiments, improvement of the SNR is necessary, i.e., by increasing the number of measurement repetitions or reducing the noises. Moreover, in attempts to avoid other possible problems of BOLD contamination and susceptibility artifacts, ultra-low-field (ULF) MRI has been attracting attention because ULF-MRI virtually cancels these out [51, 52].

There is another parameter of the spin-lock pulse B_{sl}: B_{sl} affects $T_{1\rho}$ [56, 71]. As well as T_1 and T_2^*, $T_{1\rho}$ depends on the magnitude of the static magnetic field B_0, the properties

of tissues, and the amplitude of the applied spin-lock pulse (this phenomenon is called $T_{1\rho}$ dispersion) [56]. As a result, measurements of $T_{1\rho}$ based on specific imaging conditions will be required during simulation. In the phantom study, we observed decreases in intensities of MR signals originating from the secondary magnetic resonance using magnetic fields oscillating at on-resonant frequencies. However, as shown in Figure 5.11, there were differences of a few Hz between ω_{sl} and ω that decreased the MR signal intensities the most, and ω_{sl} values were thought to be a few Hz lower than we expected. This may indicate that B_{sl} values were a little smaller than the values fixed on the console, which is considered to have been caused by the deterioration of an RF coil. Therefore, RF coils which are able to output magnetic fields with the correct amplitude are needed.

We also achieved the detection of small magnetic fields of the order of sub-nT, such as neural magnetic fields. MR images with B_{m} of 314.0 and 157.0 pT at the center of the loop showed signal changes between those with and without on-resonant oscillating magnetic fields. In the case of B_{m} of 314.0 pT, as shown in Figure 5.12 (a-1), some pixels were observed inside the loop that indicate significant differences between MR images with and without on-resonant oscillating magnetic fields. As shown in Figure 5.12 (a-2), 1.21% signal changes were observed approximately 2.5 mm from the wire of the loop. The amplitude of the magnetization at the pixel given by the Biot-Savart law was 330.4 pT. In addition, as shown in Figures 5.12 (b-1) and (b-2), 1.49% signal changes were observed approximately 1.25 mm from the wire inside the loop. There, the amplitude of the magnetization was 198.6 pT. Halpern-Manners et al. reported observing MR images of a single loop at very low driving voltages with estimated field strengths at the center of the loop of 0.92 and 0.46 nT [32]. Furthermore, Witzel et al. reported that a 7 min block design experiment was sensitive to a current dipole that produced an approximate magnetic field of 1 nT at a distance of 1.5 mm from the dipole [31]. SNR of our results calculated from the average signal and the rms noise in the ROI of acquired MR images without oscillating magnetic fields was 14.9 (ω_{sl} of 50 Hz) and 30.1 (ω_{sl} of 100 Hz). The SNR may be much higher than that of the study by Witzel et al. [31] because of the differences in B_0. Moreover, compared with the study by Halpern-Manners et al. [32] (2.0 and 2.5), SNR in the present study was much better probably because we employed larger voxel sizes. Therefore, higher SNR in our study may enable us to detect magnetic fields with much lower amplitude than those in previous studies.

Chapter 6

Discussion

In this dissertation, we discussed two fMRI methods based on non-hemodynamic phenomenon: DW-fMRI and NMFD-fMRI. DW-fMRI is based on DWI techniques and observes neural activities through restricted diffusion of water molecules around neural cells. NMFD-fMRI provides a more direct fMRI method to detect neural activities by imaging neural magnetic fields. We suggested mechanisms of these two emerging fMRI methods and demonstrated those feasibility by simulation studies and phantom studies with 7 T MRI. New fMRI methods that do not depend on hemodynamic changes are desired to make up for disadvantages of conventional BOLD-fMRI: indirectness and limitation to spatial and temporal resolutions. Therefore, mechanisms and characteristics of parameters of DW-fMRI and NMFD-fMRI obtained in this dissertation are helpful for the future investigation of these two fMRI approaches.

In Chapter 1, we have explained the importance of measuring the human brain function and increasing expectations for development of fMRI techniques in the field of research. Additionally, we mentioned the situation of previous works related to fMRI studies to design the contents in this dissertation and stated objectives of this study.

Chapter 2 has presented the background knowledge about the principles of MR techniques, fundamental information of the conventional fMRI approach including image processing and statistical analysis. In addition, we explained the technical principles of imaging methods related to MRI which we employed for the newly proposed fMRI: DW-fMRI and NMFD-fMRI.

First of all, we have explained the fundamental features of MRI, which is used for fMRI measurement, in particular, how to obtain contrasts of structures in the human brain and how to construct MR images with various pulse sequences. We also mentioned the important aspects of the conventional fMRI technique, which is based on BOLD contrast, to show how the map of brain functions is obtained by fMRI measurements. After the technical principles of MRI and fMRI, we have described imaging techniques related to the newly proposed fMRI approaches. DWI techniques present motion of water

molecules around neural cells and have been established their efficiency in the fMRI measurement. Although it has not been established, MRI measurement with the spin-lock imaging sequence has been attracted attentions to be used for fMRI measurement which detects neural magnetic fields directly; therefore, we summarized advantages and problems for achievement of this fMRI approach.

Chapter 3 demonstrated the importance of choosing parameters for achieving fMRI measurement with a DWI technique. We investigated influences of MPG parameters on signal intensities by the Monte Carlo simulation of movements of water molecules diffusing within restricted structures to find appropriate MPG parameters for brain mapping. The simulation results demonstrated that normalized signal intensities of DWI are considerably depend on MPG parameters, namely, the b- and q-values. In addition, we also demonstrated that differences between the normalized signal intensities before and after cell swelling are greatly affected by the b- and q-values. Furthermore, it was confirmed that the b- and the q-values that maximize the differences of normalized signal intensities could be estimated by the simulations. Finally, in the actual DWI experiments, the effects of noises and artifacts hampered the distinction of differences between normalized signal intensities. In order to resolve these problems, further studies are needed, including phantom experiments or actual measurements of brain functions.

Furthermore, we extended the simulation model employed in Chapter 3 to investigate how and why DWI signal intensities change after cell swelling in DW-fMRI measurements in Chapter 4. We also used the Monte Carlo method to calculate the differences between the normalized signal intensities before and after cell swelling by simulating the diffusion of water molecules within restricted structures. In this simulation, we employed a 3D simulation model with two compartments, respectively representing the intracellular and the extracellular regions, in order to distinguish the contributions of these two regions. Our simulation results using this model showed that the DWI signal intensities increase after cell swelling. These results could be interpreted because of the increasing ratio of the intracellular volume, which has a smaller diffusion coefficient and larger DWI signal intensities. Moreover, in this chapter we focused on Δ instead of q-value as a parameter to investigate, and the simulation results indicated the dependences of important DWI parameters—Δ as well as b-value— on the percent signal changes after cell swelling. These results should be helpful for DW-fMRI experiments.

Compared with DW-fMRI stated in chapter 3 and 4, which is based on the mechanism that changes in water diffusion affect changes in MR signal intensities, a MRI technique detecting neural magnetic fields directly has emerged as a more powerful fMRI. In Chapter 5, we mentioned NMFD-fMRI, which employs the spin-lock imaging sequence, as one of the fMRI techniques detecting neural magnetic fields directly. We described our results of visualizing magnetization behavior based on Bloch simulation to aid understanding

of the mechanism of the secondary magnetic resonance during a spin-lock module. We also demonstrated that the secondary magnetic resonance causes externally applied on-resonant oscillating magnetic fields to decrease noticeably the value of M_z, leading to decrease in MR signal intensities. The results of phantom studies support these findings. Moreover, in the phantom studies, we demonstrated that a longer duration of the spin-lock pulse is preferable for emphasizing the magnetization that leads intensities of MR signals decrease. We therefore selected the duration of 200 ms, which is longer than that used in previous studies [31, 32], but sufficiently short for practical use, and carried out MR image acquisitions 10 times so as to detect magnetic fields of the order of sub-nT. Consequently, we were able to detect magnetic fields of 198.6 pT originated from the single-loop coil. However, for realistic fMRI measurements of the human brain, some aspects could be improved, e.g., avoiding contamination of BOLD signals and shortening the acquisition time. To solve these problems, we would like to focus on employing ULF-MRIs or imaging methods that take into account the differences in timescale between the origination of neural magnetic fields and the BOLD effect.

Chapter 7

Conclusion

The main issue of this dissertation was to study fMRI with higher spatial and temporal resolutions. As described in Chapter 1, use of fMRI is spreading more and more widely. For example fMRI is the most popular noninvasive technique in the field of neuroscience to investigate higher brain functions. As well as for obtaining knowledges of brain functions, it is used for diagnosing or treating psychiatric disorders, e.g. Alzheimer's disease, dementia or schizophrenia. Furthermore, fMRI now begins to be used for the purpose of marketing of products as industrial use. Measurement of comfortableness with fMRI provides companies useful information how people choose products. Therefore, expectation of fMRI measurements which produce more detail spatial and temporal information has been increasing.

We have investigated two kinds of emerging fMRI approaches in this dissertation: DW-fMRI and NMFD-fMRI. Those fMRI approaches are independent with hemodynamic responses originated from neural activities, and therefore expected to have superior spatial and temporal resolutions to conventional BOLD-fMRI. Hence, they potentially enable us to reveal neural activities such as those related to higher brain function (i.e. recognition or memory) more clearly. In addition, fMRI measurements with superior spatial and temporal resolutions are expected to be used effectively in diagnosis and treatment of psychiatric diseases.

By using DW-fMRI, we obtain magnitudes of water diffusion around neural cells, and therefore, it is considered that we can detect where the neural activities occur through the changes in the magnitudes of water diffusion. However, the interaction between neural activities and changes in magnitudes of water diffusion. Thus, we assumed that neural activities induce neural cell swelling and investigated the influences of changes in the size of the regions where water molecules diffuse in Chapter 3. We also demonstrated the influences of parameters of DWI and determined appropriate values for DW-fMRI measurement. Furthermore, we suggested that changes in volume ratio of intracellular and extracellular regions of neurons affect MR signal intensities in DW-fMRI in Chapter

4. Our suggestion will help understanding of the mechanism of DW-fMRI and further development of practical use.

NMFD-fMRI is considered to be the most direct method for fMRI though there still remain several problems. Among fMRI approaches with direct detection of neural magnetic fields, we employed the one using spin-lock imaging sequence. We investigated the mechanism of changes in MR signal intensities by calculating the interaction between the spin-lock pulse in the spin-lock imaging sequence and the targeted magnetic fields in Chapter 5. The simulation and MRI measurement with a phantom displayed the feasibility of detecting oscillating magnetic fields of the order of actual neural magnetic fields. Moreover, since this approach is observing the same phenomenon as MEG, the further development including combination with MEG can be expected.

Taken together, we believe that new fMRI approaches we discussed in this dissertation realize higher spatial and temporal resolutions than the conventional BOLD-fMRI and expect our study supports achievement of these fMRI approaches.

References

[1] S. C. Johnson, A. J. Saykin, L. C. Baxter, L. A. Flashman, R. B. Santulli, T. W McAllister, and A. C. Mamourian. The Relationship between fMRI Activation and Cerebral Atrophy: Comparison of Normal Aging and Alzheimer Disease. *NeuroImage*, 11(3):179–187, 2000.

[2] L. Wang, Y. Zang, Y. He, M. Liang, X. Zhang, L. Tian, T. Wu, T. Jiang, and K. Li. Changes in Hippocampal Connectivity in the Early Stages of Alzheimer's Disease: Evidence from Resting State fMRI. *NeuroImage*, 31(2):496–504, 2006.

[3] M. Pievani, W. de Haan, T. Wu, W. W. Seeley, and G. B. Frisoni. Functional Network Disruption in the Degenerative Dementias. *The Lancet Neurology*, 10(9):829–843, 2011.

[4] H. Takahashi, M. Koeda, K. Oda, T. Matsuda, E. Matsushima, M. Matsuura, K. Asai, and Y. Okubo. An fMRI Study of Differential Neural Response to Affective Pictures in Schizophrenia. *NeuroImage*, 22(3):1247–1254, 2004.

[5] S. Ruiz, N. Birbaumer, and R. Sitaram. Abnormal Neural Connectivity in Schizophrenia and fMRI-brain-computer Interface as a Potential Therapeutic Approach. *Frontiers in Psychiatry*, 4, 2013.

[6] S. Ogawa and T. M. Lee. Magnetic Resonance Imaging of Blood Vessels at High Fields: in Vivo and in Vitro Measurements and Image Simulation. *Magnetic Resonance in Medicine*, 16(1):9–18, 1990.

[7] S. Ogawa, T. M. Lee, A. S. Nayak, and P. Glynn. Oxygenation-sensitive Contrast in Magnetic Resonance Image of Rodent Brain at High Magnetic Fields. *Magnetic Resonance in Medicine*, 14(1):68–78, 1990.

[8] S. Ogawa, D. W. Tank, R. Menon, J. M. Ellermann, S. G. Kim, H. Merkle, and K. Ugurbil. Intrinsic Signal Changes Accompanying Sensory Stimulation: Functional Brain Mapping with Magnetic Resonance Imaging. *Proceedings of the National Academy of Sciences*, 89(13):5951–5955, 1992.

[9] R. B. Buxton. *An Introduction to Functional Magnetic Resonance Imaging: Principles and Techniques*. Cambridge University Press, 2002.

[10] R. A. Poldrack, J. A. Mumford, and T. E. Nichols. *Handbook of Functional MRI Data Analysis*. Cambridge University Press, 2011.

[11] A. Darquié, J. B. Poline, C. Poupon, H. Saint-Jalmes, and D. Le Bihan. Transient Decrease in Water Diffusion Observed in Human Occipital Cortex during Visual Stimulation. *Proceedings of the National Academy of Sciences*, 98(16):9391–9395, 2001.

[12] T. Araki. *Kakusan MRI - buraun undou, kakusan tensoru kara q kuukan he - (in Japanese)*. Shujunsha, Tokyo, 9 2006.

[13] Denis Le Bihan. Looking into the functional architecture of the brain with diffusion mri. *Nature Reviews Neuroscience*, 4(6):469–480, 2003.

[14] S. Kohno, N. Sawamoto, S. Urayama, T. Aso, K. Aso, A. Seiyama, H. Fukuyama, and D. Le Bihan. Water-diffusion slowdown in the human visual cortex on visual stimulation precedes vascular responses. *Journal of Cerebral Blood Flow & Metabolism*, 29(6):1197–1207, 2009.

[15] D. Le Bihan, S. Urayama, T. Aso, T. Hanakawa, and H. Fukuyama. Direct and fast detection of neuronal activation in the human brain with diffusion mri. *Proceedings of the National Academy of Sciences*, 103(21):8263–8268, 2006.

[16] J. Kershaw, M. Tomiyasu, K. Kashikura, Y. Hirano, H. Nonaka, M. Hirano, H. Ikehira, I. Kanno, and T. Obata. A multi-compartmental se-bold interpretation for stimulus-related signal changes in diffusion-weighted functional mri. *NMR in Biomedicine*, 22(7):770–778, 2009.

[17] T. Aso, S. Urayama, C. Poupon, N. Sawamoto, H. Fukuyama, and D.L. Bihan. An Intrinsic Diffusion Response Function for Analyzing Diffusion Functional MRI Time Series. *NeuroImage*, 47(4):1487–1495, 2009.

[18] R. D. Andrew and B. A. MacVicar. Imaging Cell Volume Changes and Neuronal Excitation in the Hippocampal Slice. *Neuroscience*, 62(2):371–383, 1994.

[19] T. Jin and S. G. Kim. Functional Changes of Apparent Diffusion Coefficient during Visual Stimulation Investigated by Diffusion-weighted Gradient-echo fMRI. *NeuroImage*, 41(3):801–812, 2008.

[20] S. L. Gangstead and A. W. Song. On the Timing Characteristics of the Apparent Diffusion Coefficient Contrast in fMRI. *Magnetic Resonance in Medicine*, 48(2):385–388, 2002.

[21] A.W. Song and S.L. Gangstead. The Spatial and Temporal Characteristics of the Apparent-diffusion-coefficient-dependent fMRI Signal Changes during Vsual Stimulation. *Journal of Neural Engineering*, 1:32, 2004.

[22] T. K. Truong and A. W. Song. Cortical Depth Dependence and Implications on the Neuronal Specificity of the Functional Apparent Diffusion Coefficient Contrast. *NeuroImage*, 47(1):65–68, 2009.

[23] J. Bodurka, A. Jesmanowicz, J. S. Hyde, H. Xu, L. Estkowski, and S. J. Li. Current-induced Magnetic Resonance Phase Imaging. *Journal of Magnetic Resonance*, 137(1):265–271, 1999.

[24] J. Bodurka and P. A. Bandettini. Toward Direct Mapping of Neuronal Activity: MRI Detection of Ultraweak, Transient Magnetic Field Changes. *Magnetic Resonance in Medicine*, 47(6):1052–1058, 2002.

[25] D. Konn, P. Gowland, and R. Bowtell. MRI Detection of Weak Magnetic Fields due to an Extended Current Dipole in a Conducting Sphere: a Model for Direct Detection of Neuronal Currents in the Brain. *Magnetic Resonance in Medicine*, 50(1):40–49, 2003.

[26] D. Konn, S. Leach, P. Gowland, and R. Bowtell. Initial Attempts at Directly Detecting Alpha Wave Activity in the Brain Using MRI. *Magnetic Resonance Imaging*, 22(10):1413–1427, 2004.

[27] N. Petridou, D. Plenz, A. C. Silva, M. Loew, J. Bodurka, and P. A. Bandettini. Direct Magnetic Resonance Detection of Neuronal Electrical Activity. *Proceedings of the National Academy of Sciences*, 103(43):16015–16020, 2006.

[28] W. I. Jay, R. S. Wijesinghe, B. D. Dolasinski, and B. J. Roth. Is it Possible to Detect Dendrite Currents Using Presently Available Magnetic Resonance Imaging Techniques? *Medical & Biological Engineering & Computing*, 50(7):651–657, 2012.

[29] T. S. Park and S. Y. Lee. Effects of Neuronal Magnetic Fields on MRI: Numerical Analysis with Axon and Dendrite Models. *NeuroImage*, 35(2):531–538, apr 2007.

[30] P. A. Bandettini, N. Petridou, and J. Bodurka. Direct Detection of Neuronal Activity with MRI: Fantasy, Possibility, or Reality? *Applied Magnetic Resonance*, 29(1):65–88, 2005.

[31] T. Witzel, F. H. Lin, B. R. Rosen, and L. L. Wald. Stimulus-induced Rotary Saturation (SIRS): A Potential Method for the Detection of Neuronal Currents with MRI. *NeuroImage*, 42(4):1357–1365, 2008.

[32] N. W. Halpern-Manners, V. S. Bajaj, T. Z. Teisseyre, and A. Pines. Magnetic Resonance Imaging of Oscillating Electrical Currents. *Proceedings of the National Academy of Sciences*, 107(19):8519–8524, 2010.

[33] H. H. Ray, G. B. William, and J. L. Christopher. *MRI: The Basics*. Lippincott Williams & Wilkins, 3 edition, 4 2010.

[34] G. D. Fullerton. Magnetic Resonance Imaging Signal Concepts. In *Annual Meeting of the Radiological Society of North America*, volume 29, 1986.

[35] E. L. Hahn. Spin Echoes. *Physical Review*, 80(4):580, 1950.

[36] R. L. Dixon and K. E. Ekstrand. The Physics of Proton NMR. *Medical physics*, 9:807, 1982.

[37] H. Y. Carr and E. M. Purcell. Effects of Diffusion on Free Precession in Nuclear Magnetic Resonance Experiments. *Physical Review*, 94(3):630, 1954.

[38] J. Hennig, A. Nauerth, and H. Friedburg. RARE imaging: a Fast Imaging Method for Clinical MR. *Magnetic Resonance in Medicine*, 3(6):823–833, 1986.

[39] R. B. Buxton, K. Uludağ, D. J. Dubowitz, and T. T. Liu. Modeling the Hemodynamic Response to Brain Activation. *NeuroImage*, 23:S220–S233, 2004.

[40] P. T. Fox and M. E. Raichle. Focal Physiological Uncoupling of Cerebral Blood Flow and Oxidative Metabolism during Somatosensory Stimulation in Human Subjects. *Proceedings of the National Academy of Sciences*, 83(4):1140–1144, 1986.

[41] P. T. Fox, M. E. Raichle, M. A. Mintun, and C. Dence. Nonoxidative Glucose Consumption during Focal Physiologic Neural Activity. *Science*, 241(4864):462–464, 1988.

[42] K. J. Friston, S. Williams, R. Howard, R. S. J. Frackowiak, and R. Turner. Movement-related Effects in fMRI Time-series. *Magnetic Resonance in Medicine*, 35(3):346–355, 1996.

[43] N. K. Logothetis, J. Pauls, M. Augath, T. Trinath, and A. Oeltermann. Neurophysiological Investigation of the Basis of the fMRI Signal. *Nature*, 412(6843):150–157, 2001.

[44] A. Einstein. On the Movement of Small Particles Suspended in Stationary Liquids Required by the Molecular-kinetic Theory of Heat. *Annalen der Physik*, 17(549-560):16, 1905.

[45] E. O. Stejskal and J. E. Tanner. Spin Diffusion Measurements: Spin Echoes in the Presence of a Time-dependent Field Gradient. *The Journal of Chemical Physics*, 42(1):288, 1965.

[46] M. G. Hall and D. C. Alexander. Convergence and Parameter Choice for Monte-Carlo Simulations of Diffusion MRI. *IEEE Transactions on Medical Imaging*, 28(9):1354–1364, 2009.

[47] M. Singh. Sensitivity of MR Phase Shift to Detect Evoked Neuromagnetic Fields inside the Head. *IEEE Transactions on Nuclear Science*, 41(1):349–351, 1994.

[48] H. Kamei, K. Iramina, K. Yoshikawa, and S. Ueno. Neuronal Current Distribution Imaging Using Magnetic Resonance. *IEEE Transactions on Magnetics*, 35(5):4109–4111, 1999.

[49] M. Sekino, T. Matsumoto, K. Yamaguchi, N. Iriguchi, and S. Ueno. A Method for NMR Imaging of a Magnetic Field Generated by Electric Current. *IEEE Transactions on Magnetics*, 40(4):2188–2190, 2004.

[50] J. Xiong, P. T. Fox, and J. H. Gao. Directly Mapping Magnetic Field Effects of Neuronal Activity by Magnetic Resonance Imaging. *Human Brain Mapping*, 20(1):41–49, 2003.

[51] R. H. Kraus Jr, P. Volegov, A. Matlachov, and M. Espy. Toward direct neural current imaging by resonant mechanisms at ultra-low field. *NeuroImage*, 39(1):310–317, 2008.

[52] A. M. Cassará, B. Maraviglia, and S. Hartwig. Neuronal Current Detection with Low-field Magnetic Resonance: Simulations and Methods. *Magnetic Resonance Imaging*, 27(8):1131–1139, 2009.

[53] N. Höfner, H. H. Albrecht, A. M. Cassará, G. Curio, S. Hartwig, J. Haueisen, I. Hilschenz, R. Korber, S. Martens, H. Scheer, J. Voigt, T. Lutz, and B. Martin. Are Brain Currents Detectable by Means of Low-field NMR? A Phantom Study. *Magnetic Resonance Imaging*, 29(10):1365–1373, 2011.

[54] A. G. Redfield. Nuclear Magnetic Resonance Saturation and Rotary Saturation in Solids. *Physical Review*, 98(6):1787, 1955.

[55] R. T. Canolty, E. Edwards, S. S. Dalal, M. Soltani, S. S. Nagarajan, H. E. Kirsch, M. S. Berger, N. M. Barbaro, and R. T. Knight. High Gamma Power is Phase-locked to Theta Oscillations in Human Neocortex. *Science*, 313(5793):1626–1628, 2006.

[56] S. R. Charagundla. T1ρ-weighted Magnetic Resonance Imaging: Principles and Diagnostic Application. *Applied Radiology*, 33(1):32–43, 2004.

[57] A. Borthakur, A. Wheaton, S. R. Charagundla, E. M. Shapiro, R. R. Regatte, S. V. S. Akella, J. B. Kneeland, and R. Reddy. Three-dimensional T1ρ-weighted MRI at 1.5 Tesla. *Journal of Magnetic Resonance Imaging*, 17(6):730–736, 2003.

[58] A. J. Wheaton, A. Borthakur, S. R. Charagundla, and R. Reddy. Pulse Sequence for Multislice T1ρ-weighted MRI. *Magnetic Resonance in Medicine*, 51(2):362–369, 2004.

[59] J. Nolte. *The human brain: An introduction to its functional anatomy*. Mosby, 2002.

[60] Y. Assaf, A. Mayk, and Y. Cohen. Displacement Imaging of Spinal Cord Using Q-space Diffusion-Weighted MRI. *Magnetic Resonance in Medicine*, 44(5):713–722, 2000.

[61] J. Laett, M. Nilsson, C. Malmborg, H. Rosquist, R. Wirestam, F. Ståhlberg, D. Topgaard, and S. Brockstedt. Accuracy of Q-space Related Parameters in MRI: Simulations and Phantom Measurements. *IEEE transactions on Medical Imaging*, 26(11):1437–1447, 2007.

[62] S. Nagahara, T. Oida, and T. Kobayashi. Dependence of diffusion weighted mr signal intensities on imaging parameters and restricted size. *Transaction of the Japanese Society for Medical and Biological Engineering*, 48(3):281–290, 2010. (in Japanese).

[63] P. Vestergaard-Poulsen, B. Hansen, L. Østergaard, and R. Jakobsen. Microstructural Changes in Ischemic Cortical Gray Matter Predicted by a Model of Diffusion-weighted MRI. *Journal of Magnetic Resonance Imaging*, 26(3):529–540, 2007.

[64] K. D. Harkins, J. P. Galons, T. W. Secomb, and T. P. Trouard. Assessment of the Effects of Cellular Tissue Properties on ADC Measurements by Numerical Simulation of Water Diffusion. *Magnetic Resonance in Medicine*, 62(6):1414–1422, 2009.

[65] J. Frahm, K. D. Merboldt, W. Hanicke, and A. Haase. Stimulated Echo Imaging. *Journal of Magnetic Resonance*, 64(1):81–93, 1985.

[66] S. Heiland, O. Dietrich, and K. Sartor. Diffusion-weighted Imaging of the Brain: Comparison of Stimulated-and Spin-echo Echo-planar Sequences. *Neuroradiology*, 43(6):442–447, 2001.

[67] W. S. Hinshaw and A. H. Lent. An Introduction to NMR Imaging: From the Bloch Equation to the Imaging Equation. *Proceedings of the IEEE*, 71(3):338–350, 1983.

[68] P. K. Madhu and A. Kumar. Direct Cartesian-space Solutions of Generalized Bloch Equations in the Rotating Frame. *Journal of Magnetic Resonance, Series A*, 114(2):201–211, 1995.

[69] R. V. Mulkern and M. L. Williams. The General Solution to the Bloch Equation with Constant RF and Relaxation Terms: Application to Saturation and Slice Selection. *Medical Physics*, 20:5, 1993.

[70] K. Murase and N. Tanki. Numerical Solutions to the Time-dependent Bloch Equations Revisited. *Magnetic Resonance Imaging*, 29(1):126–131, 2011.

[71] A. Borthakur and A. J. Wheaton. In Vivo Measurement of T1ρ Dispersion in the Human Brain at 1.5 Tesla. *Journal of Magnetic Resonance Imaging*, 19(4):403–409, 2004.

[72] W. D. Rooney, G. Johnson, X. Li, E. R. Cohen, S. G. Kim, K. Ugurbil, and C. S. Springer. Magnetic Field and Tissue Dependencies of Human Brain Longitudinal 1H2O Relaxation in Vivo. *Magnetic Resonance in Medicine*, 57(2):308–318, 2007.

[73] A. Borthakur, J. Hulvershorn, E. Gualtieri, A. J. Wheaton, S. Charagundla, M. A Elliott, and R. Reddy. A Pulse Sequence for Rapid in Vivo Spin-ocked MRI. *Journal of Magnetic Resonance Imaging*, 23(4):591–596, 2006.

[74] T. Jin and S. G. Kim. Characterization of Non-hemodynamic Functional Signal Measured by Spin-lock fMRI. *NeuroImage*, 78:385–395, 2013.

Publication List

Full papers

1. Shizue Naagahara, Takenori Oida and Tetsuo Kobayashi, Dependence of Diffusion Weighted MR Signal Intensities on Imaging Parameters and Restricted Size (in Japanese). *Transaction of the Japanese Society for Medical and Biological Engineering*, 48(3):281–290, 2010

2. Takenori Oida, Shizue Naagahara and Tetsuo Kobayashi, Acquisition Parameter Settings in Diffusion Tensor Imaging for Emphasizing Fractional Anisotropy. *Magnetic Resonance in Medical Science*, 10(2):121–128, 2011

3. Shizue Nagahara, Takenori Oida and Tetsuo Kobayashi, An Explanation of Signal Changes in DW-fMRI: Monte Carlo Simulation Study of Restricted Diffusion of Water Molecules Using 3D and Two-compartment Cortical Cell Models. *IEICE TRANSACTIONS on Information and Systems*, E96-D(6):1387–1393, 2013

4. Shizue Nagahara, Masahito Ueno and Tetsuo Kobayashi, Spin-Lock Imaging for Direct Detection of Oscillating Magnetic Fields with MRI: Simulations and Phantom Studies *Advanced Biomedical Engineering*, accepted for publication in October, 2013

Proceedings (International conference)

1. Takenori Oida, Shizue Nagahara, and Tetsuo Kobayashi, Acquisition Parameters in MR Diffusion Tensor Imaging for Clarifying the Direction of Nerve Fibers. *Proceedings of 18th International Congress on Brain Electromagnetic Topography*, 209–212, 2009

2. Shizue Nagahara, Takenori Oida and Tetsuo Kobayashi, Appropriate MPG Parameters for Diffusion Weighted Functional MRI. *Proceedings of 18th International Congress on Brain Electromagnetic Topography*, 213–216, 2009

3. Shizue Nagahara, Takenori Oida and Tetsuo Kobayashi, Simulation Studies on Appropriate Imaging Parameters for DW-fMRI Using 3D and 2-compartment Models. *Proceedings of the 2012 International Conference on Complex Medical Engineering*, CFP12CME-CDR:619–622, 2012

4. Shizue Nagahara and Tetsuo Kobayashi, Bloch Simulations towards Direct Detection of Oscillating Magnetic Fields Using MRI with Spin-Lock Sequence. *Proceedings of the 35th Annual International Conference of the IEEE Engineering in Medicine and Biology Society (EMBS)*, 1061–1064, 2013

Proceedings (Domestic conference)

1. Shizue Nagahara, Takenori Oida and Tetsuo Kobayashi, Simulation Studies on Appropriate Imaging Parameters for Diffusion Weighted Function MRI (in Japanese). *The Technical Report of The Proceeding of The Institute of Electronics, Information and Communication Engineers*, 109(63):175–180, 2009

2. Shizue Nagahara, Takenori Oida and Tetsuo Kobayashi, A Functional MRI Study Using Spin-lock Sequence Toward the Detection of Neural Magnetic Fields (in Japanese). *The Technical Report of The Proceeding of The Institute of Electronics, Information and Communication Engineers*, 112(479):25–30, 2013

3. Masahito Ueno, Shizue Nagahara, Yosuke Ito and Tetsuo Kobayashi, Studies on Measurements of Neural Magnetic Fields by Using MRI with Spin-lock Sequence (in Japanese). *The Journal of Japan Biomagnetism and Bioelectromagnetics Society*, 26(1):224–225, 2013